

Technische Universität München
TUM School of Engineering and Design

Modeling and Characterization of Acoustically Absorbing Liners

Alireza Javareshkian

Vollständiger Abdruck der von TUM School of Engineering and Design zur
Erlangung des akademischen Grades eines

DOKTORS DER INGENIEURWISSENSCHAFTEN

genehmigten Dissertation.

Vorsitzender:

Prof. Dr.-Ing. Steffen Marburg

Prüfer der Dissertation:

1. Prof. Dr.-Ing. Thomas Sattelmayer
2. Prof. Bruno Facchini

Die Dissertation wurde am 17.11.2021 bei der Technischen Universität München eingereicht
und durch TUM School of Engineering and Design am 14.02.2022 angenommen.

Abstract

Modern gas turbines are prone to thermo-acoustic instabilities due to the operation under the lean regime, which is essential for emission reduction. Bias flow liners can address this issue and suppress combustion instabilities by enhancing the system's acoustic loss. To optimally design the bias flow liners, several acoustic impedance models are proposed by authors that consider a multitude of parameters. The majority of these models neglect the interaction effect between the orifices, while in practice, orifices are closely distributed, and the interactions between acoustic radiation from neighboring orifices may influence their acoustic characteristics. The hole-to-hole interaction effect may vary the resonator's resonance frequency due to the non-planar wave creation in the orifices of the perforated plate, in the cavity, and in near-wall regions in the combustor. By considering this effect, predicting the resonance frequency of the resonator may become more accurate. This thesis presents a three-dimensional analytical method, which is developed to consider the non-planar wave creation in the cavity and the orifices in the perforated plate. Present study employs the proposed three-dimensional analytical method to determine the hole-to-hole interaction end-correction of multi-orifice perforated plates.

Furthermore, the hole-to-hole interaction end-correction of a series of perforated plates with different orifice radii and spacing is obtained via the Finite Element Method (FEM). Several perforated plate samples with different center-to-center hole spacing are studied using an impedance tube test rig. Experimental results confirm that the resonance frequency is shifted towards higher frequency with increasing holes' spacing. The acquired model is validated with the experimental results and the end-correction models available in the literature. The comparison confirms that the end-correction models available in the literature cannot predict the hole-to-hole interaction effect, which is observed in measurements. On the contrary, the proposed model can reproduce the experimental measurements with high accuracy. The acquired model shows that the acoustic end-correction length of orifices is related to the porosity ratio and orifice radius of perforated plates.

Kurzfassung

Moderne Gasturbinen mit mager-vorgemischter Verbrennung, die zur Emissionsreduzierung erforderlich ist, sind anfällig für thermoakustische Verbrennungsinstabilitäten. Durch Brennkammerwände mit Kühlluftlöchern ("Bias-Flow-Liner") kann dieses Problem adressiert und Verbrennungsinstabilitäten unterdrückt werden, indem sie die akustischen Verluste des Verbrennungssystems erhöhen. Um diese "Bias-Flow-Liner" hierfür optimal auszulegen, haben bereits mehrere Autoren verschiedene akustische Impedanzmodelle vorgeschlagen, die eine Vielzahl von Parametern berücksichtigen. Die meisten dieser Modelle vernachlässigen den Interaktionseffekt zwischen den Kühlluftlöchern. In der praktischen Anwendung sind die Kühlluftlöcher allerdings meist eng beieinanderliegend, sodass akustische Wechselwirkungen zwischen benachbarten Öffnungen deren akustische Eigenschaften beeinflussen können. Dieser Loch-zu-Loch-Wechselwirkungseffekt kann die Resonanzfrequenz des "Bias-Flow-Liners" aufgrund der nicht-planaren akustischen Wellenausbreitung in den Lochöffnungen, der dahinterliegenden Kavität sowie den wandnahen Bereichen in der Brennkammer verändern. In der vorliegenden Arbeit wird eine dreidimensionale (3D) analytische Methode vorgestellt, die entwickelt wurde, um die beschriebene nicht-planare Wellenausbreitung zu berücksichtigen und somit die Genauigkeit der Vorhersage der Resonanzfrequenz des "Bias-Flow-Liners" zu verbessern. Die vorgeschlagene analytische 3D-Methode wird hierbei angewendet, um die akustischen Loch-zu-Loch-Wechselwirkungseffekte von Lochplatten mit mehreren Lochöffnungen in Form einer "Lochlängen-Endkorrektur" zu bestimmen.

Darüber hinaus wird diese Endkorrektur, zur Berücksichtigung der akustischen Loch-zu-Loch-Wechselwirkung, für verschiedene Lochplatten mit unterschiedlichen Lochöffnungsradien und -abständen mit Hilfe einer Finite-Elemente-Methode (FEM) ermittelt. Ergänzend werden mehrere Lochplattenkonfigurationen mit unterschiedlichen Lochabständen mittels eines Impedanzrohr-Prüfstands untersucht. Die experimentellen Ergebnisse bestätigen, dass sich die Resonanzfrequenz der untersuchten Lochplat-

ten mit zunehmendem Lochabstand zu höheren Frequenzen verschiebt. Das entwickelte Modell wird mit den experimentellen Ergebnissen und den in der Literatur verfügbaren Endkorrekturmodellen validiert. Der Vergleich bestätigt, dass die in der Literatur verfügbaren Endkorrekturmodelle den Loch-zu-Loch-Wechselwirkungseffekt, der in experimentellen Messungen beobachtet wird, nicht korrekt vorhersagen können. Das vorgeschlagene Modell kann dagegen die experimentellen Messungen mit hoher Genauigkeit reproduzieren. Des Weiteren kann auf Basis dieses Modells gezeigt werden, dass die akustische Endkorrektur von Lochplatten abhängig von deren Porosität und Lochradius ist.

Contents

1	Introduction	1
1.1	Objectives	3
1.2	Outline of the Thesis	4
2	Acoustic Modeling of Perforations	5
2.1	Impedance Modeling of Perforations	6
2.2	Mass End-Correction	9
2.3	Hole-to-hole Interaction	17
2.4	Howe’s Rayleigh Conductivity Model	19
2.5	Jing’s Impedance Model	21
2.6	Bellucci’s Impedance Model	21
3	Modeling Approach	27
3.1	Theoretical Background	27
3.1.1	Acoustic Wave Equation	27
3.1.2	Three-Dimensional Waves	30
3.1.3	Plane Waves	33
3.2	Modeling for Two and Multiple Holes	35
4	Numerical Analysis (FEM)	43
4.1	Numerical Setup	44
4.2	Two and Multiple Holes	46
4.3	Machine Learning	53
5	Experimental Setup and Measurement Techniques	69
5.1	Plane Wave Decomposition	69
5.2	Experimental Setup	71

6 Results and Discussion	75
6.1 Experimental validation without Bias Flow	75
6.2 Experimental validation with Bias Flow	84
7 Summary	95
A Modeling Details	99
B Re-calibration of the Coefficients of the Expression l_{nl}	103
C Re-calibration of the Coefficients of the Expression l_B	107
D Final Configuration of the Acoustic Impedance Model	115

List of Figures

2.1	Schematic view of an orifice presenting the quantities to determine Rayleigh conductivity of an orifice.	9
2.2	Cross-section view of the configurations studied by Ingard [1]. .	13
2.3	Configuration functions ψ and their fitted functions used in end-corrections as a function of ξ	15
2.4	Real term γ and imaginary term δ of the normalized Rayleigh conductivity plotted as a function of the Strouhal number. . . .	21
3.1	Schematic view of the domain consisting of a plate and a cavity.	35
3.2	Schematic view of the studied orifice patterns (P, S, and Sa denote triangular, square, and rectangular patterns, respectively). .	42
4.1	Schematic view of the domain investigated numerically.	44
4.2	Schematic view of the plates with two-holes (A1) and multi-orifice (E1).	47
4.3	Comparison of the normalized end-correction obtained for two-holes (A1) and multi-orifice (E1) configurations by increasing the number of higher-order modes ($N = m = n = 5$) included in the three-dimensional analytical method [2].	48
4.4	Normalized specific acoustic reactance of perforated plates with the orifice radius $r_0 = 1.25 \text{ mm}$ and various center-to-center spacing obtained from FEM [2].	49
4.5	Normalized specific acoustic reactance of perforated plates with the orifice radius $r_0 = 1.75 \text{ mm}$ and various center-to-center spacing obtained from FEM [2].	50
4.6	Acoustic velocity magnitude contour in the vicinity of orifices with radius $r_0 = 0.8 \text{ mm}$ and orifice spacing $a = 12.75 \text{ mm}$ [2]. .	51

4.7	Acoustic velocity magnitude contour in the vicinity of orifices with radius $r_0 = 0.8 \text{ mm}$ and orifice spacing $a = 2.25 \text{ mm}$ [2]. . .	51
4.8	The contour of interpolated normalized end-correction (δ) of perforated plates with triangular pattern (P) obtained from FEM [2].	53
4.9	The contour of interpolated normalized end-correction (δ) of perforated plates with square pattern (S) obtained from FEM [2].	54
4.10	Perforated plates that are considered as the boundary of the geometrical parameters. The samples on the top represent the situation where orifices are too close to each other such that they intersect, and the bottom samples represent the situation where orifices are inasmuch far from each other such that they are located on the periphery of the plate.	58
4.11	The training data set for the P configuration.	59
4.12	The area associated with the perforation region is shaded.	60
4.13	Representation of the equivalent circle and its radius.	60
4.14	The training data set for the P configuration with the transformed axes.	61
4.15	The training data sets for the S and Sa configurations with the transformed axes.	62
4.16	Predicted response versus true response for P configuration. . .	63
4.17	Predicted response versus true response for S and Sa configurations.	64
4.18	Data points' residual of trained models for P configuration. . . .	64
5.1	Illustration of the two waves propagating in the opposite direction.	70
5.2	Schematic view of the impedance tube used for characterization of perforated plates.	71
5.3	Perforated plate samples that are studied experimentally.	72
6.1	Magnitude (top) and phase (bottom) of reflection coefficient for the P pattern with the cavity length of $L_c = 30 \text{ mm}$ [2].	76
6.2	Magnitude (top) and phase (bottom) of reflection coefficient for the S and Sa patterns with the cavity length of $L_c = 30 \text{ mm}$ [2]. .	77

6.3	Magnitude (top) and phase (bottom) of reflection coefficient for the S1 case with the cavity length of $L_c = 30 \text{ mm}$ and various excitation amplitudes.	80
6.4	Magnitude (top) and phase (bottom) of reflection coefficient for the P1 case with the cavity length of $L_c = 30 \text{ mm}$ [2].	81
6.5	Magnitude (top) and phase (bottom) of reflection coefficient for the S1 case with the cavity length of $L_c = 30 \text{ mm}$ [2].	82
6.6	Magnitude (top) and phase (bottom) of reflection coefficient for the P1 case with the cavity length of $L_c = 30 \text{ mm}$ and various bias flow velocities (U_B).	85
6.7	Magnitude (top) and phase (bottom) of reflection coefficient for the P1 case with the cavity length of $L_c = 30 \text{ mm}$ and various bias flow velocities (U_B).	86
6.8	Magnitude (top) and phase (bottom) of reflection coefficient for the S1 case with the cavity length of $L_c = 30 \text{ mm}$ and various bias flow velocities (U_B).	87
6.9	Comparison of the model predictions for the magnitude (top) and phase (bottom) of reflection coefficient for the S1 case with the cavity length of $L_c = 30 \text{ mm}$ at the bias flow velocity $U_B = 1.1 \text{ m/s}$	89
6.10	Comparison of the model predictions for the magnitude (top) and phase (bottom) of reflection coefficient for the S1 case with the cavity length of $L_c = 30 \text{ mm}$ at the bias flow velocity $U_B = 4.5 \text{ m/s}$	91
6.11	Comparison of the model predictions for the magnitude (top) and phase (bottom) of reflection coefficient for the P1 case with the cavity length of $L_c = 30 \text{ mm}$ at the bias flow velocity $U_B = 4.5 \text{ m/s}$	92
B.1	Magnitude (top) and phase (bottom) of reflection coefficient for the S1 case with the cavity length of $L_c = 30 \text{ mm}$ and various excitation amplitudes obtained from direct measurement of acoustic pressure in the impedance tube.	104

B.2 Magnitude (top) and phase (bottom) of reflection coefficient for the P1 case with the cavity length of $L_c = 30 \text{ mm}$ and various excitation amplitudes obtained from direct measurement of acoustic pressure in the impedance tube. 105

C.1 Magnitude (top) and phase (bottom) of reflection coefficient for the P2 case with the cavity length of $L_c = 30 \text{ mm}$ obtained from direct measurement of acoustic pressure in the impedance tube. 108

C.2 Magnitude (top) and phase (bottom) of reflection coefficient for the P3 case with the cavity length of $L_c = 30 \text{ mm}$ obtained from direct measurement of acoustic pressure in the impedance tube. 109

C.3 Magnitude (top) and phase (bottom) of reflection coefficient for the S2 case with the cavity length of $L_c = 30 \text{ mm}$ obtained from direct measurement of acoustic pressure in the impedance tube. 110

C.4 Magnitude (top) and phase (bottom) of reflection coefficient for the S3 case with the cavity length of $L_c = 30 \text{ mm}$ obtained from direct measurement of acoustic pressure in the impedance tube. 111

C.5 Magnitude (top) and phase (bottom) of reflection coefficient for the S1a case with the cavity length of $L_c = 30 \text{ mm}$ obtained from direct measurement of acoustic pressure in the impedance tube. 112

C.6 Magnitude (top) and phase (bottom) of reflection coefficient for the S2a case with the cavity length of $L_c = 30 \text{ mm}$ obtained from direct measurement of acoustic pressure in the impedance tube. 113

List of Tables

- 2.1 Expressions of the mass end-correction at low frequency for different perforation configurations derived by Ingard [1]. mn^* stands for a summation where mode ($m = n = 0$) is excluded and n^* represents a summation where the mode ($n = 0$) is neglected. 14
- 3.1 Geometrical parameters of the cases investigated numerically. . 42
- 4.1 NRMSE [%] values of the machine learning models trained for P configuration on the training data set. 65
- 4.2 NRMSE [%] values of the machine learning models trained for S and Sa configurations on the training data set. 65
- 4.3 NRMSE [%] values of the machine learning models trained for P configuration applied to the test data set. 67
- 4.4 NRMSE [%] values of the machine learning models trained for S and Sa configurations applied to the test data set. 68
- 5.1 Geometrical parameters of the perforated plates that are studied experimentally. 73
- 6.1 Predicted resonance frequency of the perforated plates investigated experimentally. 84

Nomenclature

Latin Letters

A	$[m^2]$	Cross-section area
A_h	$[m^2]$	Hole cross-section area
A_{open}	$[m^2]$	Open area
Ai_{mn}	$[Pa]$	Pressure amplitude of the mode (m:n) in the direction of z in the i -th orifice
Ai_{00}	$[Pa]$	Pressure amplitude of the mode (0:0) in the direction of z in the i -th orifice
A_p	$[m^2]$	Plate cross-section area
a	$[m]$	Orifices center-to-center distance
a	$[m]$	Width of the rectangular duct
Bi_{mn}	$[Pa]$	Pressure amplitude of the mode (m:n) in the opposite direction of z in the i -th orifice
Bi_{00}	$[Pa]$	Pressure amplitude of the mode (0:0) in the opposite direction of z in the i -th orifice
b	$[m]$	Length of the rectangular duct
b_{mn}	$[-]$	Eigenvalue of J_m
C_{mn}	$[Pa]$	Pressure amplitude of the mode (m:n) in the direction of z in the cavity
C_{00}	$[Pa]$	Pressure amplitude of the mode (0:0) in the direction of z in the cavity
c	$[m/s]$	Speed of sound
C_d	$[-]$	Discharge coefficient
D_{mn}	$[Pa]$	Pressure amplitude of the mode (m:n) in the opposite direction of z in the cavity

Nomenklatur

D_{00}	[Pa]	Pressure amplitude of the mode (0:0) in the opposite direction of z in the cavity
d_i	[m]	Distance of the i -th orifice from tube center
$f_{c,mn}$	[Hz]	Cut-on frequency of mode (m:n)
f_{res}	[Hz]	Resonance frequency
He	[-]	Helmholtz number
I_m	[-]	Modified Bessel function of the first kind of order m
i	[-]	Imaginary unit
J_m	[-]	Bessel function of the first kind of order m
K_R	[m]	Rayleigh conductivity
K_m	[-]	Modified Bessel function of the second kind of order m
k	[-]	Gaussian Process covariance function
k	[1/m]	Wave number
$k_{r,mn}$	[1/m]	Radial wave number of mode (m:n)
$k_{r,mn}^I$	[1/m]	Radial wave number of mode (m:n) in the orifice
$k_{r,mn}^{II}$	[1/m]	Radial wave number of mode (m:n) in the cavity
k_s	[1/m]	Stokes wave number
$k_{z,mn}$	[1/m]	Axial wave number of mode (m:n)
$k_{z,mn}^I$	[1/m]	Axial wave number of mode (m:n) in the orifice
$k_{z,mn}^{II}$	[1/m]	Axial wave number of mode (m:n) in the cavity
L_c	[m]	Cavity length
L_p	[m]	Plate thickness
L'_p	[m]	Effective plate thickness
l	[m]	Orifice length
l'	[m]	End-correction length
l'_{11}	[m]	End-correction length of an eccentric orifice
l'_{12}	[m]	End-correction length of an eccentric orifice due to the second orifice
$l'_{Bellucci}$	[m]	End-correction length of Bellucci's original model
l_{eff}	[m]	Effective orifice length
M_B	[-]	Bias flow Mach number
m	[-]	Circumferential mode order
m	[-]	Gaussian Process mean function
N	[-]	Truncated number of higher-order modes m and n

n	$[-]$	Radial mode order
p	$[Pa]$	Pressure
p_0	$[Pa]$	Mean pressure
p'	$[Pa]$	Acoustic pressure
\hat{p}	$[Pa]$	Complex acoustic pressure amplitude
\hat{p}_{cavity}	$[Pa]$	Complex acoustic pressure amplitude in the cavity
\hat{p}_{hole}	$[Pa]$	Complex acoustic pressure amplitude in the orifice
\hat{p}_{mn}	$[Pa]$	Complex amplitude of mode (m:n)
\dot{q}'	$[W]$	Heat release perturbation
\hat{q}	$[m^3/s]$	Complex acoustic volume velocity
R	$[-]$	Acoustic reflection coefficient
R_c	$[m]$	Tube radius
R_{eq}	$[m]$	Equivalent circle radius
R_g	$[J/(kgK)]$	Specific gas constant
r	$[-]$	Radial coordinate
r_0	$[m]$	Orifice radius
s	$[J/(kgK)]$	Specific entropy
Sh	$[-]$	Shear number
St	$[-]$	Strouhal number
St_{ac}	$[-]$	Acoustic Strouhal number
$(St_{ac})_{qs}$	$[-]$	Quasi-steady acoustic Strouhal number
T	$[K]$	Temperature
t	$[s]$	Time
U_B	$[m/s]$	Bias flow velocity
\mathbf{u}	$[m/s]$	Velocity vector
u_0	$[m/s]$	Mean velocity
\hat{u}	$[m/s]$	Complex acoustic velocity amplitude
\hat{u}_{cavity}	$[m/s]$	Complex acoustic velocity amplitude in the cavity
\hat{u}_{hole}	$[m/s]$	Complex acoustic velocity amplitude in the orifice
u'	$[m/s]$	Acoustic velocity
V	$[m^3]$	Cavity volume
Z	$[kg/(m^4s)]$	Acoustic impedance
z	$[-]$	Axial coordinate
z	$[kg/(m^2s)]$	Specific acoustic impedance

z_0 [kg/(m²s)] Characteristic acoustic impedance

Greek Letters

α	[-]	Absorption coefficient
χ	[-]	Normalized specific acoustic reactance
$\chi_{Bellucci}$	[-]	Normalized specific acoustic reactance of Bellucci's original impedance model
δ	[-]	Imaginary part of the Rayleigh conductivity
δ	[-]	Average normalized end-correction of all orifices
δ_i	[-]	Normalized end-correction of i -th orifice
δ_P	[-]	Normalized end-correction of triangular (P) pattern
$\delta_{S,Sa}$	[-]	Normalized end-correction of square (S) and rectangular (Sa) patterns
ϵ	[-]	SVM prediction error
ε	[-]	Pressure loss coefficient
γ	[-]	Real part of the Rayleigh conductivity
λ	[m]	Wavelength
ν	[m ² /s]	Kinematic viscosity
ξ	[-]	Square root of perforation porosity
θ	[-]	Circumferential coordinate
θ	[-]	Normalized specific acoustic resistance
$\theta_{Bellucci}$	[-]	Normalized specific acoustic resistance of Bellucci's original impedance model
ρ	[kg/m ³]	Density
ρ_0	[kg/m ³]	Mean density
ρ'	[kg/m ³]	Fluctuating density
σ	[-]	Perforation porosity
σ_{eff}	[-]	Effective perforation porosity
ω	[1/s]	Angular frequency
ψ	[-]	Configuration function
ζ	[-]	Normalized specific acoustic impedance

Superscripts

$(\cdot)^+$	In positive z -direction
$(\cdot)^-$	In negative z -direction
$(\cdot)^I$	Domain inside orifice
$(\cdot)^{II}$	Domain inside cavity

Abbreviations

FEM	Finite Element Method
GP	Gaussian Process
OLS	Ordinary Least Squares
SVM	Support Vector Machine
SVR	Support Vector Regression
NRMSE	Normalized Root Mean Square Error

1 Introduction

Gas turbines are widely used to generate electricity in power plants or as aircraft engines. The energy sector relies on gas turbines for electricity generation. The gas turbine plays an essential role even with the increasing share of renewable energies in the global energy portfolio due to its rapid start-up compared to the other power generation technologies. This short start-up time ensures flexibility of power supply at the peak of consumption or in the case of a temporary shortage of solar or wind power due to the intermittency of their sources.

Strict emission regulations have been established to reduce the environmental impacts of gas turbine applications. It is aimed to reduce CO₂ emission up to 75% and NO_x emission up to 90% until 2050, respectively [3]. The CO₂ emission level has been decreased constantly as a result of the optimization of energy systems to consume less fuel [4]. NO_x emission reduction is a major concern in the operation of gas turbines. One of the major factors in the NO_x emission reduction is to decrease the flame temperature.

Lean premixed combustion technology has been widely employed in gas turbines in order to comply with the emission regulations. By adopting this technology, the combustion device operates with excess air (beyond the stoichiometric air-fuel-ratio of the mixture) to reduce the combustion temperature and consequently formation of NO_x. However, implementing this technology makes the combustor exposed to combustion instabilities. Combustion instabilities are pressure oscillations that result from a thermo-acoustic feedback loop between acoustic pressure oscillations and the heat release. Depending on the phase difference between the fluctuating heat release (\dot{q}') and acoustic pressure fluctuation (p'), a thermo-acoustic loop establishes which can either produce or consume work. When the acoustic pressure pulsations and the heat release perturbation are in phase, work in the form of acoustic en-

ergy is fed into the acoustic field. This necessary condition is referred to as Rayleigh criterion [5, 6] which is presented in Equation 1.1.

$$\int_T p'(t) \dot{q}'(t) dt > 0 \quad (1.1)$$

When the Rayleigh criterion is positive, self-excited oscillation may promote and the combustor operates in a thermoacoustically unstable region. This condition is necessary but not sufficient. Instability requires that the driving forces of the flame exceed the acoustic losses in the combustion chamber. If both conditions apply, instability occurs.

Combustion instabilities may lead to structural damages or even a flame blow-off. Therefore, it is desirable to avoid combustion instabilities. One method to avoid instabilities is to enhance the system's acoustic losses (known as passive damping). The predominant means of acoustic damping of gas turbines is passive damping [7]. The most important passive elements are Helmholtz resonators, quarter-wave tubes, and acoustic liners. Helmholtz resonators and quarter-wave tubes have already been integrated into combustor systems [8–13]. One major shortcoming of these damping elements is the limited frequency range of optimal damping. Thus, several dampers with different absorption characteristics would be required to cover the frequency range corresponding with different operating conditions of the system. Moreover, resonators' size grows considerably at low frequencies that poses difficulties to mount them on the engine, especially aircraft engines, due to their additional weight.

Perforated acoustic liners can be used as an alternative for the Helmholtz resonators and quarter-wave tubes [14]. In general, orifices or perforations can contribute to damping acoustic pulsations. The orifices on an acoustic liner are always supplying cooling airflow. This cooling airflow that is mainly designed to cool down the combustor wall has been reported to significantly affect the liner's damping characteristics. It is demonstrated that acoustic waves can be damped substantially when transmitted through the orifices in perforated liners with bias flow, which results in cooling air jets in the combustor [15] because of the conversion of acoustic energy into the shedding vortic-

ity in the presence of a bias flow. The major advantage of perforated bias flow liners over Helmholtz resonators and quarter-wave tubes is the capability of the bias flow liner in broadband damping of the acoustic pressure pulsations.

1.1 Objectives

The optimal design of the acoustic liner is a key factor for developing low emission combustion systems in modern gas turbines and aircraft engines. In order to design and evaluate the performance of perforated acoustic liners, several acoustic impedance models are available in the literature. The amount of literature that addresses acoustic characteristics of perforations is vast. Most of the acoustic impedance models neglect the interaction effect between the orifices. In other words, these models are developed for a single orifice on the plate and extended to a pattern of orifices by considering the number of orifices (area ratio). In application, perforations are often tightly distributed such that the interactions between acoustic radiations from neighboring orifices can affect their acoustical behavior. The hole-to-hole interaction effect may change the resonance frequency of the resonator due to the non-planar wave propagation in the cavity, the orifices in the perforated plate, and the near-wall region in the combustor. Considering this effect may help to predict the resonance frequency of the resonator accurately.

This thesis aims to model the hole-to-hole interaction in multi-orifice perforated plates to evaluate the effect of orifices' distance on the acoustic characteristics of the perforated plates backed by a cavity. To the author's knowledge, the hole-to-hole interaction effect on the acoustic impedance is not investigated and addressed in the literature. The effect of porosity is inappropriately used to consider the hole-to-hole interaction effect in various acoustic impedance models available in the literature, which are described in Chapter 2 in further detail. This study aims to develop a three-dimensional (3D) analytical approach to account for the non-planar wave creation in the cavity and the orifices in the perforated plate.

Furthermore, a low order model for predicting the hole-to-hole interaction

end-correction is proposed that can be readily integrated into the available acoustic impedance models. Additionally, to evaluate the significance of considering the hole-to-hole interaction effect on the resonator's acoustic characteristics in the presence of a bias flow, several perforated plates are studied experimentally. To the author's knowledge, this effect is not investigated experimentally, in the literature.

1.2 Outline of the Thesis

Chapter 2 presents a detailed overview of the acoustic impedance modeling followed by the various modeling approaches that are available in the literature to predict the acoustic performance of perforated liners. In Chapter 3, the essential theoretical background is collected, and a three-dimensional analytical approach is developed to account for the non-planar wave propagation in the cavity and orifices on the perforated plate. The present study employs the proposed three-dimensional analytical method to determine the hole-to-hole interaction end-correction of multi-orifice perforated plates. The hole-to-hole interaction end-correction from a series of perforated plates with different orifice radii and spacing is obtained via the Finite Element Method (FEM) and presented in Chapter 4. Chapter 5 presents the details about the analysis of the measurements. This includes a detailed description of the properties of the Impedance Tube Test Rig and the perforated plate specimens with different holes' center-to-center spacing, which are tested experimentally. The results are presented in Chapter 6, and the current findings as well as previous results from other studies are discussed, and the impedance models are compared to the experimental results.

2 Acoustic Modeling of Perforations

This chapter starts with a detailed overview of the acoustic impedance modeling. Section 2.1 presents the concepts of internal impedance and Rayleigh conductivity for a theoretical description of the acoustic properties of an orifice, and demonstrates that it is required to correct the length of the orifice by including an additional length correction term for an orifice with finite length. Section 2.2 introduces the concept of mass end-correction and presents several end-correction models that are available in the literature and used in acoustic impedance models. Section 2.3 introduces the hole-to-hole interaction effect in multi-orifice perforated plates and presents that this effect is different from the mass end-correction, while several authors inappropriately used the mass end-correction instead of hole-to-hole interaction effect. Section 2.3 presents the theoretical work of Ingard [1], which leads to an expression for the calculation of the hole-to-hole interaction end-correction for two holes in a plate, and shows that a comprehensive analysis of the hole-to-hole interaction effect in multi-orifice perforated plates is required to develop a correct analytical approach. The work of Ingard [1] is used as the state of the art to validate the methodologies that are proposed in Chapters 3 and 4. Section 2.4 briefly describes Howe's Rayleigh conductivity model, which is used in the impedance models proposed by Jing et al. [16] and Belucci et al. [8, 17] in Sections 2.5 and 2.6. These two impedance models are used in Chapter 6 to evaluate the performance of the hole-to-hole interaction end-correction expressions proposed in the current thesis.

2.1 Impedance Modeling of Perforations

Originally¹, the concept of impedance was introduced to treat alternating electrical currents [18]. Acoustic impedance is introduced similar to the impedance concept as the ratio of acoustic pressure to the acoustic volume velocity [19] or [20]

$$Z = \frac{\hat{p}}{\hat{q}}. \quad (2.1)$$

To describe the acoustic characteristics of a material, the specific acoustic impedance is used,

$$z = \frac{\hat{p}}{\hat{u}} \quad (2.2)$$

with \hat{u} the acoustic velocity normal to the surface. The characteristic impedance z_0 is the specific impedance of a fluid. The normalized specific impedance is defined by the ratio of the specific and the characteristic impedance

$$\zeta = z/z_0. \quad (2.3)$$

The normalized specific impedance is expressed in complex form,

$$\zeta = \theta + i\chi \quad (2.4)$$

where the real term represents the resistance and the imaginary term the reactance. The resistance describes the dissipation of energy, while the reactance represents the energy storage [21].

¹The content of this chapter is partially published in the paper GT2021-58535 - *Proceedings of ASME Turbo Expo 2021* [2]

Internal Impedance

Crandall [22, 23] considered the normalized specific impedance within a perforation with a unit length of l in a viscous fluid and without any end effects,

$$\zeta = \frac{1}{\sigma} ikl\Gamma(k_s r_0) \quad (2.5)$$

where ikl represents the inviscid impedance of an infinite tube. In order to convert the impedance of an individual perforation into the impedance of an array of perforations, the impedance term is divided by the porosity σ (open area ratio). The function Γ introduces the viscous effects in which $k_s^2 = -i\omega/\nu$. Crandall [22] derived the function Γ as

$$\Gamma(k_s r_0) = \left[1 - \frac{2J_1(k_s r_0)}{k_s r_0 J_0(k_s r_0)} \right]^{-1}, \quad (2.6)$$

where J_0 and J_1 are Bessel functions of the first kind. When the argument of the Bessel function is in complex form, the resulting term is in complex form, and in this case, the impedance includes real (resistive) and imaginary (reactive) terms. Based on the value of the Stokes number, $|k_s r_0|$, Equation 2.5 has two limiting values [23].

a) If $|k_s r_0| < 2$, Equation 2.5 yields [23]

$$\zeta = \frac{8\nu l}{c\sigma r_0^2} + i\frac{k}{\sigma} \left(l + \frac{1}{3}l \right). \quad (2.7)$$

The reactance $4lk/3\sigma$ has a total effective mass that is $\frac{1}{3}$ larger than the mass in the orifice per unit area [23].

b) If $|k_s r_0| > 10$, the approximation to the Bessel function ratio $J_1/J_0 = -i$ is

used [23]. Consequently, it is shown that

$$\zeta = \frac{\sqrt{2\omega\nu}l}{c\sigma r_0} + i \left(\frac{kl}{\sigma} + \frac{\sqrt{2\omega\nu}l}{c\sigma r_0} \right), \quad (2.8)$$

where both resistance and reactance terms are frequency dependent [23].

Rayleigh Conductivity

Rayleigh [6, 24] introduced the concept of acoustic conductivity based on Ohm's law in electricity. Therefore, the acoustic conductivity of a perforation is defined by the volume flow through the orifice divided by the pressure difference, and denoted as Rayleigh conductivity K_R .

Rayleigh presented the conductivity considering the oscillating pressure on each side of a perforation as $\hat{p}_1 e^{i\omega t}$ and $\hat{p}_2 e^{i\omega t}$. Then, the difference in the pressure through the perforation $(\hat{p}_1 - \hat{p}_2) e^{i\omega t}$ produces the fluctuating volume velocity $\hat{q} e^{i\omega t}$ across the orifice. For an incompressible flow and an acoustically compact orifice², therefore [6, 24]

$$\Delta\hat{p}_{orifice} = i\omega\rho \frac{\hat{q}}{K_R}, \quad (2.9)$$

where ρ stands for the density and the Rayleigh conductivity (K_R) is a complex function. The acoustic volume velocity is defined as $\hat{q} = A\hat{u}$, and \hat{u} is the acoustic particle velocity that is shown in Figure 2.1.

The Rayleigh conductivity in an ideal fluid is defined by the geometry of the perforation and for a circular perforation on a plate with an infinitesimal thickness Rayleigh proposed [6, 24]

$$K_R = 2r_0. \quad (2.10)$$

²When the characteristic length of the orifice is less than the wavelength of sound ($\lambda \gg r_0$). When the fluid is passing through the aperture due to a pressure difference, the incompressibility assumption will be satisfied if the space through which the fluid passes is small compared to the wavelength.

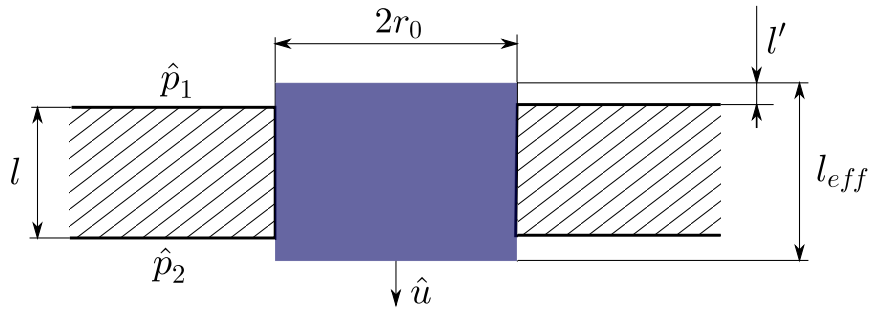


Figure 2.1: Schematic view of an orifice presenting the quantities to determine Rayleigh conductivity of an orifice.

The Rayleigh conductivity for a perforation in a wall with finite thickness can be defined as the area of the orifice divided by the effective length [6, 24]

$$K_R = \frac{A}{l_{eff}}. \quad (2.11)$$

Rayleigh derived a lower and upper limit of the conductivity [6, 24],

$$\frac{\pi r_0^2}{l + \frac{16}{3\pi} r_0} < K_R < \frac{\pi r_0^2}{l + \frac{\pi}{2} r_0}. \quad (2.12)$$

The upper limit of Equation 2.12 coincides with Equation 2.10 for a plate with an infinitesimal thickness ($l \approx 0$).

2.2 Mass End-Correction

Radiation of sound in a duct or orifice is a fundamental phenomenon in acoustics. This phenomenon results from non-planar wave creation in the vicinity of area discontinuity [25]. Modeling of the sound radiation has been a research topic since 19th century with first attempts by Helmholtz [26]. For a perforation with finite length, the effective length is greater than the geometrical length of the perforation l . The additional length l' represents the

attached mass of fluid that participates in the oscillation outside of the perforation, which is referred to as *mass end-correction*. This is depicted in Figure 2.1. The total effective length is obtained by adding the end-correction for both ends to the geometrical length of the perforation as $l_{eff} = l + 2l'$.

The mass end-correction is frequency dependent [27]. However, it can be shown that the mass end-correction is approximately constant for low frequencies when $kr_0 \ll 1$ (k being the wavenumber and r_0 inner radius of the orifice) [27–31]. Considering a duct or perforation with a radius of 2 mm and the sound speed of 340 m.s^{-1} , the assumption of low frequency is valid for frequencies much lower than 27 kHz.

The end-correction terms presented in this section are derived for plane waves with normal incidence. However, Allard [32] reported that for circular or square orifices in a square pattern, the dependence of mass end-correction on the incidence angle can be neglected. Similar observations are reported from the experimental investigation of other configurations [33, 34].

In *The Theory of Sound*, Rayleigh [6] considered a cylindrical tube with the radius of r_0 and the thickness of l , which opens in a semi-infinite space. He presents an analysis of the standing wave pattern generated by acoustic wave propagation. This analysis is limited to low frequencies when $kr_0 \ll 1$. Jaouen [35] states that analysis of Rayleigh [6] “has theoretically verified” the hypothesis of G. Wertheim [36], stating that “the origin of the standing wave pattern is not located at the boundary between the duct and the open space but is translated by a correction to the length which enables acoustic radiation of the duct in this open space” [35].

According to the axial velocity profile inside the duct (orifice), Rayleigh [6] established the mass end-correction of the perforation at large wavelengths for a constant velocity profile over the duct section

$$l' = \frac{8}{3\pi} r_0 \approx 0.85 r_0. \quad (2.13)$$

The mass end-correction of a perforation with a non-circular cross-section which opens in a semi-infinite space at low frequencies can be re-written

as [35]

$$l' = \frac{8}{3\pi^{3/2}} \sqrt{A}, \quad (2.14)$$

where A represents the area of cross-section of the perforation.

Rayleigh [6] assumes that the effect of duct length (or plate thickness in a perforated plate) does not influence the end-correction, which is shown to be correct for $l/r_0 \gg 1$ [35, 37]. For a thin plate, where the plate thickness l tends to zero, Helmholtz [26] and Rayleigh [6] demonstrated that the end-correction for a circular perforation that opens in a semi-infinite space at low frequencies is

$$l' = \frac{\pi}{4} r_0 \approx 0.785 r_0. \quad (2.15)$$

The end-correction range can be determined from the Equation 2.12 as $0.785 r_0 < l' < 0.849 r_0$. The slight difference between the end-correction expressions in Equations 2.13 and 2.15 has led Rayleigh [6] to consider the end-correction as “independent, or nearly so, of the thickness of the duct”. Likewise, Jaouen [35] interpreted this small difference as “the weak interaction between the evanescent modes inside and outside the diaphragm.”

It is worth mentioning that the expressions presented in Equations 2.13, 2.14, and 2.15 are proposed for a single perforation, which opens in a semi-infinite space, with the assumption of low frequency excitation. Several authors used the end-correction introduced in Equation 2.13 for one side of the orifice [1, 22, 23, 38–40].

Fok [41, 42] proposed an end-correction expression for an infinitely thin ($l \approx 0$) circular perforation of radius r_0 in a circular duct with the radius R_c at low frequencies,

$$l' = \frac{\pi}{4} r_0 \psi(\xi) \approx 0.785 r_0 \psi(\xi). \quad (2.16)$$

The expression $\psi(\xi)$ is obtained by the Taylor series expansion of Bessel functions for variable $\xi = \frac{r_0}{R_c}$. The variable ξ is equivalent to the square root of the porosity or open-area ratio ($\sigma = \pi r_0^2 / \pi R_c^2 = r_0^2 / R_c^2 = \xi^2$). Hereafter the expression $\psi(\xi)$ will be called “configuration function” because it relates the mass end-correction with the perforation configuration

$$\psi(\xi) = \sum_{n=0}^{12} a_n(\xi)^n, \quad (2.17)$$

where:

$$\begin{aligned} a_0 &= 1, & a_1 &= -1.40925, & a_2 &= 0, \\ a_3 &= 0.33818, & a_4 &= 0, & a_5 &= 0.06793, \\ a_6 &= -0.02287, & a_7 &= 0.03015, & a_8 &= -0.01614, \\ a_9 &= 0.01729, & a_{10} &= -0.01248, & a_{11} &= 0.01205, \\ a_{12} &= -0.00985. \end{aligned}$$

Fok [41, 42] suggested using only powers of 0, 1, 3, and 5 instead of using all terms of Equation 2.17, and rounded the coefficients to the second decimal to facilitate the calculation of the $\psi(\xi)$ as

$$\psi(\xi) = 1 - 1.41\xi - 0.34\xi^3 + 0.07\xi^5. \quad (2.18)$$

Both expressions in Equation 2.17 and 2.18 give the value equal to 0 when $\xi = 1$ (i.e. when $r_0 = R_c$). In other words, when the orifice radius r_0 is increasing and approaching the tube radius R_c , the mass end-correction tends to zero. Nesterov [43] conducted an experimental investigation on the same configuration as Fok [41, 42] and proposed a polynomial fit to his measurements based on the Fok’s expression in Equation 2.17. Nesterov [43] used only powers of 0, 1, and 3 on ξ

$$\psi(\xi) = 1 - 1.47\xi + 0.47\xi^3, \quad (2.19)$$

with the same expression for the end-correction as Fok’s, which is presented in Equation 2.16. Nesterov [43] described the validity range of his formula

as “the entire range of practical interest” and specified $0 \leq \xi = \sqrt{\sigma} \leq 0.9$. The mass end-correction expressions proposed by Fok [41, 42] and Nesterov [43] give similar results. For low area ratio (where the orifice radius is significantly smaller than the tube radius $r_0 \ll R_c$), both expressions in Equations 2.18 and 2.19 give values close to the mass end-correction calculated by Helmholtz [26] and Rayleigh [6] for a diaphragm of radius r_0 that opens in a semi-infinite space at low frequencies (shown in Equation 2.15). For the porosity approaching 1 (when the $r_0 \rightarrow R_c$), the mass end-correction tends to 0.

Initially, Ingard [44] proposed an expression of the mass end-correction for a circular orifice in a cylindrical tube. Karal [45] derived this expression independently, and in the same year, Ingard expanded his analysis to two other configurations: circular orifice in a rectangular duct, rectangular perforation in a rectangular duct [1]. These geometrical configurations are illustrated in Figure 2.2.

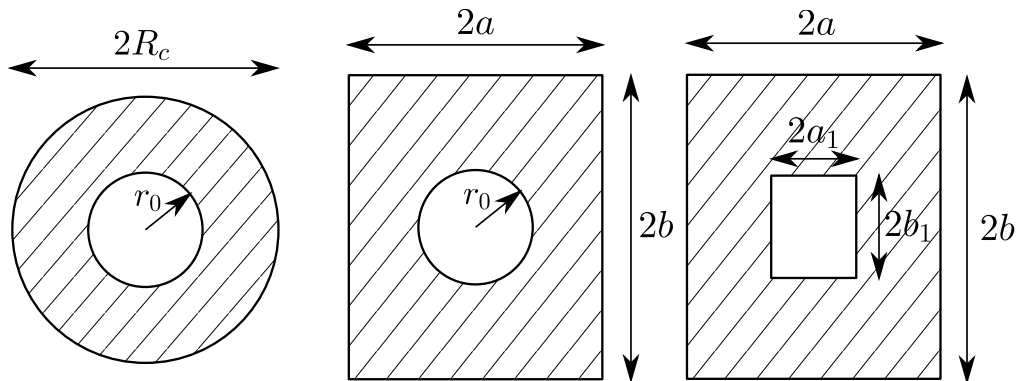


Figure 2.2: Cross-section view of the configurations studied by Ingard [1].

The expressions of the mass end-correction proposed by Ingard [1] are presented in Table 2.1. The full derivations for these geometrical configurations are presented on the APMR website [46].

The mass end-correction expression for a circular orifice in a cylindrical tube

Table 2.1: Expressions of the mass end-correction at low frequency for different perforation configurations derived by Ingard [1]. mn^* stands for a summation where mode ($m = n = 0$) is excluded and n^* represents a summation where the mode ($n = 0$) is neglected.

Configuration	Mass end-correction expression
Circular perforation in a circular tube	$l' = 4R_c \sum_{n^*} \frac{J_1^2(k_{r,mn}r_0)}{(k_{r,mn}R_c)^3 J_0^2(k_{r,mn}R_c)}$ <p>$k_{r,mn}$ being the solutions of $J_0'(k_{r,mn}R_c) = 0$</p>
Circular perforation in a rectangular tube	$l' = \frac{4\pi}{ab} \sum_{mn^*} v_{mn} \frac{J_1^2\left(r_0 \sqrt{\left(\frac{\pi m}{a}\right)^2 + \left(\frac{\pi n}{b}\right)^2}\right)}{\left[\left(\frac{\pi m}{a}\right)^2 + \left(\frac{\pi n}{b}\right)^2\right]^{3/2}}$ <p>$v_{0n} = v_{m0} = 1/2 \quad v_{mn} = 1$</p>
Rectangular perforation in a rectangular tube	$l' = \frac{4a_1b_1}{\pi ab} \sum_{mn^*} v_{mn} \frac{\left[\frac{\sin(\pi m a_1/a)}{\pi m a_1/a} \frac{\sin(\pi n b_1/b)}{\pi n b_1/b}\right]^2}{\sqrt{\frac{m^2}{a a_1} + \frac{n^2}{b b_1}}}$ <p>$v_{0n} = v_{m0} = 1/2 \quad v_{mn} = 1$</p>

proposed by Ingard [1] and Karal [45] is

$$l' = 4R_c \sum_{n^*} \frac{J_1^2(k_{r,mn}r_0)}{(k_{r,mn}R_c)^3 J_0^2(k_{r,mn}R_c)}, \quad (2.20)$$

where the values of the wavenumbers $k_{r,mn}$ are derived from rigid-wall boundary condition, which requires that the derivative of J_0 vanishes at the rigid-wall, so that $J_0'(k_{r,mn}R_c) = 0$ (J_m stands for the Bessel function of of the first kind and of order m). It is worth mentioning that Ingard [1] states that the mass end-correction of a circular perforation in a cylindrical tube approaches the same value as given in Equation 2.13, when $\xi = \frac{r_0}{R_c}$ goes to zero.

In the present study, the expression in Equation 2.20 is computed with more than 10^4 modes, and to obtain the configuration function $\psi(\xi)$, the mass end-correction is divided by the value of the end-correction acquired by Rayleigh as shown in Equation 2.13. It can be observed in Figure 2.3 that the configuration function for the circular orifice in a circular duct gives similar results as the expressions proposed by Fok and Nesterov shown in Equations 2.18 and 2.19. In addition, the configuration functions for a circular orifice in a circular duct and a square orifice in a square duct ($a = b$ and $a_1 = b_1$) are shown in Figure 2.3. The results are quite close over the range of ξ so that the curves can hardly be differentiated. Ingard [1] has already observed and pointed out this result and stated that the mass end-correction approaches zero when ξ approaches unity, except for the circular orifice in a square tube. In other words, in that case, there is a “little space left for higher-order modes to develop in the cavity around the orifice” even though the orifice diameter is equal to the tube side [1].

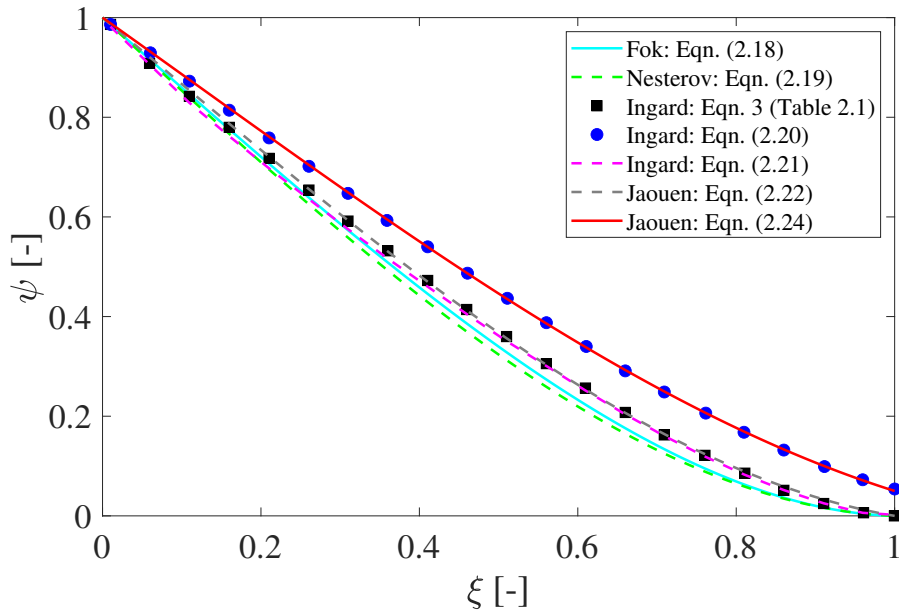


Figure 2.3: Configuration functions ψ and their fitted functions used in end-corrections as a function of ξ .

In order to avoid time-consuming computation of the mass end-correction expressions, Ingard [1] proposed an approximation as shown in Equation 2.21.

This approximation is valid at a low perforation rate (porosity) for two configurations: circular orifice in a circular duct and square perforation in a square duct

$$l' = \frac{8r_0}{3\pi} (1 - 1.25\xi) = \frac{8r_0}{3\pi} \psi(\xi), \quad (2.21)$$

where $\xi = a_1/a$ for a square orifice in a square tube and $\xi = r_0/R_c$ for a circular orifice in a cylindrical duct. The validity range proposed by Ingard is $\xi < 0.4$, which corresponds to a porosity range of $\sigma < 0.16$. Jaouen and Chevillotte [35] proposed a fit of Ingard's results for a square orifice in a square duct to overcome the low porosity limitation. This fitted function has the validity range of $0 \leq \xi \leq 1$ and can be applied to a circular orifice in a cylindrical duct [35] (as Ingard mentioned that this function can be used for both configurations because of the close results),

$$l' = \frac{8r_0}{3\pi} \psi(\xi) = \frac{8r_0}{3\pi} (1 - 1.33\xi - 0.07\xi^2 + 0.4\xi^3). \quad (2.22)$$

In *Propagation of sound in porous media*, Allard [32] introduced an expression for a circular orifice in a square duct

$$l' = \frac{8r_0}{3\pi} \psi(\xi) = \frac{8r_0}{3\pi} (1 - 1.14\xi), \quad (2.23)$$

with the validity range of $\xi < 0.4$, which corresponds to a porosity range of $\sigma < 0.13$ (where $\sigma = \pi r_0^2 / (2a)^2 = \pi \xi^2 / 4$).

Jaouen et al. [47] experimentally characterized perforated plates and introduced a fitted function to Ingard's theoretical results for a circular orifice in a square duct

$$l' = \frac{8r_0}{3\pi} \psi(\xi) = \frac{8r_0}{3\pi} (1 - 1.13\xi - 0.09\xi^2 + 0.27\xi^3), \quad (2.24)$$

with the validity range of $0 \leq \xi \leq 1$.

This section aimed to present the mass end-correction expressions which are widely used in the literature. Before studying the hole-to-hole interaction effect, it is required to differentiate the mass end-correction from the hole-to-hole interaction effect. Because several authors inappropriately used mass end-correction expressions to represent the hole-to-hole interaction effect. This section presented the origin of mass end-correction expressions and the major assumption behind their derivation, which is considering a single orifice in the plate. Therefore, none of the expressions that are presented in this section can be used to consider the hole-to-hole interaction effect.

2.3 Hole-to-hole Interaction

In the previous section, several mass end-correction expressions are presented that are originally proposed for a single orifice in the plate. Several authors used these end-correction expressions for multi-orifice perforated plates and assumed that the propagation of sound in an orifice is acting individually and not depending on its neighboring orifices as the orifice dimensions are smaller than the acoustic wavelength. Ingard [1] presented an analysis that shows that the hole-to-hole interaction has an additional effect on the mass end-correction, when there are multiple orifices in the plate.

Ingard [1] investigated the effect of hole-to-hole interaction by considering two orifices in a plate that open in a semi-infinite space. He started his analysis by considering an eccentric orifice that is not located in the center of the tube and obtained the mass end-correction for this case

$$l'_{11} = 4R_c \sum_{mn^*} \frac{J_1^2(k_{r,mn}r_0) J_m^2(k_{r,mn}d_i)}{(k_{r,mn}R_c)^3 \left(1 - \frac{m^2}{(k_{r,mn}R_c)^2}\right) J_m^2(k_{r,mn}R_c)}, \quad (2.25)$$

where d_i stands for the distance between the orifice center and the tube center. The subscript 11 stands for the effect of the first orifice on itself. The expression for mass end-correction of a circular orifice in a cylindrical tube presented in Equation 2.20 is a particular case of the orifice eccentricity where

the center-to-center distance is zero ($d_i = 0$). Therefore, the expression presented in Equation 2.25 is a general form of the expression in Equation 2.20. Furthermore, Ingard [1] introduced the interaction impedance of two adjacent circular orifices in a circular tube at low frequency by calculating “the pressure caused by the first orifice at the surface of the second orifice.” Ingard [1] assumed the mass end-correction for each orifice in this configuration is composed of the effect of the orifice on itself, which corresponds to the mass end-correction of a single orifice, and the effect of the second orifice ($l' = l'_{11} + l'_{12}$). Ingard [1] obtained the mass end-correction expression that accounts for the effect of the second orifice on the first orifice

$$l'_{12} = 4R_c \sum_{mn^*} \frac{(-1)^m J_1^2(k_{r,mn} r_0) J_m^2(k_{r,mn} d_i)}{(k_{r,mn} R_c)^3 \left(1 - \frac{m^2}{(k_{r,mn} R_c)^2}\right) J_m^2(k_{r,mn} R_c)}, \quad (2.26)$$

where the subscript 12 stands for the effect of the second orifice on the first orifice.

Ih [48] extended the theoretical approach of Ingard [1] by considering two rectangular perforations in a rectangular tube and two perforations (one circular and one rectangular) in a rectangular tube. In addition to the situation that orifices open in a semi-infinite space, he studied the “apertures in an axially finite tube” and introduced an expression for mass end-correction. To the knowledge of the author, only Ingard [1] and Ih [48] theoretically investigated the hole-to-hole interaction effect. However, these studies are limited to two perforations in a duct.

Tayong [49, 50] experimentally investigated the effect of interacting orifices for a multi-orifice perforated plate and proposed a “geometrical tortuosity model” to consider the effect of the acoustic radiation of the perforated region, which is called “heterogeneity distribution effects.” However, the exact definition of parameters such as tortuosity in his model is not known a priori and requires external input, which he acquired from experiments. Wang et al. [51] investigated the effect of hole-to-hole interaction on the resonance frequency of distributed Helmholtz resonators by a series of highly resolved computational fluid dynamics simulations. They performed a regression analysis

of the results and proposed a model to predict acoustic resonance frequency,

$$l' = 0.48r_0\sqrt{\pi} + 0.48\sqrt{A_{open}}(0.78\sqrt{\sigma_{eff}} - 0.11), \quad (2.27)$$

where A_{open} stands for the overall open area of all orifices and σ_{eff} is the effective porosity, which is the ratio of the opening area of an orifice and the area of a rectangular region associated to that orifice.

The model proposed by Wang is obtained from perforated plates that are limited to a specific orifice-tube radius ratio ($\xi = r_0/R_c = 0.022$), while the effect of ξ on the mass end-correction is reported by several authors [1, 41, 43, 52].

2.4 Howe's Rayleigh Conductivity Model

Howe [53, 54] proposed a model based on Rayleigh conductivity [6, 24] for an orifice, considering the shedding of vorticities from the rim of the orifice. He treated a circular orifice with bias flow in a wall with an infinitesimal thickness. He considered the acoustic absorption by vortex shedding neglecting the viscosity except at the rims of the aperture. The Reynolds number is considered to be adequately high so that the viscous dissipation is small, and its contribution is limited to generate vorticity at the rims of the orifice. In the presence of mean flow (bias flow), the acoustic energy is transformed into energy of fluctuating vorticity generated at the rim of the aperture and swept downstream, transferring the energy into heat. This energy conversion mechanism considers the increase in the acoustic resistance of the orifice as the bias flow velocity increases. The generated vortex is considered to have a convection velocity equal to the mean flow velocity through the perforation, and the radius of the vortex rings remains constant, traveling downstream. A summary of the assumptions is presented as follows:

- Low frequency, such that the wavelength is greater than the radius of the orifice: $\lambda \gg r_0$.

- Low Mach number, such that the fluid can be regarded as incompressible fluid: $M_B \ll 1$.
- Infinitely thin wall: $l \approx 0$.
- High bias flow Reynolds number, such that viscosity is solely taken into account at the orifice edges $U_B r_0 / \nu \gg 1$.

For these constraints, Howe [53, 54] presented the conductivity of an orifice,

$$K_R = 2r_0(\gamma + i\delta), \quad (2.28)$$

where

$$\gamma + i\delta = 1 + \frac{\frac{\pi}{2} I_1(St) e^{-St} + i K_1(St) \sinh(St)}{St [\frac{\pi}{2} I_1(St) e^{-St} - i K_1(St) \cosh(St)]}. \quad (2.29)$$

Equation 2.29 is a function of the Strouhal number only and calculated based on the vorticity convection velocity and the orifice radius. Figure 2.4, shows the dependency of the real and imaginary terms of Equation 2.29 on Strouhal number. δ stands for the acoustic absorption, and the inertia of the orifice is denoted as γ .

At higher Strouhal numbers, the shedding of vorticity has a negligible effect since induced velocities due to successive vortex rings diminish rapidly. On the other hand, at a low Strouhal number, generated vorticity can stretch downstream. This behavior is illustrated by the imaginary part of Equation 2.29 with its maximum at the Strouhal number just beyond unity.

One shortcoming of Howe's model is assuming an infinitesimal wall thickness, which is not practical.

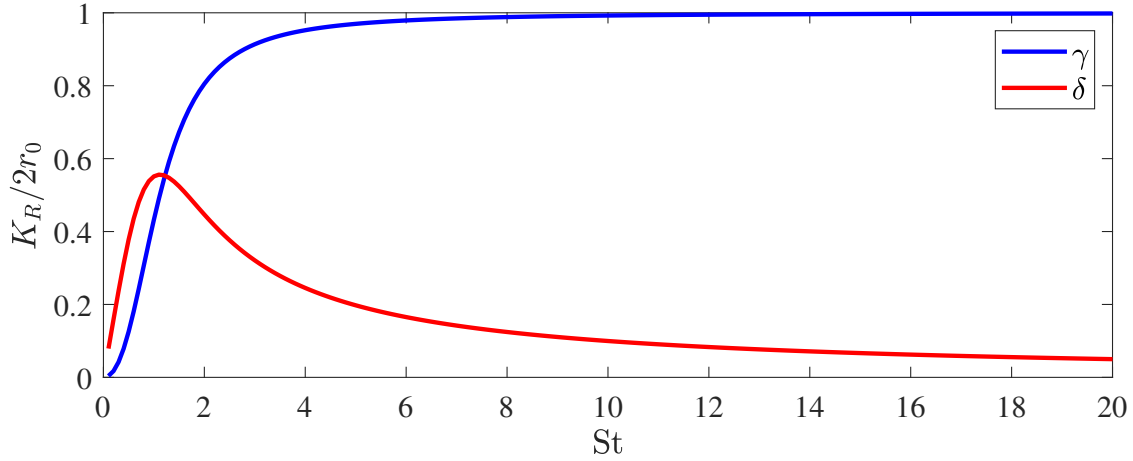


Figure 2.4: Real term γ and imaginary term δ of the normalized Rayleigh conductivity plotted as a function of the Strouhal number.

2.5 Jing's Impedance Model

Jing and Sun [16] extended Howe's Rayleigh conductivity model to include orifices with a finite length and expressed Howe's Rayleigh conductivity model in terms of the normalized specific impedance ζ . For a circular perforation with finite thickness in the presence of a bias flow, they considered the effect of thickness by adding an additional term, ikl . The impedance yields

$$\zeta_{Jing} = \frac{k\pi r_0 \delta}{2(\gamma^2 + \delta^2)} + i \left(\frac{k\pi r_0 \gamma}{2(\gamma^2 + \delta^2)} + kl \right). \quad (2.30)$$

The effect of viscosity is neglected in their model, and the thickness effect is included only in the reactance term.

2.6 Bellucci's Impedance Model

Bellucci et al. [8, 17] proposed an impedance model for perforated screens for the range of the nonlinear regime (in the absence of the bias flow) to the linear regime (the velocity of the bias flow is higher than the acoustic velocity).

Their impedance model is based on Crandall's impedance model [22] which is presented in Equation 2.5. However, the thermal conductivity losses are not considered. Their assumptions can be summarized as follows:

- Helmholtz number of the orifice $He < 0.08$.³
- Mach number inside the orifice $M_B < 0.02$.
- Smaller orifice radius compared to the wavelength (the orifice is acoustically compact).
- Sufficiently high Shear number.⁴

They used different sub-models in the resistance term to include the bias flow effect and the non-linearity due to high amplitudes. The resistance term of Bellucci et al. [8] yields

$$\theta_{Bellucci} = \frac{\varepsilon}{c\sigma} G \left(\frac{U_B}{|\hat{u}|} \right) |\hat{u}|, \quad (2.31)$$

where ε , which stands for pressure loss coefficient, is calculated as follows:

$$\varepsilon = \begin{cases} 1/C_d^2 & \text{if } U_B = 0, St_{ac} \leq (St_{ac})_{qs} \\ 0.6 \left(\frac{3\pi}{4} \right) St_{ac}^{1/3} & \text{if } U_B = 0, St_{ac} > (St_{ac})_{qs} \\ \frac{\pi}{2} \frac{\delta St}{\gamma^2 + \delta^2} & \text{if } U_B \geq |\hat{u}| \\ \frac{\varepsilon_{nonlin}(1-G) + \varepsilon_{lin}(G - \frac{4}{3\pi})}{1 - \frac{4}{3\pi}} & \text{if } 0 < U_B < |\hat{u}| \end{cases}. \quad (2.32)$$

In Equation 2.32, ε_{nonlin} in the fourth expression corresponds to the first and second expressions in Equation 2.32, depending on St_{ac} . In the fourth expression of Equation 2.32, ε_{lin} refers to the third expression with γ and δ , which are

³Orifice length Helmholtz number $kl \ll 1$ means that changes in the density due to pressure variation in time is negligible.

⁴Shear number $Sh = r_0 \sqrt{\frac{\omega}{\nu}}$ represents the hole radius r_0 divided by the acoustic boundary layer thickness $\sqrt{\frac{\nu}{\omega}}$.

the real and imaginary parts of Howe's Rayleigh conductivity, respectively. The threshold of the quasi-steady assumption for the acoustic Strouhal number is defined by $(St_{ac})_{qs} = 0.61/C_d^6$.

In Equation 2.31, $G(x)$ is proposed as:

$$G(x) = \begin{cases} \frac{2}{\pi} \left(x \cdot \arcsin(x) + \frac{\sqrt{1-x^2}}{3} (2+x^2) \right) & \text{if } |x| \leq 1 \\ |x| & \text{if } |x| > 1 \end{cases}. \quad (2.33)$$

When $U_B > |\hat{u}|$, Equation 2.31 reduces to the linear expression $\theta_{Bellucci} = \frac{\varepsilon}{c\sigma} U_B$. For large $|\hat{u}|$ and for $U_B < |\hat{u}|$, Equation 2.31 predicts a nonlinear behavior of pressure losses [8, 17]. When bias flow is present, the resistance term in this model is based on Howe's Rayleigh conductivity model.

The impedance model of Bellucci et al. [8, 17] is based on Crandall's impedance model [22]. Additionally, they included different correction length to Crandall's impedance model, which yields

$$\chi_{Bellucci} = \frac{k}{\sigma} \left(l\Gamma + l'_{Bellucci} \right). \quad (2.34)$$

Bellucci et al. [8, 17] used the asymptotic value of $-i$ for J_1/J_0 in Equation 2.6, and proposed expressions to calculate Γ based on the value of the Shear number as follows [55]:

$$\Gamma = \left(\frac{4}{3} - i \frac{8}{Sh^2} \right) \quad Sh < 1, \quad (2.35)$$

$$\Gamma = \left[\frac{4}{3} \left(1 + \frac{1}{\sqrt{9 + \frac{Sh^2}{2}}} \right) - i \frac{8}{Sh^2} \sqrt{1 + \frac{Sh^2}{32}} \right] \quad 1 < Sh < 10, \quad (2.36)$$

$$\Gamma = \left[\left(1 + \frac{\sqrt{2}}{Sh} \right) - i \left(\frac{\sqrt{2}}{Sh} \right) \right] \quad 10 < Sh. \quad (2.37)$$

Bellucci used the approximation of Γ function for higher shear numbers, according to Equation 2.37. The function Γ accounts for the viscosity effects and is composed of real and imaginary parts, which leads to considering the effect of viscosity in both resistance and reactance terms, Equations 2.31 and 2.34 respectively.

In Equation 2.34, $l'_{Bellucci}$ accounts for the end-correction length, including contributions from the radiation reactance (l'_{rad}), the orifice interaction (l'_{int}), the bias flow (l'_B), and nonlinear effects due to high amplitude excitation (l'_{nl}). Considering the end-correction length for both sides of the orifice yields

$$l'_{Bellucci} = l'_{rad} \cdot l'_{int} \cdot l'_B \cdot l'_{nl}, \quad (2.38)$$

where

$$l'_{rad} = 2 \cdot 0.8216r_0 \left(1 + \frac{(0.77He)^2}{1 + 0.77He} \right)^{-1}, \quad (2.39)$$

$$l'_{int} = 1 - \sqrt{\frac{\sigma}{2}}, \quad (2.40)$$

$$l'_B = \frac{0.3(6.0/St^2) + 1}{6.0/St^2 + 1}, \quad (2.41)$$

$$l'_{nl} = 1 - 0.3/St_{ac}^{0.6}. \quad (2.42)$$

Bellucci et al. [8, 17] considered the hole-to-hole interaction effect using the expression presented in Equation 2.40. This expression is proposed for a single orifice and, therefore, is inappropriately used in Bellucci model to consider the hole-to-hole interaction effect, as mentioned earlier in this chapter. To include the reduction of end-correction due to high-amplitude oscillations and bias flow, the terms l'_{nl} and l'_B are fitted to the experimental measurements [8].

Bellucci et al. [8] included the effect of the back cavity in their proposed impedance model by introducing an additional term, $i \cot(kL_c)$, where L_c

stands for the cavity length. In the presence of a back cavity and considering the plane wave propagation into the back cavity, their impedance model yields

$$\zeta_{Bellucci} = \frac{\varepsilon}{c\sigma} G\left(\frac{U_B}{|\hat{u}|}\right) |\hat{u}| + \frac{ik}{\sigma} (l\Gamma + l'_{Bellucci}) - i \cot(kL_c). \quad (2.43)$$

Bellucci et al. [8] investigated the perforated plate with normal sound incidence and compared the model prediction with experimental data. The results agree well with the measurements for both the zero bias flow regime and linear regime (where the bias flow velocity exceeds the acoustic velocity) over a wide range of orifice radii, wall thicknesses, and bias flow velocities.

3 Modeling Approach

Following¹ the discussion in Section 2.2, all the mass end-correction terms, that are presented in Section 2.2, are developed with the assumption of a single orifice in the center of a duct. These terms have been used inappropriately for multi-orifice perforated plates by several authors [8, 23, 56]. The hole-to-hole interaction end-correction expressions proposed by Ingard [1] and Ih [48] are limited to two-hole configurations. Therefore, a comprehensive analysis of the hole-to-hole interaction effect in multi-orifice perforated plates is required to develop a correct analytical approach.

This chapter presents the theoretical background required for the modeling of hole-to-hole interaction effect, followed by the hole-to-hole interaction modeling approach.

3.1 Theoretical Background

This section starts with the derivation of the one-dimensional acoustic wave equation, followed by the three-dimensional acoustic wave equation, which is essential for the modeling of the hole-to-hole interaction effect.

3.1.1 Acoustic Wave Equation

Fluid Dynamics Equations

The conservation laws for mass, momentum, and energy govern the motion of a fluid. The continuity equation, which relates the fluid's velocity to its density,

¹The content of this chapter is partially published in the paper GT2021-58535 - *Proceedings of ASME Turbo Expo 2021* [2]

is given by [20, 57, 58]

$$\frac{\partial \rho}{\partial t} + \nabla \cdot (\rho \mathbf{u}) = 0. \quad (3.1)$$

Rewriting this equation by substituting the local time derivative $\partial/\partial t$ with the substantial derivative [58–60]

$$\frac{D}{Dt} = \frac{\partial}{\partial t} + \mathbf{u} \nabla. \quad (3.2)$$

Equation 3.1 leads to [58]

$$\frac{D\rho}{Dt} + \rho(\nabla \cdot \mathbf{u}) = 0. \quad (3.3)$$

For an inviscid fluid, the conservation of momentum where gravity is neglected can be cast in [20, 57, 58]

$$\rho \frac{D\mathbf{u}}{Dt} = -\nabla p. \quad (3.4)$$

This equation is known as the Euler equation that presents the relationship between the fluid's velocity and pressure.

The conservation of energy is expressed by the ideal gas law [58, 61]

$$p = \rho R_g T. \quad (3.5)$$

By assuming that the acoustic wave is isentropic, the relation between the density and the pressure can be given by [20, 58]

$$\left(\frac{\partial p}{\partial \rho} \right)_s = c^2 \quad \text{with} \quad \frac{Ds}{Dt} = 0. \quad (3.6)$$

The system of these three Equations 3.1, 3.4, and 3.6 describes the motion of a compressible, ideal fluid and is commonly known as the system of Euler equations.

Linear Acoustics Equations

The quantities such as pressure, velocity, and density can be expressed by the sum of their mean and acoustic perturbation values:

$$\begin{aligned} p &= p_0 + p' \\ u &= u_0 + u' \\ \rho &= \rho_0 + \rho' \end{aligned} \quad (3.7)$$

The Euler equations (3.1, 3.4, and 3.6) can be linearized by assuming that the acoustic perturbations are smaller than the mean values

$$\frac{p'}{p_0} \ll 1 \quad \frac{u'}{c} \ll 1 \quad \frac{\rho'}{\rho_0} \ll 1. \quad (3.8)$$

By using these assumptions, higher-order terms in Equations 3.1, 3.4, and 3.6 can be excluded. The acoustic equations using these approximations are given by [20, 62]

$$\frac{D\rho'}{Dt} + \rho_0 (\nabla \cdot \mathbf{u}') = 0, \quad (3.9)$$

$$\rho_0 \frac{D\mathbf{u}'}{Dt} + \nabla p' = 0, \quad (3.10)$$

$$p' = c^2 \rho'. \quad (3.11)$$

Acoustic Wave Equation

The acoustic wave equation can be derived from Equations 3.9, 3.10, and 3.11.

$$\nabla^2 p' - \frac{1}{c^2} \frac{D^2 p'}{Dt^2} = 0. \quad (3.12)$$

The summary of the assumptions that are used in the derivation are:

- Inviscid fluid.
- Isentropic relation between pressure and density.
- Homogeneous medium (i.e., a medium with spatially uniform properties [21]).
- Linear acoustics (the amplitude of oscillation is small, in such a way that the relation between any two perturbing quantities is not amplitude-dependent [21]).

Equation 3.12 in stationary medium ($u_0 = 0$) reduces to the well known acoustic wave equation [20, 63, 64]

$$\nabla^2 p' - \frac{1}{c^2} \frac{\partial^2 p'}{\partial t^2} = 0. \quad (3.13)$$

Similar to the wave equation that is given for the acoustic pressure, the wave equation can be written for all acoustic quantities such as velocity and density because all coefficients remain constant [65].

3.1.2 Three-Dimensional Waves

To describe the wave propagation in a cylindrical tube, the wave equation 3.12 can be written in cylindrical coordinates. z is the axial coordinate, r is the ra-

dial coordinate, and the circumferential coordinate is denoted by θ . Therefore, the three-dimensional wave equation in cylindrical coordinates gives

$$\frac{\partial^2 p'}{\partial z^2} + \frac{1}{r} \frac{\partial}{\partial r} \left(r \frac{\partial p'}{\partial r} \right) + \frac{1}{r^2} \frac{\partial^2 p'}{\partial \theta^2} - \frac{1}{c^2} \frac{D^2 p'}{Dt^2} = 0. \quad (3.14)$$

This linear second-order partial differential equation can be solved by the separation of variables. A general solution for the time-harmonic wave propagation in a cylindrical tube with the rigid walls is given by (e.g. [66–69])

$$\hat{p}_{mn}(z, r, \theta, t) = (\hat{p}_{mn}^+ e^{-ik_{z,mn}z} + \hat{p}_{mn}^- e^{ik_{z,mn}z}) J_m(k_{r,mn}r) e^{im\theta} e^{i\omega t}. \quad (3.15)$$

Equation 3.15 represents the so-called modal solution. The first and second terms on the right-hand side of the Equation 3.15 describe the shape of the mode in axial and radial directions. The third term represents the circumferential shape of the mode, and the fourth term gives the temporal mode shape. The axial, circumferential, and temporal mode shapes are sinusoidal, while the radial mode shape is given by Bessel functions. J_m stands for the Bessel function of the first kind. The sound pressure of a time-harmonic wave is obtained by the real part of the summation of an infinite number of modes

$$p'(z, r, \theta, t) = \sum_m \sum_n \hat{p}_{mn}(z, r, \theta, t), \quad (3.16)$$

where $m \in \{\dots, -2, -1, 0, 1, 2, \dots\}$ is the circumferential mode order and $n \in \{0, 1, 2, \dots\}$ is the radial mode order. For $m = 0$ and $n = 0$ the sound field is one-dimensional, which varies along the z -direction only. This particular case is referred to as plane wave or fundamental mode, and all other modes are known as higher-order modes.

The relation between axial and radial wave numbers in Equation 3.15 is

$$\left(\frac{\omega}{c} \right)^2 = k_{z,mn}^2 + k_{r,mn}^2, \quad (3.17)$$

where the axial wave number is given by

$$k_{z,mn}^{\pm} = \frac{k}{1 - M_B^2} \left(-M_B \pm \sqrt{1 - (1 - M_B^2) \left(\frac{b_{mn}}{kR_c} \right)^2} \right). \quad (3.18)$$

The rigid-wall boundary condition requires that the radial component of the acoustic velocity diminishes at the wall. Following Equation 3.10, the acoustic pressure boundary condition at $r = R_c$ is

$$\frac{\partial p'}{\partial r} = 0. \quad (3.19)$$

Therefore, the derivative of J_m must vanish at the rigid-wall, such that for $r = R_c$

$$J'_m(k_{r,mn}R_c) = 0, \quad (3.20)$$

with the radial wave number

$$k_{r,mn} = \frac{b_{mn}}{R_c}, \quad (3.21)$$

and b_{mn} the n -th root of J'_m for the rigid-wall boundary condition.

The propagation of a mode in z -direction is defined by the axial wave number $k_{z,mn}^{\pm}$. The propagation characteristics depends on the value of the square root in Equation 3.18. Two different cases occur depending on the axial wave number:

1. $k_{z,mn}^{\pm}$ is a real quantity when: $1 - (1 - M_B^2) \left(\frac{b_{mn}}{kR_c} \right)^2 \geq 0$
2. $k_{z,mn}^{\pm}$ is a complex quantity when: $1 - (1 - M_B^2) \left(\frac{b_{mn}}{kR_c} \right)^2 < 0$

In the first case, the mode propagates along the duct without being attenuated (in the inviscid case). In the second case, the imaginary part of $k_{z,mn}^{\pm}$ behaves

as an attenuation coefficient. Therefore, the mode can not propagate, and its amplitude will be decayed exponentially based on its axial distance from the source. By increasing frequency to a threshold, this mode may not decay anymore and can propagate. This threshold frequency, at which a mode starts propagating, is referred to as "Cut-on" frequency. At this particular frequency, the value of the square root in Equation 3.18 becomes zero, such that

$$f_{c,mn} = \frac{b_{mn}}{2\pi R_c} c \sqrt{1 - M_B^2}. \quad (3.22)$$

For each mode, the cut-on frequency is related to the tube diameter (radius), the Mach number of the flow, the sound speed, and the b_{mn} of that particular mode. b_{mn} is equal to zero for the plane wave (so called fundamental mode (0:0)), and following the same analogy, the cut-on frequency is also zero, which implies that the fundamental mode can propagate at all frequencies. The first higher-order mode has the lowest cut-on frequency among the higher-order modes. The cut-on frequency of the first higher-order mode (1:0) is referred to as the frequency where the transition between one-dimensional and three-dimensional sound propagation occurs. The non-propagating modes which are being attenuated are known as evanescent modes or cut-off modes.

One major advantage of the decaying higher-order mode is that only a finite number of higher-order modes can propagate at a specific frequency, and the remaining modes that are not propagating can be neglected in most cases.

3.1.3 Plane Waves

At low frequencies below the cut-on frequency of the first higher-order mode, the wave propagates in one dimension (z -direction). The quantities of the acoustic field for a wave traveling in the z -direction are constant in any cross-section of a constant-area duct. The acoustic wave equation 3.12 for plane

waves is given by [20]

$$\frac{\partial^2 p'}{\partial z^2} - \frac{1}{c^2} \frac{D^2 p'}{Dt^2} = 0. \quad (3.23)$$

The general solution is given by [20, 63, 64, 69]

$$p'(z, t) = f_1\left(t - \frac{z}{c}\right) + f_2\left(t + \frac{z}{c}\right), \quad (3.24)$$

where f_1 and f_2 are functions with continuous first and second-order derivatives. The equation presents two plane waves that are traveling with the speed c in opposite directions.

Applying f_1 and f_2 approximated by a Fourier series to Equation 3.24 and taking the real part of the expression yields the well-known notation [38, 69]

$$p'(z, t) = (\hat{p}^+ e^{-ikz} + \hat{p}^- e^{ikz}) e^{i\omega t}. \quad (3.25)$$

Equation 3.25 represents the time-dependent acoustic pressure distribution of a single frequency plane wave in a stationary medium.

By introducing a mean flow in the z -direction, the speed at which the wave is propagating varies. In the direction of the mean flow, the mean flow velocity is added to the propagation speed c , and it is reduced from the propagation speed c in the opposite direction of the mean flow i.e. $c \pm u_0$. This convective effect of the mean flow is considered in the wave number

$$k^\pm = \frac{\omega}{c(1 \pm M_B)}. \quad (3.26)$$

The superscript + describes in the direction of the mean flow and superscript – describes in the opposite direction of the mean flow. Equation 3.25 becomes [69, 70]

$$p'(z, t) = (\hat{p}^+ e^{-ik^+z} + \hat{p}^- e^{ik^-z}) e^{i\omega t}. \quad (3.27)$$

3.2 Modeling for Two and Multiple Holes

This section presents the modeling approach for the hole-to-hole interaction effect in a multi-orifice perforated plate.

Selamet et al. [71] developed a three-dimensional analytical approach to evaluate the acoustic absorption performance of circular asymmetric Helmholtz resonators. This method is employed to study the influence of the neck offset from the center of the cavity on the resonance frequency and on acoustic damping. In this section, a similar approach is implemented and extended to multi-orifice perforated plates.

In the current thesis, a multi-orifices perforated plate, as shown in Figure 3.1, is studied.

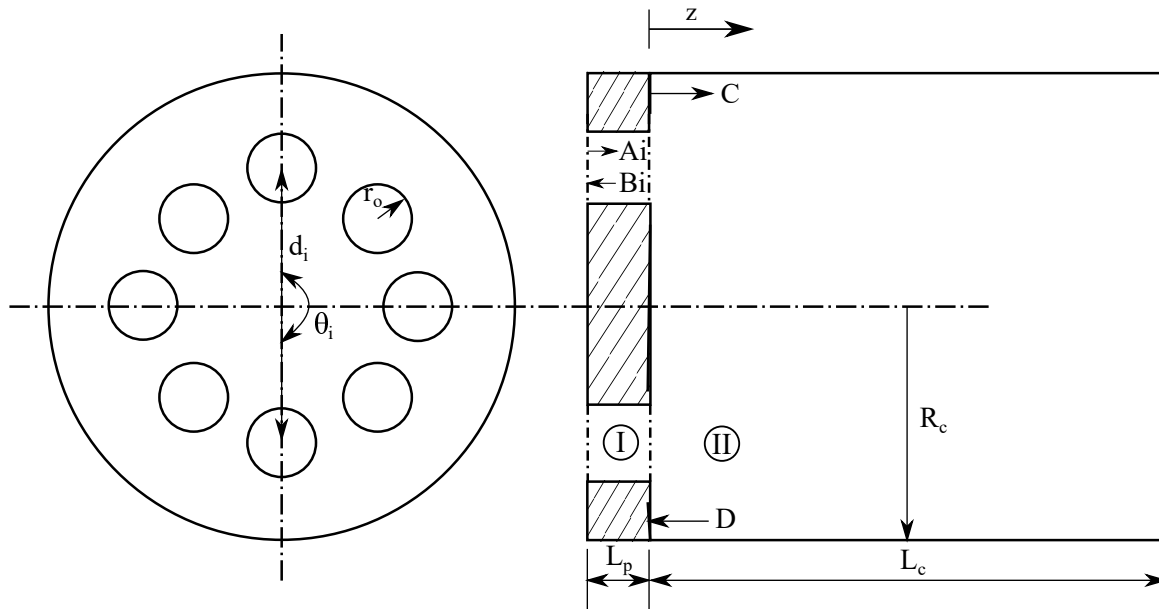


Figure 3.1: Schematic view of the domain consisting of a plate and a cavity.

Before presenting the modeling approach, it is required to introduce the basic concepts that are used in the modeling as follows:

- As it is shown in Figure 3.1, the cavity domain is coupled with a set of short tubes, which are the orifices in the perforated plate.

- There is no restriction concerning the size and placement of the orifices.
- The idea behind the modeling is to employ the analytical solutions of the wave equation in the cavity and in the tubes (orifices in the perforated plate), and couple them at the interface plate $z = 0$.
- One main assumption is imposing a constant velocity on the cross-section of all holes (A_h) at $z = -L_p$ as the boundary condition, although the velocity may not be constant over the hole's cross-section and for all orifices. Without making this assumption, it is required to include an additional tube on the other side of the perforated plate, which includes the excitation source, and couple the domain with the cavity domain via a set of short tubes. The assumption of constant velocity is made to avoid the excessive computational cost associated with the coupling of the additional tube and the excitation source. Besides, it will be presented that even with imposing such a boundary condition, the mass end-correction can be obtained.
- The analytical solutions of the wave equation are for all types of modes in the tubes and the cavity. This is the main point, because incorporating higher-order modes in the cavity is essential for the coupling at the interface plane A_h and $(A_p - A_h)$. Without higher-order modes there will be no solution after coupling which results in the calculation of end-correction.
- Finally, the axial mode is examined and from that mode the end-correction is extracted for different hole patterns.

For the three-dimensional acoustic waves propagating in a quiescent fluid in a cylindrical tube, the governing equation is the Helmholtz equation [69]

$$\nabla^2 \hat{p} + k^2 \hat{p} = 0, \quad (3.28)$$

where \hat{p} stands for the fluctuating pressure and $k = \omega/c$ represents the wave number. By employing the separation of variables, the general solution for

$\hat{p}(r, z, \theta)$ in the cavity (Figure 3.1) can be written as [69]

$$\hat{p}_{\text{cavity}} = C_{00}e^{-ikz} + D_{00}e^{ikz} + \sum_{m^*}^{\infty} \sum_{n^*}^{\infty} \left(C_{mn}e^{ik_{z,mn}^{II}z} + D_{mn}e^{-ik_{z,mn}^{II}z} \right) J_m(k_{r,mn}^{II}r) e^{im\theta} \quad (3.29)$$

where C_{mn} and D_{mn} are constants associated with the waves propagating in the positive and negative z -direction, as shown in Figure 3.1. The $*$ on the summation sign implies that the plane wave ($m = 0, n = 0$) is neglected in the summation, while the plane wave is represented by the first two terms on the right hand side of Equation 3.29. The reason that ($m = 1, n = 1$) are not used instead of m^* and n^* in the summation is that by using ($m = 1, n = 1$), modes ($0 : 1$) and ($1 : 0$) will be excluded from the summation, while m^* and n^* implies that all the modes are considered in the summation except the fundamental mode ($0 : 0$). J_m is the Bessel function of the first kind of order m . Superscript II represents the cavity to differentiate it from the region of the holes that is denoted by I . The rigid-wall boundary condition requires for $r = R_c$ requires

$$J'_m(k_{r,mn}^{II}R_c) = 0, \quad (3.30)$$

where

$$k_{r,mn}^{II} = \frac{b_{m,n}}{R_c}. \quad (3.31)$$

The axial wavenumber of the (m, n) mode

$$k_{z,mn}^{II} = k \left[1 - \left(\frac{b_{m,n}}{kR_c} \right)^2 \right]^{1/2} \quad (3.32)$$

will be imaginary for any high-order mode when $k < k_{r,mn}^{II}$. Similarly, the solu-

tion for $\hat{p}(r, z, \theta)$ inside each orifice can be written as

$$\begin{aligned} \hat{p}_{\text{hole}} = & Ai_{00}e^{-ikz} + Bi_{00}e^{ikz} + \\ & \sum_{m^*}^{\infty} \sum_{n^*}^{\infty} \left(Ai_{mn}e^{ik_{z,mn}^I z} + Bi_{mn}e^{-ik_{z,mn}^I z} \right) J_m(k_{r,mn}^I r) e^{im\theta}. \end{aligned} \quad (3.33)$$

Ai_{mn} and Bi_{mn} are constants associated with the waves propagating in the positive and negative z -direction inside the i -th orifice.

The rigid-wall boundary condition requires for $r = r_0$

$$J'_m(k_{r,mn}^I r_0) = 0, \quad (3.34)$$

where

$$k_{r,mn}^I = \frac{b_{m,n}}{r_0}, \quad (3.35)$$

with the axial wave number of the (m, n) mode

$$k_{z,mn}^I = k \left[1 - \left(\frac{b_{m,n}}{kr_0} \right)^2 \right]^{1/2}. \quad (3.36)$$

The axial particle velocity $\hat{u}(r, z, \theta)$ is obtained from the momentum equation $i\rho\omega\hat{u} = -\nabla^2\hat{p}$. Inside the cavity

$$\begin{aligned} \hat{u}_{\text{cavity}} = & \frac{1}{\rho\omega} \left[kC_{00}e^{-ikz} - kD_{00}e^{ikz} - \right. \\ & \left. \sum_{m^*}^{\infty} \sum_{n^*}^{\infty} \left(k_{z,mn}^{II} C_{mn} e^{ik_{z,mn}^{II} z} - k_{z,mn}^{II} D_{mn} e^{-ik_{z,mn}^{II} z} \right) J_m(k_{r,mn}^{II} r) e^{im\theta} \right] \end{aligned} \quad (3.37)$$

is obtained and similarly for inside the orifices

$$\hat{u}_{\text{hole}} = \frac{1}{\rho\omega} \left[kAi_{00}e^{-ikz} - kBi_{00}e^{ikz} - \sum_{m^*}^{\infty} \sum_{n^*}^{\infty} \left(k_{z,mn}^I Ai_{mn} e^{ik_{z,mn}^I z} - k_{z,mn}^I Bi_{mn} e^{-ik_{z,mn}^I z} \right) J_m(k_{r,mn}^I r) e^{im\theta} \right]. \quad (3.38)$$

For the perforated plate shown in Figure 3.1, each cylindrical orifice's sound field can be expressed analytically by Equation 3.33. The oscillating mass inside orifices with velocity amplitude \hat{u}_0 is imposed as the boundary condition on the cross-section of the hole (A_h) as follows:

$$\hat{u}_{\text{hole}} = \hat{u}_0 \text{ at } z = -L_p \quad (3.39)$$

Substitution of Equation 3.38 into Equation 3.39 gives for each orifice

$$Ai_{00}e^{ikL_p} - Bi_{00}e^{-ikL_p} = \rho c \hat{u}_0 \quad (3.40)$$

and

$$Ai_{mn}e^{-ik_{z,mn}^I L_p} - Bi_{mn}e^{ik_{z,mn}^I L_p} = 0. \quad (3.41)$$

At the cavity end-plate, the rigid-wall boundary condition gives

$$\hat{u}_{\text{cavity}} = 0 \text{ at } z = L_c \quad (3.42)$$

and the substitution of Equation 3.37 into Equation 3.42 yields

$$D_{00} = C_{00}e^{-2ikL_c} \quad (3.43)$$

and

$$D_{mn} = C_{mn} e^{2ik_{z,mn}^I L_c} . \quad (3.44)$$

At the area jump between the orifice and the cavity, continuity for pressure requires

$$\hat{p}_{\text{hole}} = \hat{p}_{\text{cavity}} \quad \text{at } z = 0 , \text{ on } A_h \quad (3.45)$$

and for the velocity

$$\hat{u}_{\text{hole}} = \hat{u}_{\text{cavity}} \quad \text{at } z = 0 , \text{ on } A_h \quad (3.46)$$

and

$$\hat{u}_{\text{hole}} = 0 \quad \text{at } z = 0 , \text{ on } (A_p - A_h) . \quad (3.47)$$

Equation 3.45 implies that pressure inside the orifice at each radial and circumferential coordinate on the orifice cross-section A_h on the interface plane $z = 0$ is equal to the pressure inside the cavity on the interface plane $z = 0$. This does not imply that all the orifices should have the same pressure on the interface $z = 0$. Similarly, Equation 3.46 implies that velocity inside the orifice at each radial and circumferential coordinate on the orifice cross-section A_h on the interface plane $z = 0$ is equal to the velocity inside the cavity on the interface plane $z = 0$. Equation 3.46 relates the acoustic velocity inside the cavity and the orifices via the open area ratio (porosity). Equation 3.47 implies that the acoustic velocity is zero on the plate surface (A_p) between the holes ($A_p - A_h$).

To form a system of independent equations for calculating the coefficients of the amplitude, Equations 3.45, 3.46, and 3.47 are coupled with the Fourier-Bessel functions orthogonality for the velocity and pressure conditions [71]. The details of forming a matrix, including the description of boundary conditions, are presented in Appendix A.

Following the procedure shown in Appendix A, by solving the set of equations for a finite number of higher-order modes, the pressure amplitudes for waves Ai_{mn} , Bi_{mn} , and C_{mn} can be obtained. Because of the diminishing effect of the higher-order modes (radial and circumferential) on the solution [71, 72], m and n can be truncated, and for the geometries and frequencies studied here, $N = m = n = 5$ were found to be sufficient [71, 72]. After obtaining the pressure amplitudes for waves Ai_{mn} , Bi_{mn} , and C_{mn} , the normalized end-correction for each orifice can be obtained from [71]

$$\delta_i = \frac{\hat{p}_{00}^I - \hat{p}_{00}^{II}}{i\rho\omega\hat{u}_{00}^I(\pi \cdot r_0^2)^{1/2}} = \frac{(Ai_{00} + Bi_{00}) - C_{00}(1 + e^{-2ikL_c})}{ik(Ai_{00} - Bi_{00})(\pi \cdot r_0^2)^{1/2}}. \quad (3.48)$$

Subscripts 00 represent the fundamental mode (0,0). This non-dimensional end-correction includes the acoustic radiation effect on one side of the orifice. The end-correction in Equation 3.48 is normalized by the square root of the orifice area $\sqrt{\pi r_0^2}$. The procedure of obtaining Equation 3.48 is briefly described in Appendix A. The normalized end-correction (δ_i) is calculated for each orifice separately. The average value of the normalized end-correction of all orifices in the plate is considered as the representative value of the normalized end-correction of the orifices in the perforated plate

$$\delta = \frac{1}{i} \sum_{n=1}^i \delta_i, \quad (3.49)$$

where i stands for the number of orifices in the plate and δ_i is the normalized end-correction of each orifice. The relation between the end-correction (l') (presented in Chapter 2) and the normalized end-correction (δ_i) can be written as

$$l' = \delta \sqrt{\pi r_0^2}. \quad (3.50)$$

To investigate the hole-to-hole interaction effect, several perforated plates with three different patterns of orifices (as shown in Figure 3.2) are considered in this thesis, and the end-correction is calculated.

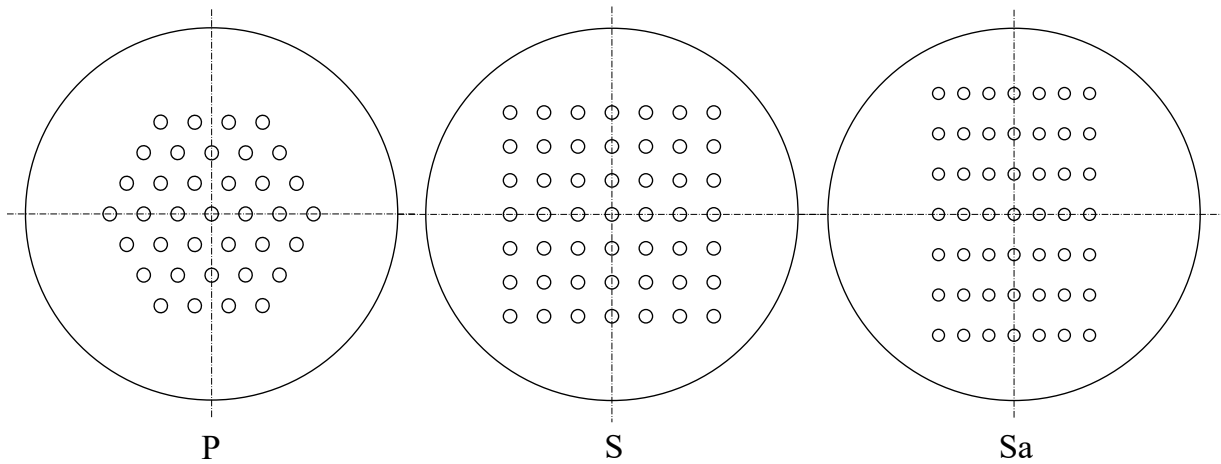


Figure 3.2: Schematic view of the studied orifice patterns (P, S, and Sa denote triangular, square, and rectangular patterns, respectively).

In this thesis, several orifice radii and spacing were studied numerically for the triangular, square, and rectangular patterns in the ranges given in Table 3.1. The diameter of perforated plates is 0.092 m , and the orifices have a circular shape.

Table 3.1: Geometrical parameters of the cases investigated numerically.

Pattern	Orifice radius [mm]	Center-to-center distance [mm]	Number of cases
P	0.25-6.25	0.75-12.75	147
S	0.15-4.65	0.99-10.56	91
Sa	0.4-2.65	0.9-13	44

4 Numerical Analysis (FEM)

The three-dimensional analytical approach presented in Chapter 3 leads to the pressure and velocity distributions throughout the domain. By including more higher-order modes (theoretically infinite number of higher-order modes) in the calculation, the pressure and velocity distributions become more accurate. In this chapter, the pressure and velocity distributions are obtained using Finite Element Method (FEM). Therefore, this chapter presents the FEM approach as an alternative for the three-dimensional analytical approach to obtain the pressure and velocity distributions, and the normalized end-correction using FEM and three-dimensional analytical approach will be compared.

This chapter starts with the description of the numerical setup and the simulation procedure, followed by the analysis of the numerical results. Firstly, a two-hole configuration is considered, because the only applicable end-correction model in the literature (proposed by Ingard [1]) is only valid for two-hole configurations, and current thesis aims to compare the results with Ingard's findings. After comparing the results of three-dimensional analytical approach and the FEM with Ingard's model for the two-hole configuration, a multi-orifice perforated plate will be studied and compared to Ingard's model. The normalized end-correction is obtained using FEM for a multitude of perforated plates. Finally, the normalized end-correction is used to obtain a mathematical function using regression analysis and machine learning algorithms.

4.1 Numerical Setup

To investigate¹ the propagation of the acoustic waves through small orifices, a three-dimensional, numerical solution in frequency space is obtained using FEM for the wave propagation described by the Helmholtz equation. Under the assumption of linear acoustics, the propagation of an acoustic plane wave in fluids at quiescent background conditions, excluding viscous and thermal losses, can be analyzed by solving the Helmholtz equation. Therefore, the Helmholtz equation in frequency space is solved in the computational domain shown in Figure 4.1, similar to the impedance tube used in experiments (presented in Chapter 5) based on a stabilized FEM approach. A MUMPS (Multifrontal Massively Parallel Sparse) direct solver is used to solve the discrete variational finite element formulation of the Helmholtz equation in frequency space. The computations are performed on an unstructured grid consisting of quadratic tetrahedral elements². The excitation is applied at the inlet by the Normal Acceleration boundary condition and at all the remaining boundaries, non-viscous wall-boundary conditions $\hat{u} \cdot \hat{n} = 0$ are imposed.

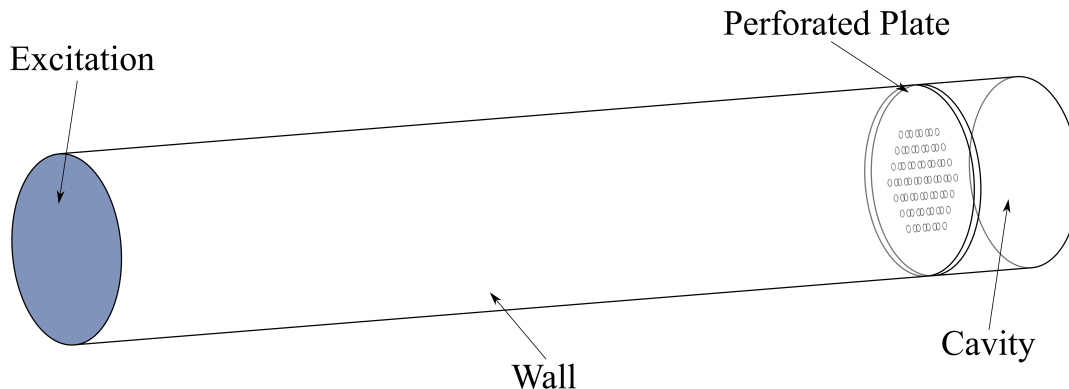


Figure 4.1: Schematic view of the domain investigated numerically.

The perforated plates, shown in Figure 3.2 with parameters in the ranges specified in Table 3.1 are investigated. The Multi-Microphone Method (MMM) [73] is used for wave decomposition (presented in Chapter 5). This finally delivers

¹The content of this chapter is partially published in the paper GT2021-58535 - *Proceedings of ASME Turbo Expo 2021* [2]

²The commercial software COMSOL Multiphysics is used.

the specific acoustic impedance of the resonator which is given by [25, 74]

$$Z = \rho c \frac{(1 + R)}{(1 - R)}. \quad (4.1)$$

As mentioned in Chapter 2, impedance is a complex quantity and has real and imaginary terms. To facilitate the physical interpretation of the impedance, the acoustic boundary condition can be modeled as a mass-spring-damper system. The sound wave applies unsteady force on the mass due to the oscillating pressure. Following the mechanical interpretation of the acoustic impedance, the real part of the impedance represents the resistive damper element and describes acoustic absorption or transmission at the boundary. The imaginary part stands for the reactive spring or mass element that does not dissipate sound, but introduces a phase shift between the pressure and velocity at the boundary [25].

The maximum acoustic absorption of the resonator happens at the frequency where the acoustic reflection coefficient is equal to zero. In other words, when the incident wave is transmitted or fully absorbed at the boundary, the acoustic reflection coefficient (R) tends to zero. Since the FEM used in this chapter excludes the viscosity and bias flow effects, the magnitude of the reflection coefficient remains constant and equal to unity over the studied frequency range, because there is no damping effect. Therefore, the above-mentioned criterion for identifying the frequency, at which the absorption is maximum, cannot be used because the reflection coefficient does not show any minimum. The acoustic absorption coefficient is given by [51, 74]

$$\alpha = 1 - |R|^2 = \frac{4\theta}{(1 + \theta)^2 + \chi^2}, \quad (4.2)$$

where θ and χ stand for the normalized specific acoustic resistance and reactance, respectively. Equation 4.2 shows that the maximum absorption coefficient happens when $\theta \rightarrow 1$ and $\chi \rightarrow 0$. The optimum absorption takes place at the frequency where acoustic reactance is zero, which also coincides with the resonance frequency of the perforated plate backed by a cavity [51, 74]. In

this chapter, the acoustic reactance is equal to zero ($\chi = 0$), is used as the criterion to identify the resonance frequency of the perforated plate backed by a cavity. After obtaining the resonance frequency from FEM, this frequency is used to calculate the acoustic end-correction using the Helmholtz resonator's resonance frequency formula given by

$$f_{res} = \frac{c}{2\pi} \left(\frac{A}{VL'_p} \right)^{1/2}, \quad (4.3)$$

with A , V , and L'_p being the open area of orifices, cavity volume, and effective neck length ($L'_p = L_p + 2l'$), respectively. All parameters in Equation 4.3 are defined except the effective neck length (l'). After obtaining the effective neck length, the acoustic end-correction can be calculated using

$$l' = \frac{L'_p - L_p}{2}. \quad (4.4)$$

The acoustic end-correction for 282 perforated plates in the ranges listed in Table 3.1, which are numerically investigated, is acquired from Equation 4.3. The end-correction for each plate is divided by two to account only for one side of the orifice and then normalized by the square root of the hole's area $\sqrt{\pi r_0^2}$ to obtain the normalized end-correction (δ). The normalized end-correction obtained using this method is the average value of the normalized end-correction values of the orifices in the perforated plate.

4.2 Two and Multiple Holes

This section presents the effect of acoustic radiation of neighboring orifices in a multi-orifice pattern on each other. Before investigating this effect for a multi-orifice pattern, the end-correction for a two-hole pattern (shown in Figure 4.2 as A1) is obtained using the three-dimensional analytical method presented in Chapter 3. Results are presented in Figure 4.3. Squares represent the end-correction of each hole in a two-hole pattern. An increase in

end-correction is observed by increasing the number of higher-order terms (m and n), which means considering more higher-order modes in the process of calculating the normalized end-correction (described in Chapter 3). Since the higher-order modes have a vanishing effect on the final solution, calculation of end-correction up to $N = m = n = 5$ is suggested to avoid the excessive computational cost associated with the increased number of higher-order modes [71]. It is worth mentioning that depending on the configuration, it might be necessary to calculate for N higher than 5. It should be mentioned that in this pattern, there are two orifices, and increasing the number of holes will require even more computational resources.

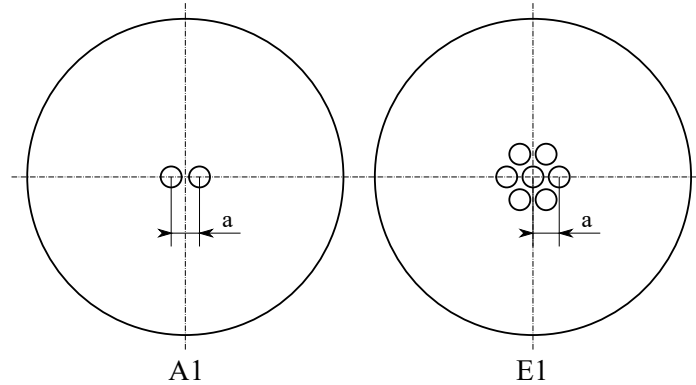


Figure 4.2: Schematic view of the plates with two-holes (A1) and multi-orifice (E1).

As mentioned earlier in Chapter 3, only the formulation proposed by Ingard (described by Equations 2.25 and 2.26) is able to address the hole-to-hole interaction effect in the two-holes pattern. The end-correction calculated by Ingard's formulation is presented by the blue dashed-line in Figure 4.3. The three-dimensional analytical method shows marginal improvements compared to Ingard's formulation, which can be associated with Ingard's low frequency and infinite tube assumptions in his model [1]. Furthermore, the end-correction of the two-hole pattern in Figure 4.2 acquired using FEM is shown in Figure 4.3. The FEM solving the Helmholtz Equation (presented in Equation 3.28) results in the solution of the acoustic pressure inside the domain (presented by Equations 3.29 and 3.33). This solution of the acoustic pressure inside the domain can be obtained similarly by solving the equations

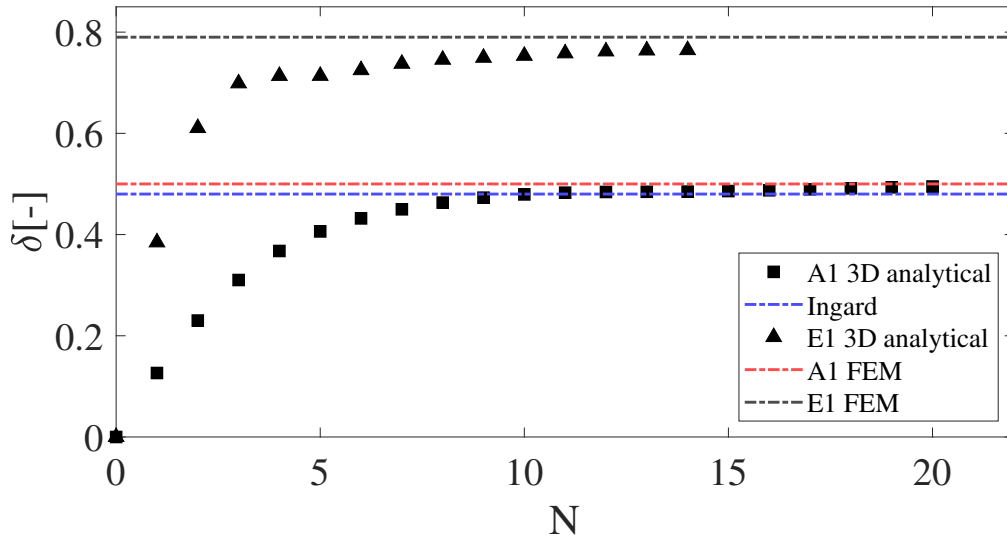


Figure 4.3: Comparison of the normalized end-correction obtained for two-holes (*A1*) and multi-orifice (*E1*) configurations by increasing the number of higher-order modes ($N = m = n = 5$) included in the three-dimensional analytical method [2].

proposed by the three-dimensional analytical method for an infinite number of higher-order modes. The results shown in Figure 4.3 can be interpreted as solving the equations of the three-dimensional analytical method for a theoretically infinite number of higher-order modes results in a similar acoustic pressure distribution inside the domain (Equations 3.29 and 3.33) to the FEM solution. Therefore, the FEM results are considered as the reference throughout this chapter.

Furthermore, the average end-correction in a multi-orifice pattern shown in Figure 4.2 as *E1* calculated by the three-dimensional method is depicted in Figure 4.3 by triangles. Similar to the two-holes pattern, the end-correction increases for the first five modes and then converges quickly. As expected, Ingard's formulation for the two-holes pattern cannot predict the increased end-correction for the multi-orifice pattern. The reason is that Ingard considered only two orifices on a plate. Ingard's formulation was a significant progress toward the investigation of the hole-to-hole interaction effect. However, his method is limited to two orifices and cannot be applied to configu-

rations with multiple orifices. The end-correction of the E1 pattern acquired using FEM is shown in Figure 4.3 by black dashed-line. Similar to the two-holes pattern, the end-correction obtained from FEM is greater than the end-correction obtained from the three-dimensional analytical method. By solving the equations of the three-dimensional method for higher number of higher-order modes, the value of end-correction becomes closer to the FEM result. This observation again confirms that if the equations of the three-dimensional analytical method are solved for infinite number of higher-order modes, the resulting value of the end-correction will converge to the FEM result.

In Figures 4.4 and 4.5, the normalized specific acoustic reactance of several plates obtained using FEM are presented. Figure 4.4 shows the results for the perforated plates with the orifice radius of $r_0 = 1.25 \text{ mm}$ and various center-to-center spacing. Similarly, Figure 4.5 shows the results for the perforated plates with the orifice radius of $r_0 = 1.75 \text{ mm}$ and various center-to-center spacing.

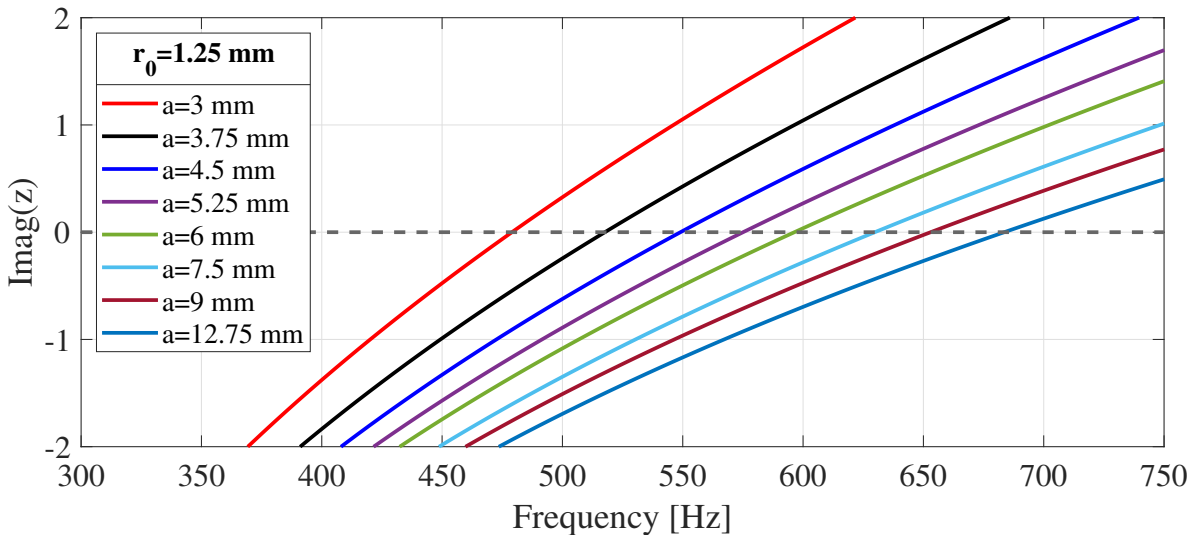


Figure 4.4: Normalized specific acoustic reactance of perforated plates with the orifice radius $r_0 = 1.25 \text{ mm}$ and various center-to-center spacing obtained from FEM [2].

All perforated plates in the ranges listed in Table 3.1 demonstrate similar behavior. As shown in Figures 4.4 and 4.5, acoustic reactance curves shift to

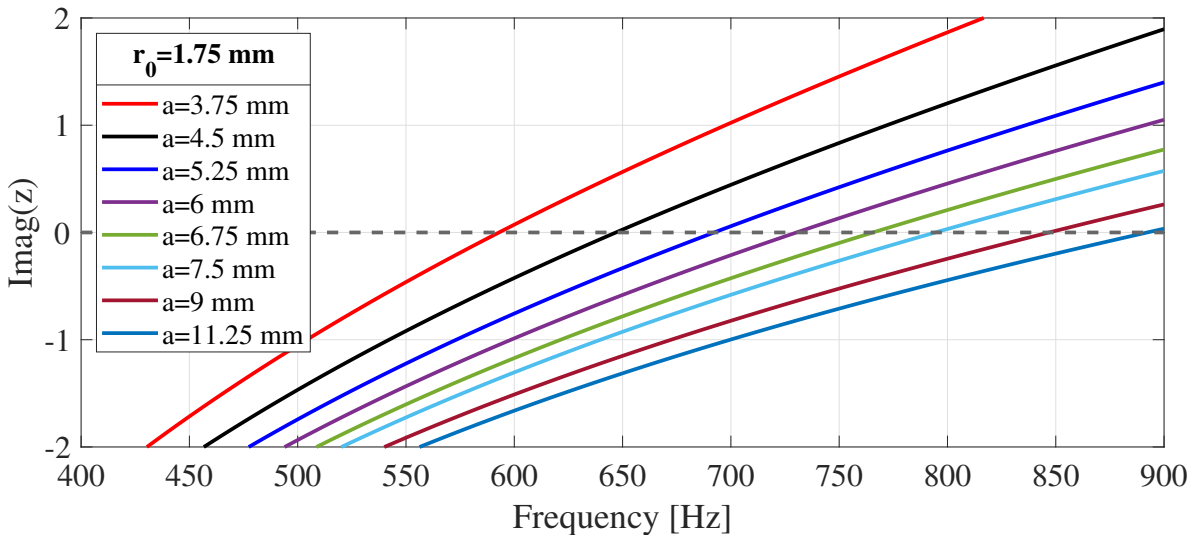


Figure 4.5: Normalized specific acoustic reactance of perforated plates with the orifice radius $r_0 = 1.75 \text{ mm}$ and various center-to-center spacing obtained from FEM [2].

lower frequencies as the distance between orifices decreases. By considering the $\text{Imag}(z)=0$ as the criterion to identify the resonance frequency (discussed earlier in this chapter following Equation 4.2), the shift in acoustic reactance curves leads to a shift in resonance frequency. The resonance frequency for each curve, which represents a perforated plate, is the frequency at which the acoustic reactance ($\text{Imag}(z)$) is zero. This decrease in resonance frequency implies that the end-correction increases by decreasing the orifices' distance, according to Equation 4.3. However, this is contrary to the findings of Fok [41] and Ingard [1], while the same behavior is observed by Tayong [49] and Wang et al. [51]. This difference results from the fact that the findings of Fok [41] and Ingard [1] are obtained by assuming a single orifice in the center of the tube, and their findings are inappropriately used by other authors and applied to the multi-orifice configurations, while, these findings are only valid for the configurations with a single orifice such as Helmholtz Resonators.

The results shown in Figures 4.4 and 4.5 represent the overall trend of resonance frequency shift by varying the holes' center-to-center spacing. To evaluate effect of orifice spacing on the acoustic field inside the domain, the acous-

tic velocity magnitude in the proximity of orifices from FEM is obtained for two plates from P pattern (shown in Figure 3.2) with the same orifice radius ($r_0 = 0.8 \text{ mm}$) and different orifice spacing. The results are shown in Figures 4.6 and 4.7.

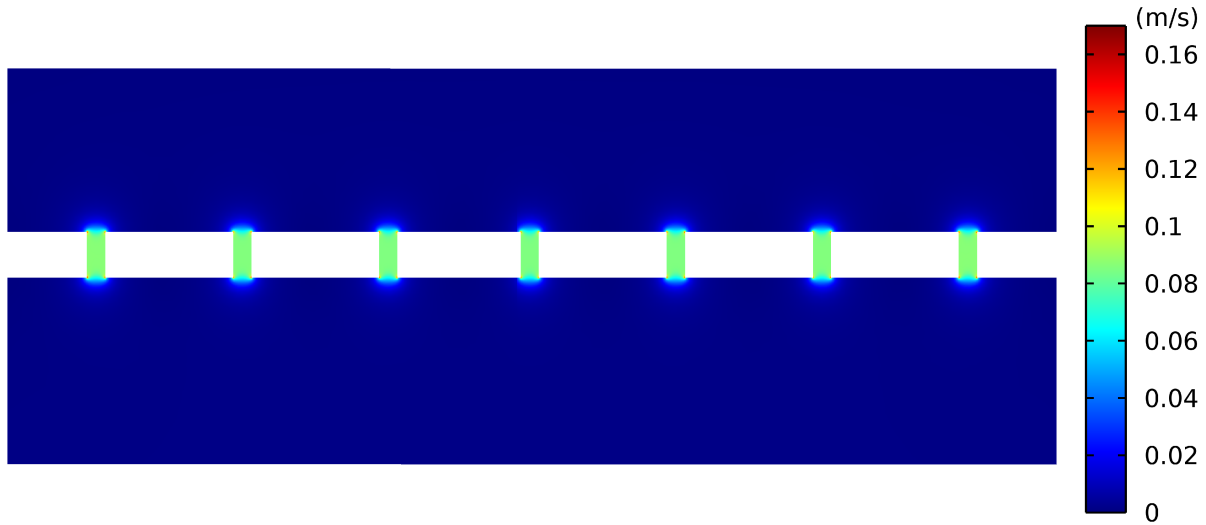


Figure 4.6: Acoustic velocity magnitude contour in the vicinity of orifices with radius $r_0 = 0.8 \text{ mm}$ and orifice spacing $a = 12.75 \text{ mm}$ [2].

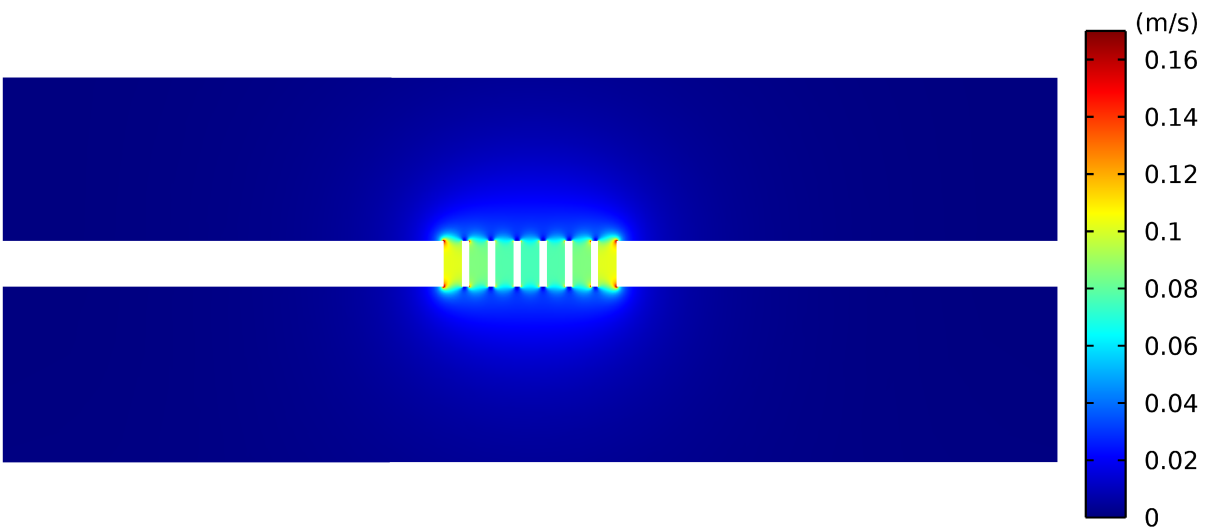


Figure 4.7: Acoustic velocity magnitude contour in the vicinity of orifices with radius $r_0 = 0.8 \text{ mm}$ and orifice spacing $a = 2.25 \text{ mm}$ [2].

As shown in Figure 4.6, when the holes are located far from each other, the oscillating mass of each hole is not significantly affected by the adjacent orifices. In contrast, the oscillating mass of orifices is strongly influenced by the neighboring holes when the orifices are tightly distributed, as shown in Figure 4.7. The acoustic velocity profile is affected farther downstream, and the region with oscillating mass extends on both sides of the orifice (Figure 4.7). Wang et al. [51] observed similar behavior. They described that the acoustic velocity does not vanish so rapidly in the vicinity of the area discontinuity when holes are closely distributed due to the combined momentum of the interacting jet flows from neighboring orifices. Therefore, following these observations and according to the formulation proposed by Ingard (described by Equation 2.26), the end-correction due to acoustic radiation for a pattern of orifices can be considered as a function of the orifices' radius and spacing. Wang et al. [51] considered this phenomenon as superposition of two radiation effects: the radiation of a single orifice and the radiation associated with the perforation region.

To evaluate how the orifices' radius and spacing affect the end-correction, the normalized end-correction for all perforated plate in the ranges listed in Table 3.1 are acquired from the FEM results using the resonance frequency (Equation 4.3). The normalized end-correction for P and S patterns are presented in Figures 4.8 and 4.9, respectively.

The results show that increasing the distance of orifices decreases the normalized end-correction and vice versa. In addition, decreasing the orifice radius increases the end-correction, similar to the findings available in the literature [1, 35, 48, 49, 51]. The normalized end-correction for the square pattern S presented in Figure 4.9 shows similar behavior to the P pattern.

After having obtained the normalized end-correction (δ) for different orifice patterns with various geometrical parameters, it is required to find mathematical functions representing the δ of the considered patterns. These functions simplify the calculation of the normalized end-correction for those configurations that are not included in this study and acts as an interpolation function. The procedure of extracting such mathematical functions is described in the following section. Two independent functions are proposed for triangular pat-

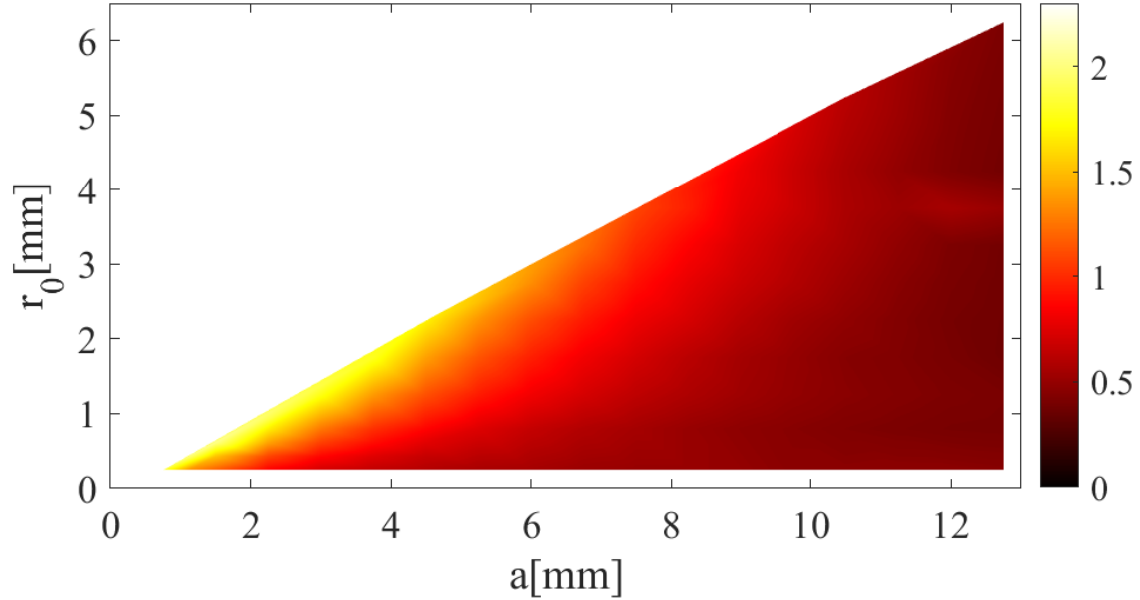


Figure 4.8: The contour of interpolated normalized end-correction (δ) of perforated plates with triangular pattern (P) obtained from FEM [2].

tern (δ_p) and square and rectangular patterns ($\delta_{S,sa}$).

4.3 Machine Learning

This section aims to obtain Machine Learning (ML) models and mathematical correlations that represent the normalized end-correction as a function of geometrical parameters. As a result, the correlations obtained from regression analysis are compared to the models obtained using machine learning algorithms.

This section begins with a brief introduction of several machine learning algorithms that are used for interpolation. Following the introduction, the training data set is proposed, followed by the procedure of obtaining data-driven models. The representative mathematical correlations obtained using regression analysis are described. Finally, the performance analysis of the obtained models is presented.

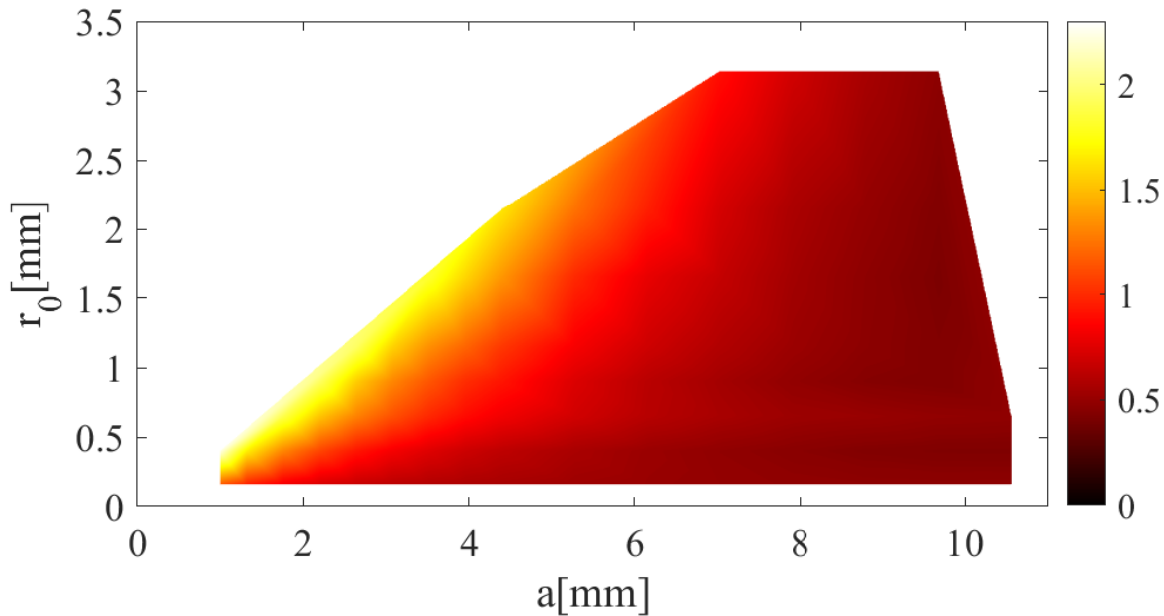


Figure 4.9: The contour of interpolated normalized end-correction (δ) of perforated plates with square pattern (S) obtained from FEM [2].

Machine Learning Algorithms

Gaussian Processes

Gaussian Processes describe probability distributions over a family of functions and use Bayes' rule to update the distribution of functions by observing training data points. In other words, Gaussian Processes generate a Gaussian posterior using a prior assumption and the training data points. Every realization of a Gaussian Processes is not a set of numerical values but an entire function. Indeed, Gaussian Processes (GP) model the underlying function and not its parameters. Gaussian Processes (GP) are non-parametric models. The non-parametric model does not imply that there are no parameters. In GP, the parameters are the function itself. The non-parametric model in this context means infinite number of functions. A Gaussian Process (GP) is defined by its mean function $m(x)$ and its covariance function $k(x, x')$.

The mean function $m(x)$ specifies the form of the prior mean function of the

Gaussian Process regression model, and describes the expected value of the distribution. There are different types of mean functions such as Zero, Constant, and Linear. The form of mean function is more influential in the extrapolation, while for the interpolation, it may not affect the outcome significantly. In the current study, the Zero mean function is selected because the data points are selected to be located on the boundary of the domain. Therefore, there is no need to extrapolate the results. The data set domain boundary represents values of the geometrical parameters. In other words, outside of the selected domain boundary defined by the geometrical parameters, the configurations are not geometrically feasible (e.g., orifices locate outside of the plate or the orifices become inasmuch close so that they intersect and no longer represent individual circular orifices). The procedure for selecting the training data set is presented in the following section.

It is expected that the data points with similar input values x , have similar response values y . In Gaussian Processes, the covariance function describes the variance in the response values y [75]. In other words, it determines how the response at one point x is affected by responses at other points x' . The covariance function $k(x, x')$ can be characterized by several kernel functions. The kernel parameters that can be used for parameterization of the covariance function are based on the standard deviation and the characteristic length scale. The characteristic length scale describes the farthest distance between two priors x and x' for the posteriors to become uncorrelated. Training of a Gaussian Process implies the selection of a covariance function and its kernel parameters. GPs are discussed further in detail in [75].

Support Vector Machines

In machine learning, Support Vector Machines (SVMs) are supervised learning models widely used for classification and regression (known as Support Vector Regression) problems. Support Vector Machines (SVMs) are introduced by Vladimir Vapnik [76]. In general, the objective in linear regression models is to minimize the sum of squared errors (e.g., Ordinary Least Squares or OLS). However, the Support Vector Regression (SVR) aims to reduce the error to a

given magnitude and is not concerned about reducing the error of points that fall within this range. In other words, using SVR gives flexibility in defining the extent to which the error is acceptable in the training of the model. Indeed, the SVM uses the “kernel trick” to transform the input data in a nonlinear manner to a higher dimensional space where the data becomes linearly separable, and hence easier to model. Then an appropriate fit to the data set will be found.

Since the Support Vector Regression (SVR) depends on the kernel functions, it is classified as a non-parametric model. The SVR used in this study is linear epsilon-insensitive SVM regression (ϵ -SVM) that ignores prediction errors less than the defined value ϵ . In other words, the objective in this method is to fit a function that deviates from the observed response no greater than ϵ for each prior (training point). The data points with error values greater than ϵ are called the support vectors. In ϵ -SVM, only predictions that have the error values larger than ϵ (support vectors) are used during model training. This helps the model training to improve predictions in regions with poor performance and results in a more generalized model [77]. This method has three hyper-parameters: ϵ , an error penalty (or box constraint C), and the kernel length scale. The role of the box constraint is to control the penalty applied on the observations with an error value greater than ϵ . Setting a larger error penalty results in a more flexible model, while a smaller value leads to a rigid model which is less sensitive to over-fitting. The kernel length scale governs the scale over which the predictor output changes significantly.

Interpolation

Splines are a piecewise interpolation method that considers a set of polynomials of degree w that are smoothly connected to adjoining data points [78]. At each point of the data set, two polynomials connect, and their corresponding first derivatives have the same value. In the case of higher order of polynomials, it is also required by the definition that all the derivatives up to the $(w-1)$ st are the same at the point. In this study, linear and cubic forms of interpolation are used. The linear spline is the most simple form of interpolation and represents a set of straight-line segments between each adjacent data points. The

cubic spline is the most widely used interpolation and improves the piecewise interpolation by matching the data values, slopes, and the concavity of each interpolating segment [79].

Training Data Set

To train data-driven models and perform regression analysis, a training data set is required. The training data set is composed of the normalized end-correction values obtained from FEM for all the configurations listed in Table 3.1 (the procedure for obtaining the normalized end-correction from FEM is described earlier in this Chapter). The data points representing the experimental configurations are excluded because these data points will be used to validate the numerical model with the experimental results. In addition, for testing the numerical model, a testing data set is generated randomly after training the models. The testing data set is generated after model training to ensure that the data points that are used for evaluating the performance of the model, are excluded from the training process. The number of testing data points is approximately 15% of the training data points.

Training data points are selected carefully to cover the whole region defined by the geometrical parameters. Therefore, extrapolation may become irrelevant, and training of the model implies interpolation. This choice of training data set helps avoid unreliable predictions associated with extrapolation, which are heavily influenced by implicit model assumptions, such as hyper-parameter tuning and influence of the mean function in the case of Gaussian Processes (GP). To clarify the idea behind the boundary of geometrical parameters, six perforated plates are shown in Figure 4.10. For these samples, the orifice radius is kept constant. If the orifices become so close to each other so that they intersect, then they no longer represent individual circular orifices (shown in Figure 4.10 top, for configurations P, S, and Sa). Similarly, if the distance between orifices increases so that the orifices are located on the periphery of the plate, they also do not represent circular orifices, although the distance between orifices in both situations is smaller than the plate radius (shown in Figure 4.10 bottom, for configurations P, S, and Sa). Therefore, lower and up-

per limits of the distance of orifice should be defined at each orifice radius and for each configuration, separately. These extreme cases will form the boundary of the geometrical parameters, beyond which the configurations are not geometrically feasible and not relevant. For the purpose of training, the extreme cases that are located on the boundary of the geometrical parameters are identified and included in the training data set to facilitate the model training by transforming the model training into an interpolation problem.

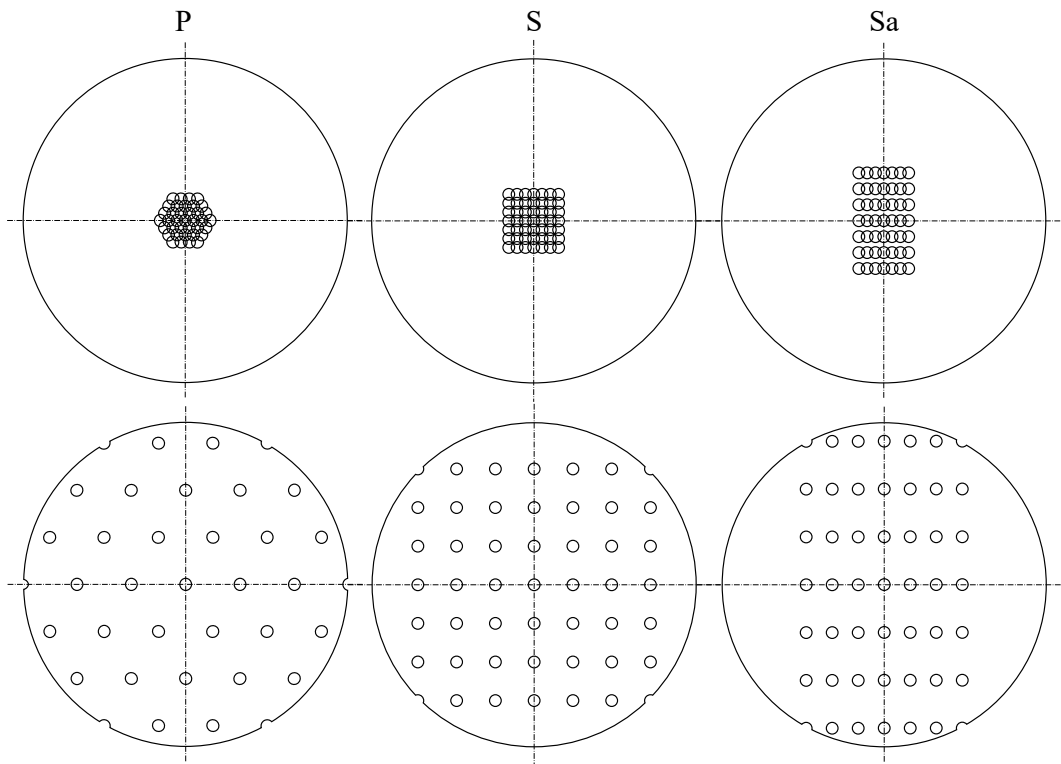


Figure 4.10: Perforated plates that are considered as the boundary of the geometrical parameters. The samples on the top represent the situation where orifices are too close to each other such that they intersect, and the bottom samples represent the situation where orifices are inasmuch far from each other such that they are located on the periphery of the plate.

In the current section, the training data set and the approach to obtain it are described for configuration P only, to avoid repetition of the same procedure for configurations S and Sa. The training data set for the P configura-

tion is presented in Figure 4.11. Circles represent the perforated plate samples, and the lines represent contour lines of the constant orifice radius. At a constant orifice radius, decreasing the orifice spacing (a) increases the hole-to-hole interaction end-correction (denoted here by δ as the normalized end-correction). When the orifice radius (r_0) is smaller, the maximum normalized end-correction is greater compared to the larger orifice radii. The normalized end-correction of the configurations with smaller orifice radius changes more significantly compared to the configurations with larger orifices, when center-to-center orifice spacing is decreased. In other words, the normalized end-correction of the configurations with smaller orifice radii are more sensitive to the center-to-center orifice spacing.

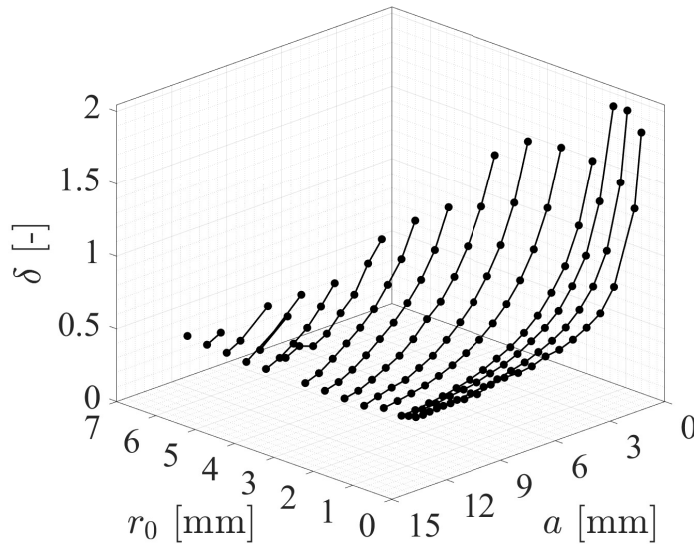


Figure 4.11: The training data set for the P configuration.

Normalized end-correction behavior depends on the orifice spacing and the radius. According to Equations 2.25 and 2.26, the end-correction for a single orifice is a function of radius ratio (r_0/R_c). To consider the effect of orifice spacing for different hole patterns, a circle with an equivalent area associated with the orifices on the plate is considered, and the ratio between the orifice radius and the equivalent circle radius (r_0/R_{eq}) is obtained. As shown in Figure 4.12, transforming the area associated with the orifices to an equivalent

circle may facilitate the modeling of the effect of orifice spacing for different orifice patterns.

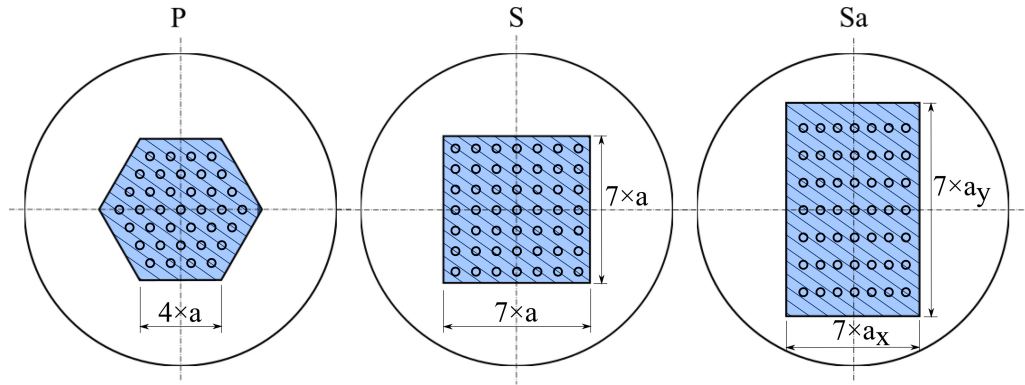


Figure 4.12: The area associated with the perforation region is shaded.

As shown in Figure 4.12, the area associated with the orifices is expanded by half of the center-to-center orifice spacing to include the effect of the outermost orifices in the plate. This associated area is considered to be equivalent to a circle whose radius is R_{eq} (equivalent circle radius).

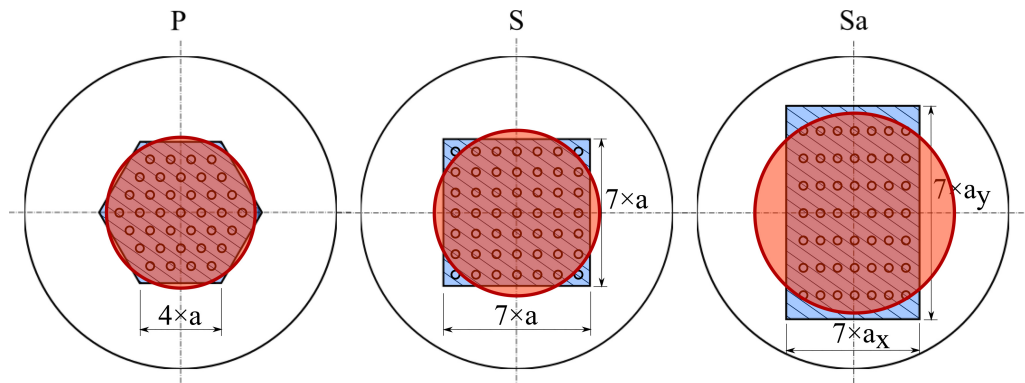


Figure 4.13: Representation of the equivalent circle and its radius.

The training data set with the transformed axes is shown in Figure 4.14 for P configuration. The connecting lines show less curvature, implying a relatively linear relationship between δ and the input variables.

Similarly, the training data set with the transformed axes is shown in Figure 4.15 for S and Sa configurations. The black circles represent the data points

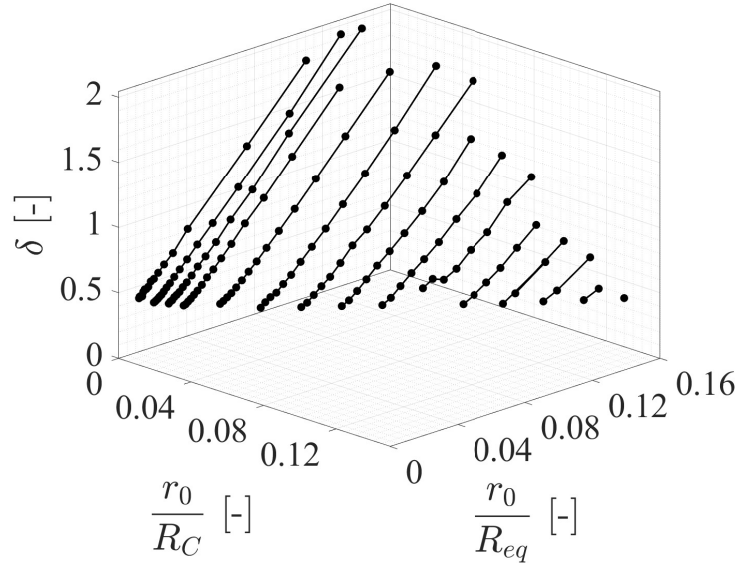


Figure 4.14: The training data set for the P configuration with the transformed axes.

of S configuration, while the red circles represent the data points of Sa configuration.

Model Training

To train Machine Learning (ML) models with the training data set, the Regression Learner toolbox of MATLAB[®] is used. Hyper-parameters optimization is used to find the model structure that gives the lowest error on the training data set. For example, to train a Gaussian Process (GP), all of the available combinations of the kernel and mean functions are used to obtain the most optimal combination of hyper-parameters.

For the purpose of model training, the training data set is used in such a way that r_0/R_c and r_0/R_{eq} are considered as input variables, and the normalized end-correction (δ) as model output. After training models, the output of each model, which is the normalized end-correction predicted by the model (referred to as predicted response), is compared with the normalized

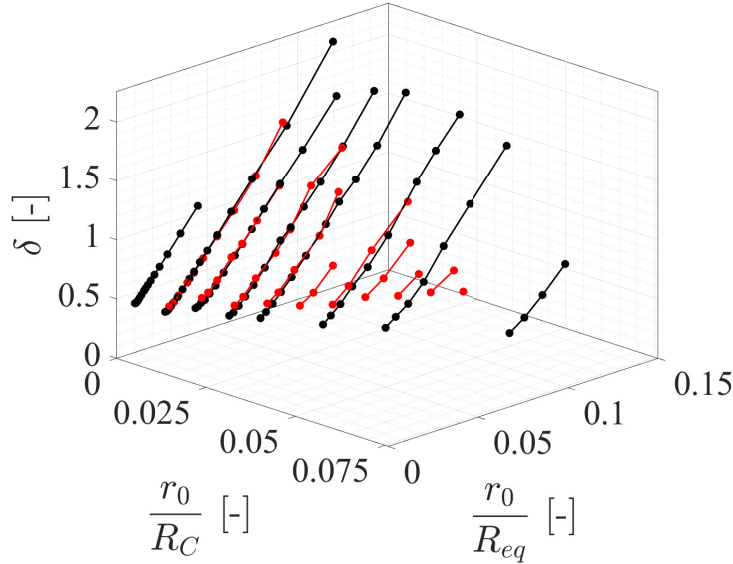


Figure 4.15: The training data sets for the S and Sa configurations with the transformed axes.

end-correction used for training (referred to as true response). Figures 4.16 and 4.17 show the predicted response and compare it with the true response for each training data point and trained model for P, S, and Sa configurations, respectively. Circles represent the data points, and the straight diagonal line stands for the perfect prediction. The closer the circles are to the perfect prediction line, the prediction of the model is closer to the normalized end-correction values used for training. In Figure 4.16, most of the data points are located on the perfect prediction line with relatively low scatter.

To present how close the normalized end-correction predicted by models are from the true response (the normalized end-correction which is obtained from FEM and used for the model training), residual for each data point is calculated by

$$Residual = \frac{\delta_{Predicted} - \delta_{True}}{\delta_{True}} \times 100, \quad (4.5)$$

where $\delta_{Predicted}$ and δ_{True} stand for the predicted normalized end-correction

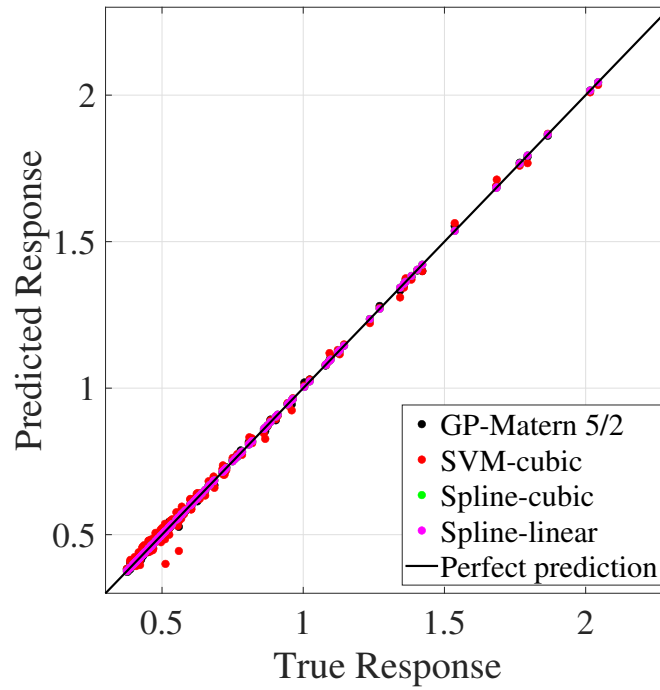


Figure 4.16: Predicted response versus true response for P configuration.

by models and the normalized end-correction obtained from FEM, respectively. The residuals for all data points and trained models for P configuration are shown in Figure 4.18. In Figure 4.18 similar to Figure 4.16, data points of GP and Spline (both cubic and linear) are in the proximity of the zero-residual line, while the data points of the SVM are more scattered.

To evaluate the performance of each machine learning model, the Normalized Root Mean Square Error (NRMSE) is used as the performance metrics. NRMSE indicates the normalized error of the model with respect to the data by evaluating how close the the model's prediction are to the normalized end-correction values obtained from FEM.

$$NRMSE = \frac{\sqrt{\frac{1}{n} \sum_1^n (\hat{y}_i - y_i)^2}}{\frac{1}{n} \sum_1^n y_i} \times 100. \quad (4.6)$$

In Equation 4.6, n stands for the number of data points used for the models

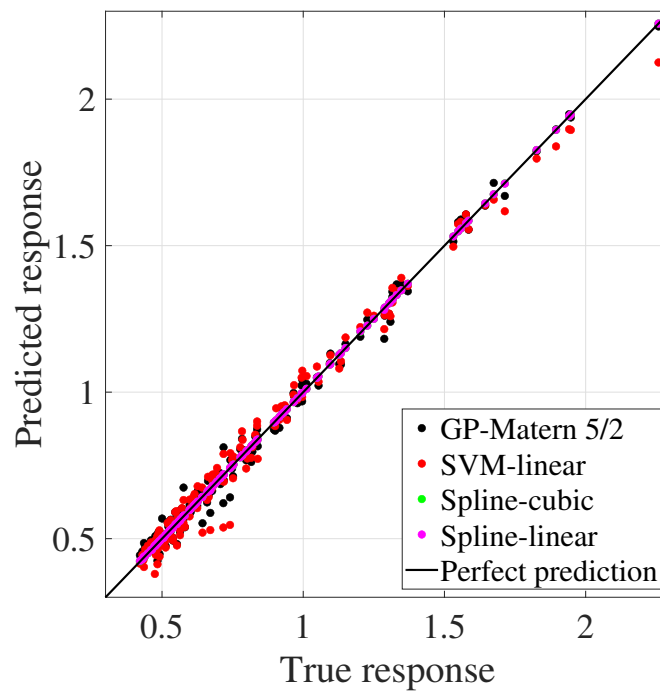


Figure 4.17: Predicted response versus true response for S and Sa configurations.

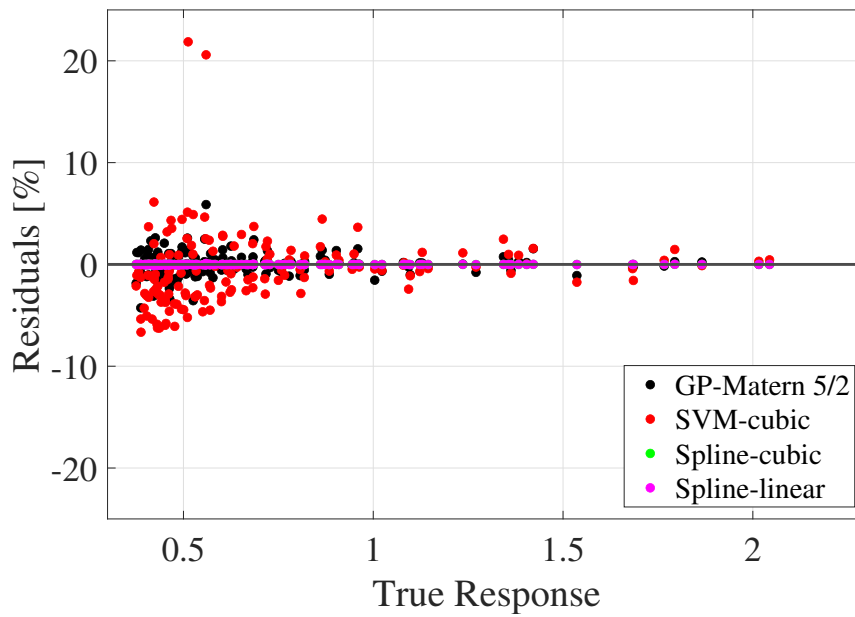


Figure 4.18: Data points' residual of trained models for P configuration.

training. As mentioned earlier, the normalized end-correction values obtained from FEM are used for the models training. $\hat{y}_1, \hat{y}_2, \dots, \hat{y}_n$ are predicted values of the normalized end-correction by models ($\delta_{Predicted}$), while y_1, y_2, \dots, y_n are the normalized end-correction values obtained from FEM and used for the models training (δ_{True}). NRMSE is a good measure of how accurately the model predicts the normalized end-correction. Lower values of NRMSE indicate a better fit of the model to the data. NRMSE values for the machine learning models trained for P configuration are presented in Table 4.1.

Table 4.1: NRMSE [%] values of the machine learning models trained for P configuration on the training data set.

GP	SVM	Spline cubic	Spline linear
1.0183	2.8956	0.0118	0.0173

Similarly, the NRMSE values for the machine learning models trained for S and Sa configurations are presented in Table 4.2.

Table 4.2: NRMSE [%] values of the machine learning models trained for S and Sa configurations on the training data set.

GP	SVM	Spline cubic	Spline linear
4.2127	5.6593	0.1073	0.1551

In addition to the models obtained from machine learning algorithms (GPs, SVM, and Splines), mathematical correlations for the normalized end-correction is obtained from the training data points using regression analysis. These mathematical correlations are obtained independent from the machine learning models. To obtain mathematical correlations, the numerical results shown in Figures 4.8 and 4.9 are used.

The behavior of the normalized end-correction depends on the orifice spacing and the radius. Therefore, the end-correction model may have the following

shape:

$$\delta = 0.48 \left(1 + C_1 \frac{r_0}{R_c} + C_2 \frac{r_0}{R_{eq}} \right), \quad (4.7)$$

where C_1 and C_2 are coefficients. By including $C_1 \frac{r_0}{R_c}$, the model considers the end-correction of one orifice which its radius can be varied. The term $C_2 \frac{r_0}{R_{eq}}$ accounts for the variation in the orifice spacing in such a way that decreasing orifice spacing will reduce the equivalent circle radius R_{eq} . The factor of 0.48 stands for the maximum value of the normalized end-correction of a single orifice in the plate, which is introduced by Ingard [1]. The effect of hole-to-hole interaction is considered as an additional effect on the normalized end-correction. Therefore, Equation 4.7 includes superimposed effects of the end-correction of a single orifice in the plate and the hole-to-hole interaction. The coefficients C_1 and C_2 are obtained by regression analysis for the triangular pattern (P) as

$$\delta_P = 0.48 \left(1 - 34 \frac{r_0}{R_c} + 26.56 \frac{r_0}{R_{eq}} \right). \quad (4.8)$$

Similarly, for square and rectangular patterns (S and Sa) as

$$\delta_{S,Sa} = 0.48 \left(1 - 50.41 \frac{r_0}{R_c} + 38.19 \frac{r_0}{R_{eq}} \right). \quad (4.9)$$

The difference in the coefficients results from the difference in the arrangement of orifices in the studied patterns. For instance, in P pattern (triangular), each orifice is surrounded by six orifices, while in S and Sa patterns (square and rectangular), each orifice is surrounded by eight orifices.

The mathematical correlations obtained using regression (presented in Equations 4.8 and 4.9) are obtained independent of Machine Learning (ML) algorithms. The obtained correlations will be compared with the trained ML models in the following section.

Performance Analysis

This section presents the performance analysis of the trained machine learning models and the obtained mathematical correlations (presented in Equations 4.8 and 4.9). The random test data points, which are used to evaluate the performance of each model in predicting the normalized end-correction, are equivalent to approximately 15% of the training data points.

The normalized end-correction of the test data points is obtained using FEM, after training the machine learning models, to ensure that the models' training is not influenced by the test data set. These data points are used to assess the performance of the trained models using ML and the mathematical correlations obtained using regression (presented in Equations 4.8 and 4.9).

The NRMSE values of the machine learning models trained for P configuration are presented in Table 4.3 to evaluate the performance of each model in predicting the test data points. The NRMSE values of the ML models have the same order of the magnitude and less than the NRMSE of the mathematical correlation δ_P .

Table 4.3: NRMSE [%] values of the machine learning models trained for P configuration applied to the test data set.

GP	SVM	Spline cubic	Spline linear	δ_P
1.2280	1.9836	1.1715	1.1718	7.1723

Similar to the configuration P, the test data points are used to evaluate the performance of the trained machine learning models for the configurations S and Sa. The NRMSE values are presented in Table 4.4 and show an increase compared to the NRMSE values obtained for P configuration, except the $\delta_{S,Sa}$ which has a lower NRMSE.

In summary, it can be concluded that the mathematical correlations obtained by regression (presented in Equations 4.8 and 4.9) have relatively the same level of accuracy compared to the ML models, according to the NRMSE values. A main drawback of the ML models is that these models cannot be eas-

Table 4.4: NRMSE [%] values of the machine learning models trained for S and Sa configurations applied to the test data set.

GP	SVM	Spline cubic	Spline linear	$\delta_{S,Sa}$
3.2976	4.6558	3.4935	3.4905	4.3894

ily transferred to users, while the mathematical correlations can be used as presented in Equations 4.8 and 4.9. The current section aimed to compare the performance of mathematical correlations obtained by regression with the ML models. Now that is shown that the mathematical correlations have relatively the same level of accuracy in comparison with the ML models, the mathematical correlations (Equation 4.8 and 4.9) will be used for further comparison with the experimental results in Chapter 6.

5 Experimental Setup and Measurement Techniques

This chapter¹ aims to describe the measurement technique used in this work, followed by the description of the test setup and the investigated perforated plate configurations.

5.1 Plane Wave Decomposition

In acoustic measurements in the impedance tube, only plane waves are considered. The acoustic pressure recorded by a microphone is a superposition of two waves propagating in opposite directions. This superposition is mathematically expressed by Equation 3.27 and is presented here again by

$$\hat{p}(z) = \hat{p}^+ e^{-ik^+ z} + \hat{p}^- e^{ik^- z}. \quad (5.1)$$

By knowing the $\hat{p}(z)$ from measurements at each axial location z_1, z_2, \dots, z_m (as illustrated in Figure 5.1), the complex amplitudes \hat{p}^+ and \hat{p}^- can be identified by using the plane wave decomposition. Therefore, a system of equations can be constructed as follows,

$$\begin{aligned} \hat{p}(z_1) &= \hat{p}^+ e^{-ik^+ z_1} + \hat{p}^- e^{ik^- z_1} \\ \hat{p}(z_2) &= \hat{p}^+ e^{-ik^+ z_2} + \hat{p}^- e^{ik^- z_2} \\ &\vdots \\ \hat{p}(z_m) &= \hat{p}^+ e^{-ik^+ z_m} + \hat{p}^- e^{ik^- z_m} \end{aligned} \quad (5.2)$$

¹The content of this chapter is partially published in the paper GT2021-58535 - *Proceedings of ASME Turbo Expo 2021* [2]

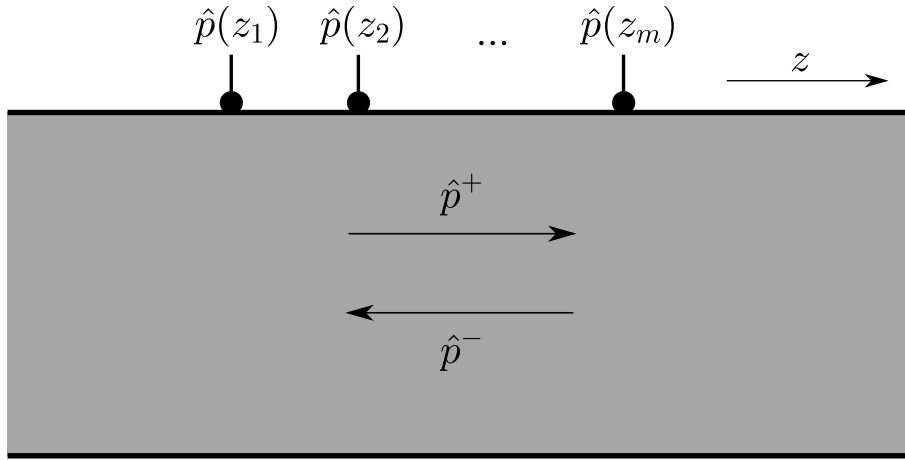


Figure 5.1: Illustration of the two waves propagating in the opposite direction.

Rewriting the system of equations in the form of a matrix yields

$$\underbrace{\begin{bmatrix} e^{-ikz_1} & e^{ikz_1} \\ e^{-ikz_2} & e^{ikz_2} \\ \vdots & \vdots \\ e^{-ikz_m} & e^{ikz_m} \end{bmatrix}}_{\mathbf{C}} \times \underbrace{\begin{bmatrix} \hat{p}^+ \\ \hat{p}^- \end{bmatrix}}_{\mathbf{x}} = \underbrace{\begin{bmatrix} \hat{p}(z_1) \\ \hat{p}(z_2) \\ \vdots \\ \hat{p}(z_m) \end{bmatrix}}_{\mathbf{D}} \quad (5.3)$$

The number of available measurement data points (m) and the number of unknowns define the dimension of matrices presented in Equation 5.3. The number of unknowns is 2 because of the unknown complex amplitudes \hat{p}^+ and \hat{p}^- , and m is equal to the number of pressure sensors. Thus, the dimension of \mathbf{C} is $[m \times 2]$, the dimension of \mathbf{x} is $[2 \times 1]$, and the dimension of \mathbf{D} is $[m \times 1]$. By solving the following equation, a solution for Equation 5.3 is given by [80]

$$\mathbf{x} = \mathbf{C}^+ \mathbf{D}. \quad (5.4)$$

\mathbf{C}^+ is the Moore-Penrose pseudoinverse of matrix \mathbf{C} .

Equation 5.3 has a solution only if at least two independent equations exist. According to the number of pressure sensors, two cases can be identified as

follows:

- The number of pressure sensors is equal to the number of unknowns. This is known as the two-microphone method.
- The number of pressure sensors is greater than the number of unknowns. This is known as the multi-microphone method

5.2 Experimental Setup

Experiments are carried out on the impedance tube test rig illustrated in Figure 5.2. The test rig consists of a loudspeaker, a tube where the pressure sensors are located, and an absorber module composed of the backing cavity and a perforated plate. The airflow is supplied through the inlet ports on the cavity periphery and is discharged through the outlet ports on the other side of the tube. The inner diameter of the tube and the cavity is 0.092 m . Plane wave propagation in the tube is assumed below the cut-on frequency of the first higher-order mode of the impedance tube (approximately 1.7 kHz).

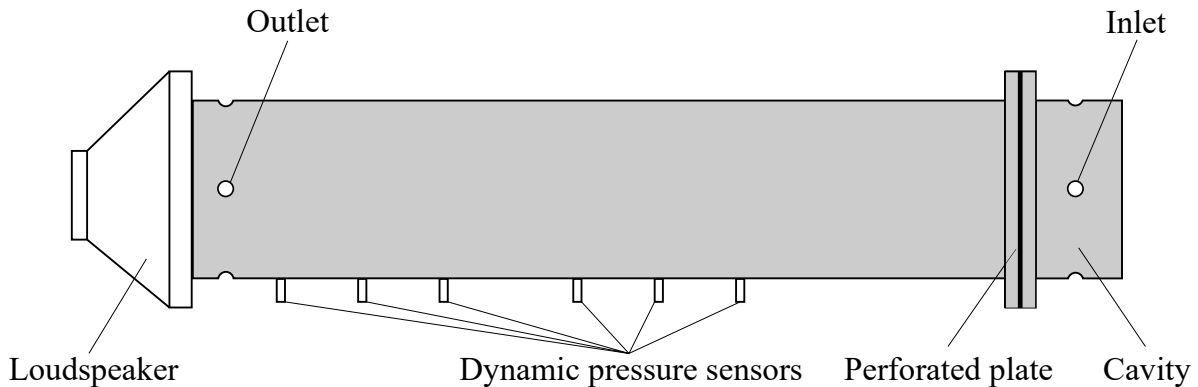


Figure 5.2: Schematic view of the impedance tube used for characterization of perforated plates.

Six dynamic pressure sensors are mounted along the tube, and the closest sensor is located at 0.215 m with reference to the perforated plate to avoid near-field effects. The acoustic pressure data are recorded and post-processed ap-

plying the multi-microphone method [73, 80, 81] to obtain the reflection coefficient R over the range of frequencies 200 – 700 Hz .

An overview of the perforated plates is shown in Figure 5.3 and Table 5.1.

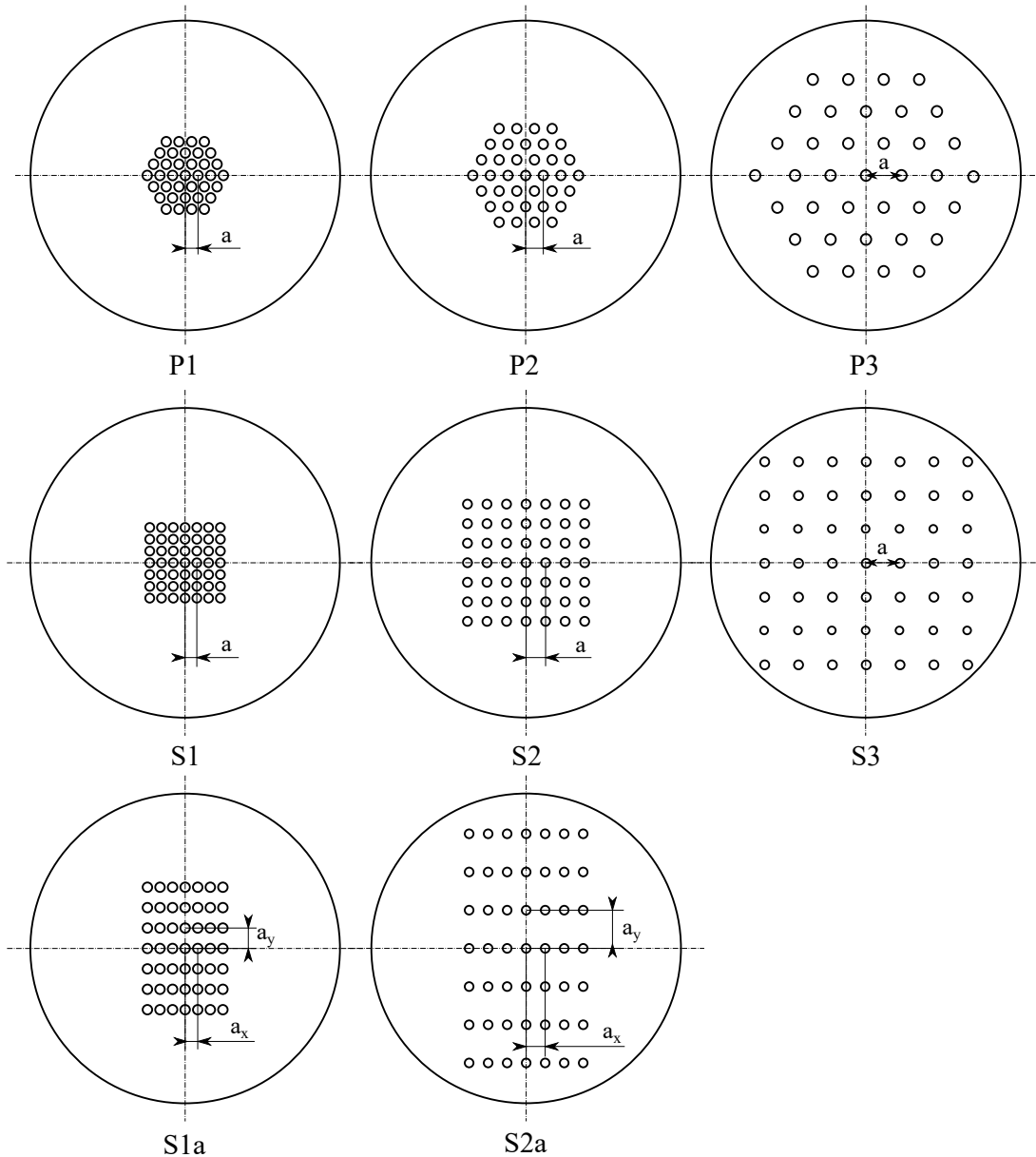


Figure 5.3: Perforated plate samples that are studied experimentally.

In the present study, for each pattern (P, S, and Sa), it is tried to keep all geometrical parameters and operating conditions constant except the spacing

of the orifices (center-to-center distance) to evaluate the effect of the hole-to-hole interaction on the damping characteristics of the perforated plates. For instance, in the configuration P, all geometrical parameters are constant for P1, P2, and P3, except the center-to-center orifice spacing.

Table 5.1: Geometrical parameters of the perforated plates that are studied experimentally.

Case Name	r_0 [mm]	Porosity [%] of cases	L_p [mm]	Center-to-center distance (a) [mm]
P1	0.8	1.1	4	2.5
P2	0.8	1.1	4	3.5
P3	0.8	1.1	4	8
S1	0.65	0.98	4	2.2
S2	0.65	0.98	4	5
S3	0.65	0.98	4	10
S1a	0.65	0.98	4	$a_x = 2.2, a_y = 5$
S2a	0.65	0.98	4	$a_x = 5, a_y = 10$

6 Results and Discussion

This chapter¹ aims to evaluate the effect of the hole-to-hole interaction on the acoustic characteristics of multi-orifice perforated plates backed by a cavity. The experimental results of the configurations in the absence of bias flow are presented, followed by the comparison with the impedance models' predictions. Then, the experimental results in the presence of bias flow are presented, and the prediction of the impedance models are compared with the experimental data and discussed.

6.1 Experimental validation without Bias Flow

This section starts by presenting the experimental results of configurations in the absence of bias flow. For these experiments, the inlet and outlet ports designed for supplying and discharging the airflow are blocked to avoid any additional damping. The investigated perforated plates are illustrated in Figure 5.3. The acoustic reflection coefficient is acquired from the measured acoustic pressures after post-processing of the raw data (described further in detail in Chapter 5).

The magnitude and phase of the reflection coefficient for pattern P are shown in Figure 6.1. Similarly, Figure 6.2 presents the magnitude and phase of the reflection coefficient for patterns S and Sa. The squares in Figure 6.2 represent S cases, while the cross markers represent Sa cases to differentiate between these two configurations.

The experimental results in Figures 6.1 and 6.2 show that the resonance frequency of the perforated plate backed by cavities shifts to higher frequencies

¹The content of this chapter is partially published in the paper GT2021-58535 - *Proceedings of ASME Turbo Expo 2021* [2]

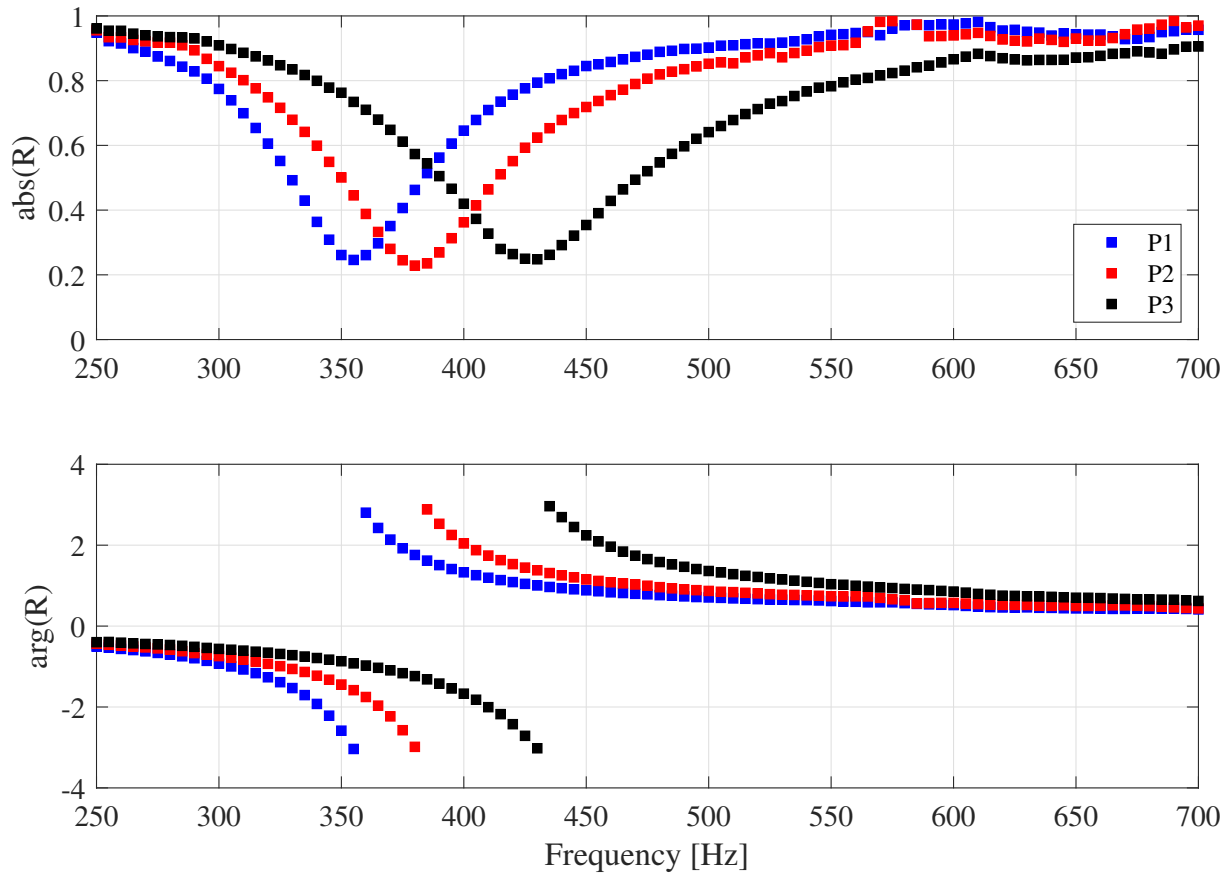


Figure 6.1: Magnitude (top) and phase (bottom) of reflection coefficient for the P pattern with the cavity length of $L_c = 30 \text{ mm}$ [2].

as the orifice spacing increases. According to Equation 4.3, the reason for this increase in resonance frequency is the decreasing end-correction because all the other geometrical parameters are kept constant except the distance between the orifices. These experimental observations are in accordance with the results of the numerical analysis presented in Chapter 4 (shown in Figures 4.8 and 4.9). Similar observations are reported by Tayong [49] and Wang et al. [51]. Wang et al. [51] explained this behavior by considering it as a result of the "combined momentum of the jet flows" when the orifices are close to each other. In contrast, this effect is less significant when the orifices are distantly spaced. However, Tayong [49] did not explicitly address this behavior and associated it with the "heterogeneity distribution effect" without further discussing this effect.

6.1 Experimental validation without Bias Flow

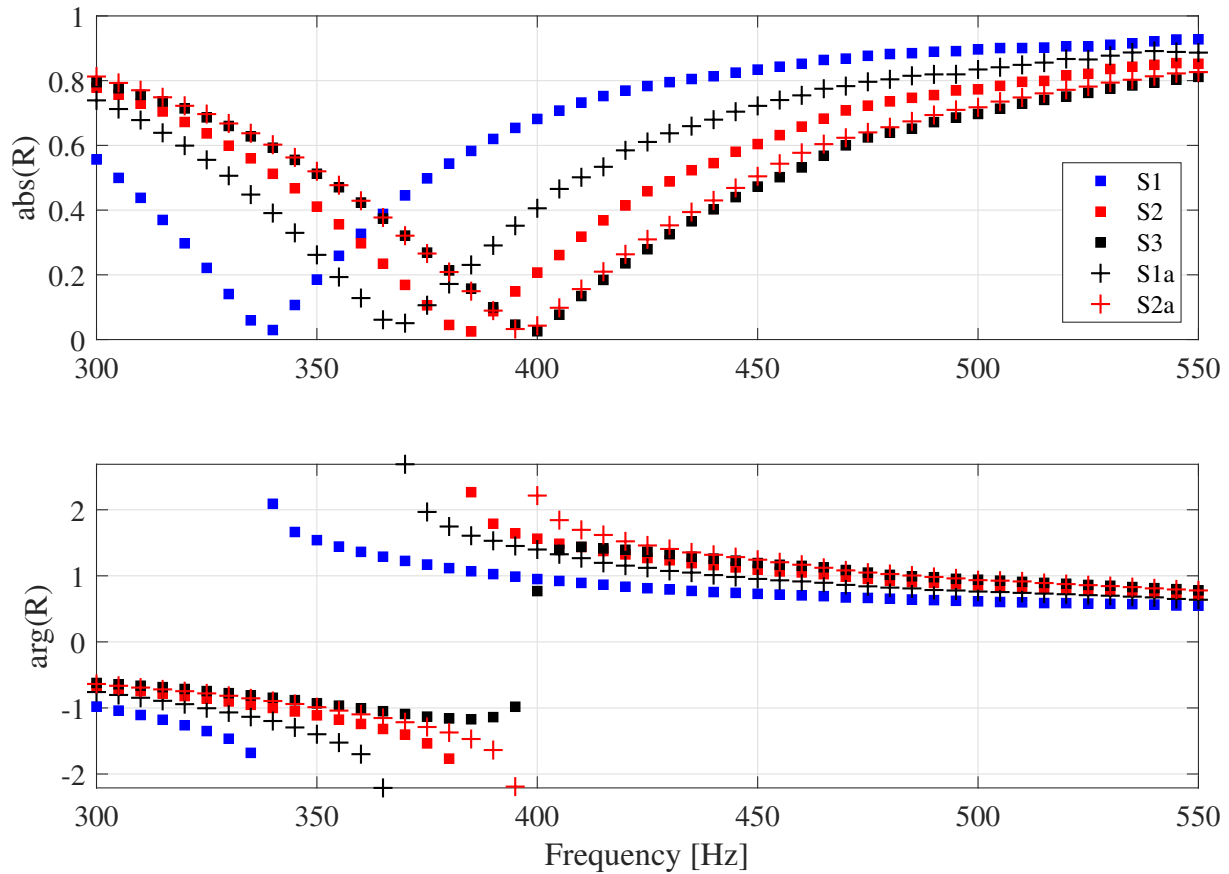


Figure 6.2: Magnitude (top) and phase (bottom) of reflection coefficient for the S and Sa patterns with the cavity length of $L_c = 30 \text{ mm}$ [2].

Similar to the behavior of the triangular pattern, the resonance frequency of the square and rectangular patterns shifts to higher frequencies when the orifice spacing increases. As shown in Figure 6.2, the resonance frequency of the S1a case is located between the S1 and S2 cases. This behavior can be explained by considering the orifice spacing in the S1a case. In the x-direction, the orifice spacing is similar to the S1 case, while in the y-direction, it is similar to the S2 case. This geometrical characteristic may result in an end-correction value between the S1 case and the S2 case, since all other geometrical parameters of the S and Sa configurations are kept constant except their orifice spacing. The resonance frequency of case S2a follows a similar behavior and falls between the S2 and S3 cases. The resonance frequency of S1a case is located between the resonance frequency of S1 and S2 cases, while the resonance fre-

quency of S2a case is close to the S3 case. The reason might be that by increasing the orifice spacing, the hole-to-hole interaction effect decreases and becomes less significant [2].

As shown in the experiments, the shift of the resonance frequency is solely related to the normalized end-correction, because all geometrical parameters kept constant, while the orifice spacing is the sole variable parameter. Therefore, according to the findings of Ingard [1] and Ih [48], the normalized end-correction is related to the orifice radius and orifice spacing. The acoustic impedance model proposed by Bellucci et al. [8] described in Section 2.6 is used to validate the numerical results with the experiments. The overall structure of Bellucci's impedance model is not altered. The only term that is modified in the current work is the end-correction term ($l'_{Bellucci}$ in Equation D.14). A new end-correction term is proposed in the current work as

$$l_{eff} = l_{h-h} \cdot l_{nl} \cdot l_B, \quad (6.1)$$

where the expressions l_{nl} and l_B account for the reduction of end-correction due to high amplitude pressure oscillations and bias flow effects, respectively. The expression l_{h-h} account for the radiation reactance as well as the hole-to-hole interaction effects. Since the effect of radiation reactance described by l'_{rad} in Equation 2.38 is related to the hole-to-hole interaction effect [1, 48], these two effects are combined and presented by the expression l_{h-h} as

$$l_{h-h} = 2 \cdot \frac{\delta (\pi \cdot r_0^2)^{1/2}}{\left[1 + \frac{(0.77kr_0)^2}{1+0.77kr_0} \right]}, \quad (6.2)$$

where δ is the normalized end-correction and is obtained from Equations 4.8 and 4.9. As mentioned earlier, the normalized end-correction considers the end-correction on one side of the orifice and is normalized by $(\pi \cdot r_0^2)^{1/2}$. Therefore, to obtain the end-correction, the normalized end-correction (δ) should be multiplied by $(\pi \cdot r_0^2)^{1/2}$ and the factor 2 (to consider for both sides of the orifice).

The general expression is proposed for the total (effective) end-correction as [2]

$$l_{eff} = 2 \cdot \frac{\delta (\pi \cdot r_0^2)^{1/2}}{\left[1 + \frac{(0.77kr_0)^2}{1+0.77kr_0}\right]} \cdot l_{nl} \cdot l_B. \quad (6.3)$$

The expression (presented in Equation 6.3) includes the effect of radiation reactance presented by Equation 2.39 and the hole-to-hole interaction effect in terms of the normalized end-correction δ . Thus, the normalized end-correction acquired from the three-dimensional analytical method and the FEM analysis can also be directly used in Equation 6.3. The final configuration of the modified Bellucci model, where the normalized end-correction is obtained from the mathematical correlations (δ_P and $\delta_{S,sa}$) is presented in Appendix D.

It is mentioned earlier in Section 2.6 that the expression l'_{nl} (Equation 2.42) accounts for the reduction of end-correction due to high amplitude pressure oscillations, and this expression is fitted to the measurements [8]. Therefore, Equation 2.42 may contain the hole-to-hole interaction effect because this effect was not taken into account in the derivation of the model for l'_{nl} [8]. In the present work, the expression l_{nl} is fitted to the experimental measurements considering the hole-to-hole interaction effect. Figure 6.3 shows the reflection coefficient curves of the S1 case from experiments with different excitation amplitude levels.

The pressure levels specified in Figure 6.3 are the acoustic pressures at the location of the perforated plate obtained from measurements. Experimental results show that increasing the excitation amplitude increases the acoustic absorption at first, and then by further increasing the amplitude, the absorption decreases while it becomes more broadband. These observations are in agreement with the findings reported in the literature [81]. Figure 6.3 presents only five excitation amplitude levels for the S1 case, while to fit the l_{nl} expression, a multitude of excitation levels for P and S configurations were used. The experimental data that are used for fitting the l_{nl} expression and the procedure to obtain the l_{nl} expression are described further in detail in Appendix B.

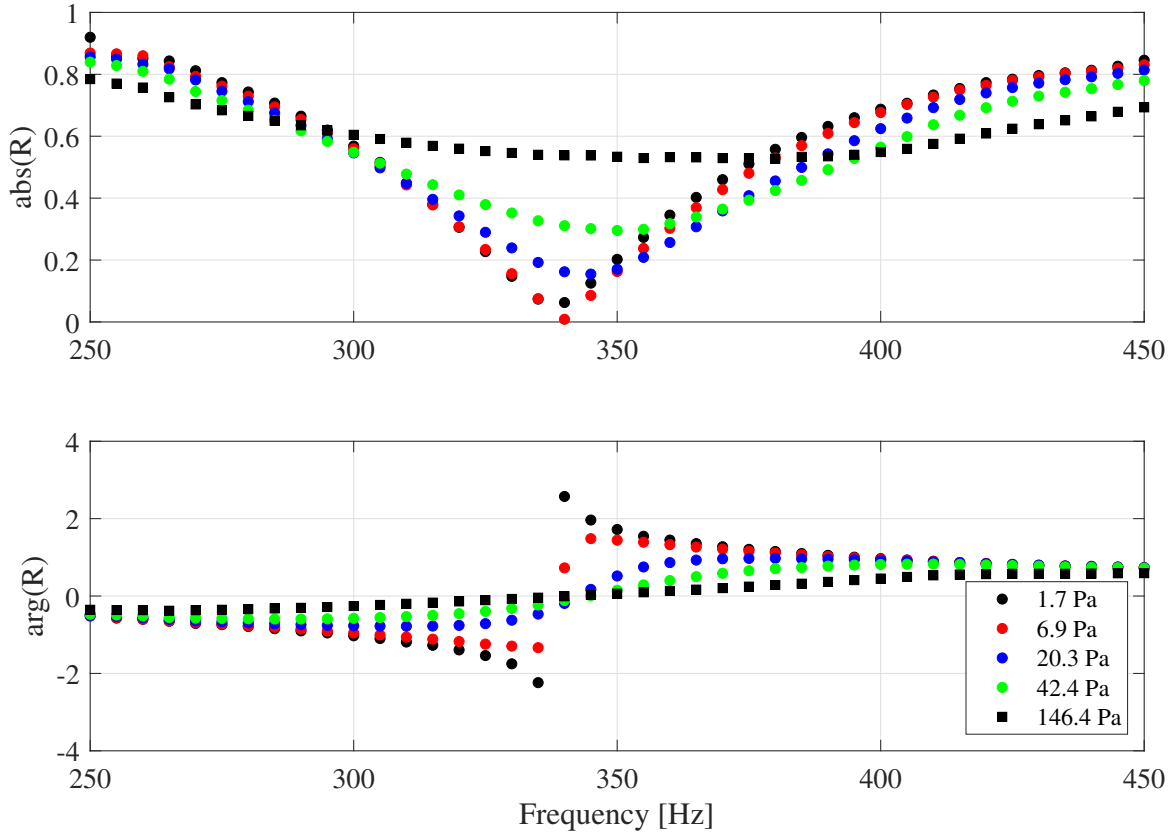


Figure 6.3: Magnitude (top) and phase (bottom) of reflection coefficient for the S1 case with the cavity length of $L_c = 30$ mm and various excitation amplitudes.

In this work, by considering the hole-to-hole interaction effect, the following expression is obtained for l_{nl} by calibrating coefficients of Equation 2.42 with the experimental data for the triangular pattern (P) as [2]

$$l_{nl}^P = 1 - \frac{0.15}{St_{ac}^{0.2}}. \quad (6.4)$$

And similarly, for the square and rectangular patterns (S and Sa) [2]

$$l_{nl}^{S,Sa} = 1 - \frac{0.09}{St_{ac}^{0.54}}. \quad (6.5)$$

The difference in the coefficients arises from the difference in the arrangement of holes in the pattern P compared to the patterns S and Sa. As mentioned earlier, in P pattern (triangular), each orifice is surrounded by six orifices, while in S and Sa patterns (square and rectangular), each orifice is surrounded by eight orifices.

For validation of the proposed mathematical correlations (presented in Equations 4.8 and 4.9) with the experimental results, P1 and S1 cases are considered.

Reflection coefficient curves for P1 and S1 are shown in Figures 6.4 and 6.5, respectively.

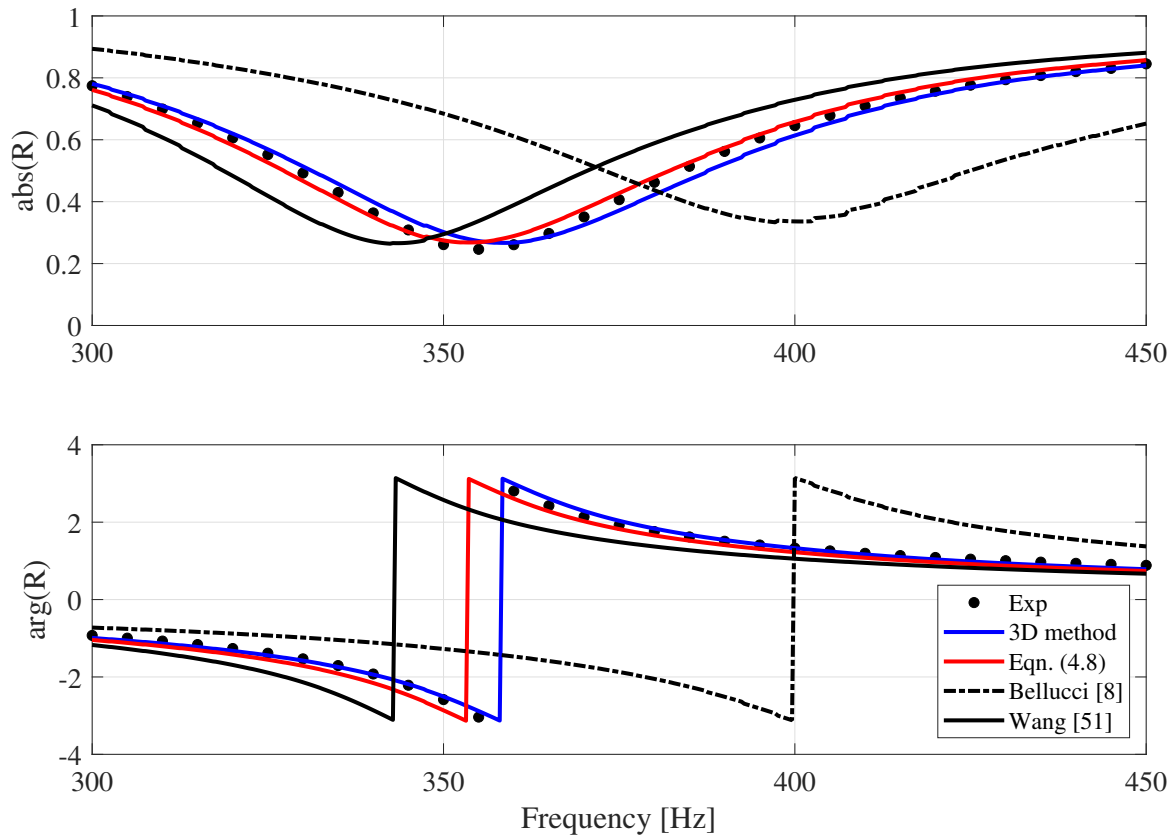


Figure 6.4: Magnitude (top) and phase (bottom) of reflection coefficient for the P1 case with the cavity length of $L_c = 30 \text{ mm}$ [2].

In Figures 6.4 and 6.5, black circles represent the experimental results, which are obtained from direct measurement of acoustic pressure in the impedance

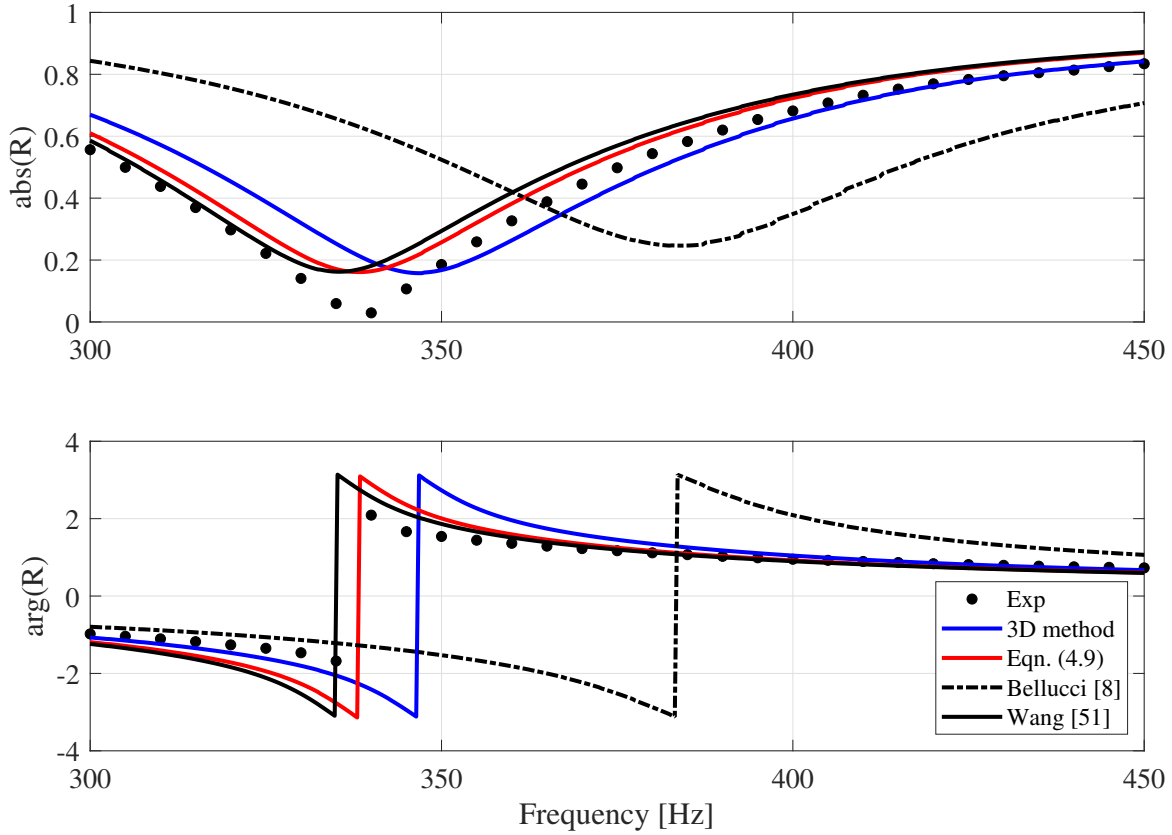


Figure 6.5: Magnitude (top) and phase (bottom) of reflection coefficient for the S1 case with the cavity length of $L_c = 30 \text{ mm}$ [2].

tube (presented in Chapter 5). Black dashed-lines represent the prediction of Bellucci's original model [8] (presented in Section 2.6). Blue solid lines represent the prediction of the modified Bellucci model, where the normalized end-correction (δ) obtained from the three-dimensional analytical model (presented in Equation 3.49) is used for the calculation of the end-correction presented in Equation 6.3. Similarly, red solid lines represent the prediction of the modified Bellucci model, where the mathematical correlations for the normalized end-correction (δ_P and $\delta_{S, Sa}$) presented in Equations 4.8 and 4.9, are used for the calculation of the end-correction presented in Equation 6.3. Solid black lines represent the prediction of the modified Bellucci model, where the end-correction term introduced by Wang et al. [51] presented in Equation 2.3, is used to obtain the total end-correction (presented in Equation 6.3). As the effect of l_{nl} is not taken into account by Wang, l_{nl} expressions obtained in the

current work (presented in Equations 6.4 and 6.5) are used to calculate the total end-correction. The FEM results are not directly used for the purpose of the comparison the reflection coefficient curves, rather the mathematical correlations obtained from FEM results are used for the purpose of validation against the experiments.

The results are presented in Figures 6.4 and 6.5. For both configurations (P1 and S1), Bellucci's original model predicts the resonance frequency higher than the experiments. The underlying reason is that the end-correction model used in Bellucci's original model (Equation 2.40) is only valid for a single orifice located in the center of a plate, and it does not account for the hole-to-hole interaction effect [2]. The three-dimensional analytical method (presented in Equation 3.49), referred to as 3D method in Figures 6.4 and 6.5, significantly improves the prediction of the resonance frequency with respect to Bellucci's original model (presented in Section 2.6). However, a slight deviation from the experiments can be noticed, which may be related to the number of higher-order modes that are considered to calculate the end-correction [2].

The prediction of the modified Bellucci's model with the end-correction term introduced by Wang et al. [51] (shown by solid black lines in Figures 6.4 and 6.5) for the resonance frequency of the S1 case is more accurate than the P1 case. Underpredicting the resonance frequency of the P1 case might be explained by the fact that the triangular configuration is not studied in Wang's work, and the end-correction expression they proposed is based on the square and rectangular configurations. The arrangement of orifices may influence the effective porosity (σ_{eff}) and consequently the end-correction, as shown in Equation 2.3.

A comparison of the predicted resonance frequencies for the perforated plates shown in Figure 5.3 is presented in Table 6.1.

The resonance frequencies predicted by the mathematical correlations (presented in Equations 4.8 and 4.9) for both configurations are in good agreement with the experimental results. On the contrary, Bellucci's original model predicts a constant resonance frequency for all P and S cases, respectively. The

Table 6.1: Predicted resonance frequency of the perforated plates investigated experimentally.

Case Name	Experiment [Hz]	Mathematical correlations Eqns. 4.8 and 4.9 [Hz]	3D method [Hz]	Bellucci et al. [8] [Hz]	Wang et al. [51] [Hz]
P1	355	352	360	400	-
P2	380	375	392	400	-
P3	435	412	447	400	-
S1	340	339	350	387	334
S2	385	381	408	387	379
S3	400	402	440	387	401
S1a	370	360	381	387	354
S2a	395	393	423	387	390

reason is that the interaction end-correction expression considered in this model (Equation 2.40) is not depending on the orifice spacing [2]. The three-dimensional analytical approach shows improvement over Bellucci's original model and predicts the resonance frequency closer to the experiments.

6.2 Experimental validation with Bias Flow

This section presents the influence of the hole-to-hole interaction in the presence of a bias flow on two representative perforated plate configurations: triangular and square patterns. The general influence of the bias flow is demonstrated with configurations P1 and S1. Figures 6.6 and 6.7 present the reflection coefficient curves for several bias flow velocities for P1 case. In Figure 6.6, squares represent the case without bias flow (as shown in Figure 6.1), and circles represent different bias flow velocities.

Without any bias flow, the P1 case exhibits a prominent absorption maximum of around 350 Hz (shown in Figure 6.6). Introducing a bias flow and increasing its velocity shifts the maximum absorption to higher frequencies. The shift in resonance frequency can be noticed in Figure 6.6, however, this

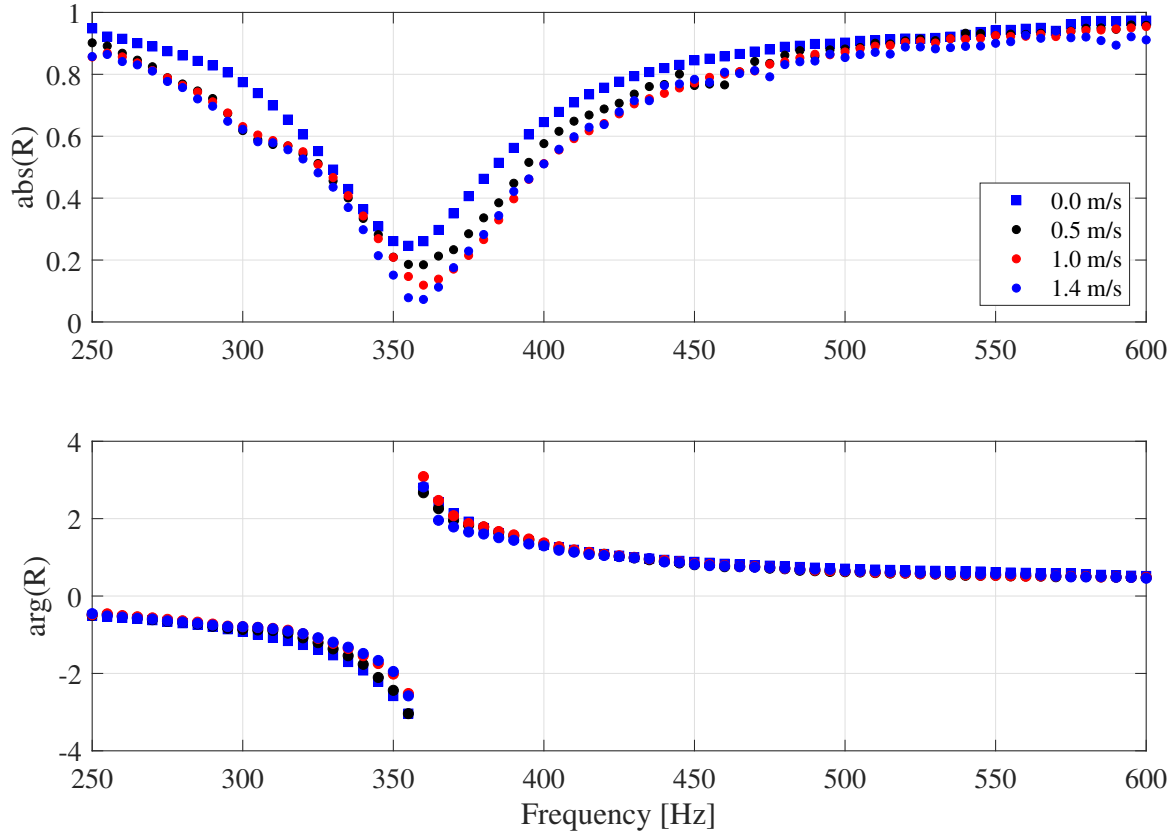


Figure 6.6: Magnitude (top) and phase (bottom) of reflection coefficient for the P1 case with the cavity length of $L_c = 30 \text{ mm}$ and various bias flow velocities (U_B).

shift is more significant at higher bias flow velocities (shown in Figure 6.7). Simultaneously, the maximum level of absorption is first increased (shown in Figure 6.6) and then reduced (shown in Figure 6.7), while the absorption becomes more broadband. This increase and decrease in the maximum level of absorption by increasing bias flow velocity is in agreement with the observations reported in the literature [81].

In Figure 6.6, without any bias flow, the resonance damping behavior characterized by a minimum of the reflection coefficient magnitude and a phase shift equal to $\pm\pi$, is shown by squares. The bias flow influences this resonance effect up to a sufficiently high bias flow velocity. As shown in Figure 6.6, increasing bias flow velocity affects the magnitude of the reflection coefficient by in-

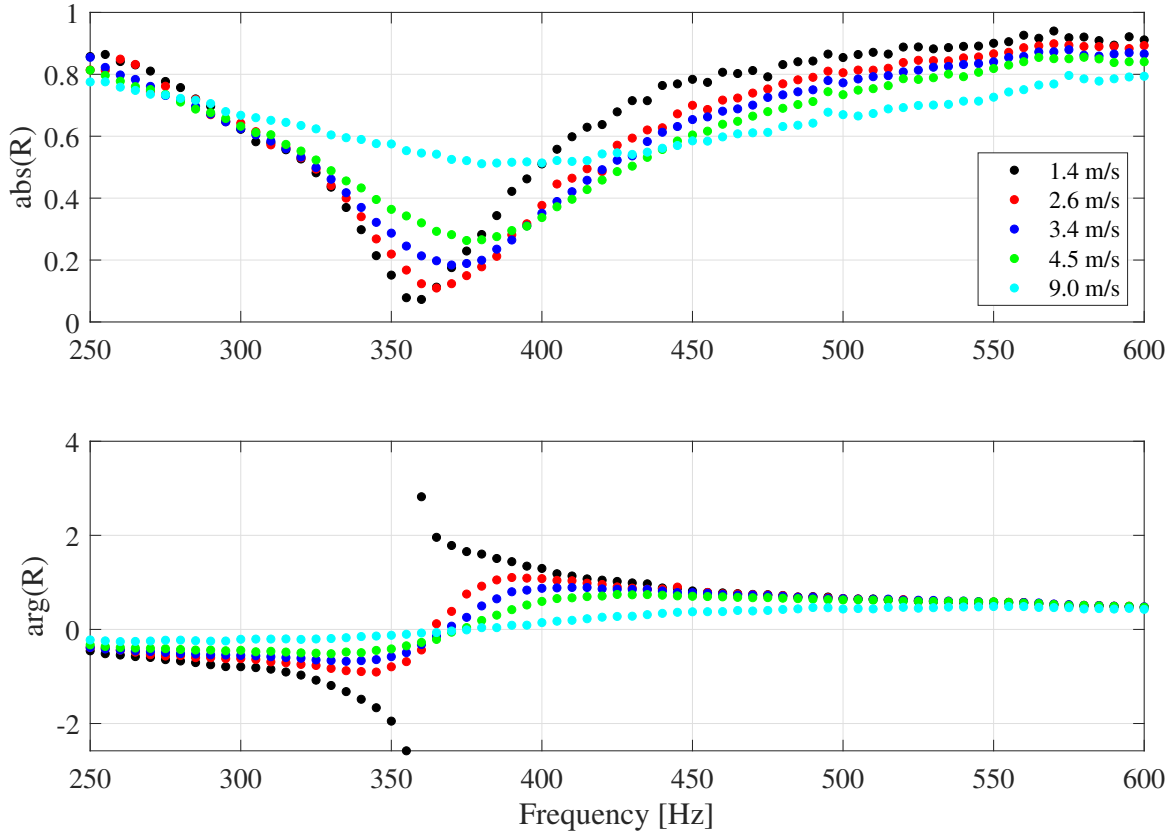


Figure 6.7: Magnitude (top) and phase (bottom) of reflection coefficient for the P1 case with the cavity length of $L_c = 30 \text{ mm}$ and various bias flow velocities (U_B).

creasing the damping level due to the enhanced vortex shedding. While, the phase is not significantly affected. Beyond a sufficiently high bias flow velocity ($U_B = 1.4 \text{ m/s}$) in Figure 6.7, the bias flow dominates and the phase shift starts to decrease by increasing the bias flow velocity. The decrease in the phase shift may be related to the reduced reactance when the bias flow velocity is increasing. This behavior is somewhat related the Strouhal number, as mentioned by Lahiri [81].

Figure 6.8 presents the reflection coefficient curves for several bias flow velocities for S1 case. For the S1 case, similar to the P1 case, introducing a bias flow shifts the maximum absorption to higher frequencies while the absorption becomes broadband. Similar behavior is observed for all perforated plates stud-

ied (shown in Figure 5.3). The results show that bias flow reduces the maximum absorption, while becoming more broadband compared to the condition without bias flow. These observations comply with the finding reported in [8, 16, 81–85].

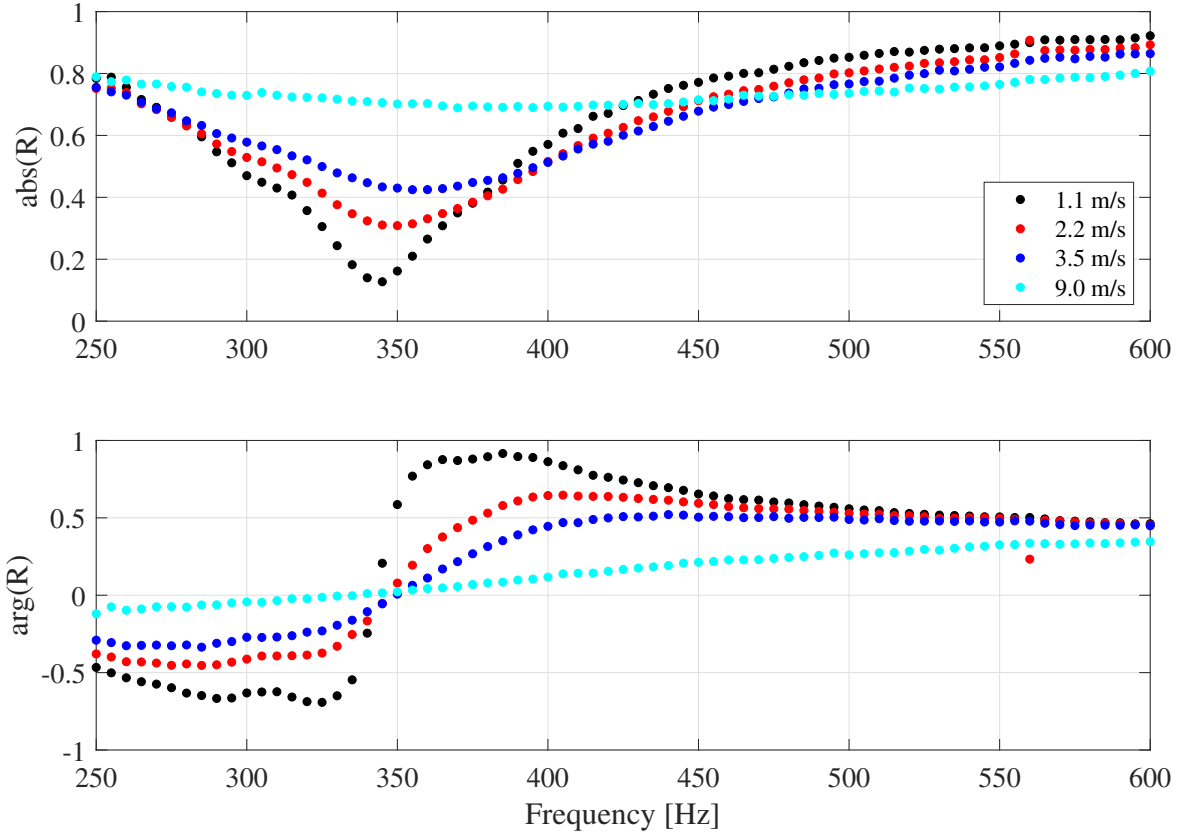


Figure 6.8: Magnitude (top) and phase (bottom) of reflection coefficient for the S1 case with the cavity length of $L_c = 30 \text{ mm}$ and various bias flow velocities (U_B).

Before comparing the prediction of the models, it is necessary to evaluate the bias flow end-correction expression l'_B proposed by Bellucci et al. [8]. As mentioned in Section 2.6, the expression l'_B (Equation 2.41), which considers the reduction of end-correction due to bias flow, is fitted to the experimental data [8]. Thus, Equation 2.41 may contain the hole-to-hole interaction effect, since this effect was not taken into account in the derivation of the expression for l'_B [8]. Since in the current study, the effect of hole-to-hole interaction is considered separately, the l_B expression should be evaluated because the l'_B

expression proposed by Bellucci et al. [8] (presented in Equation 2.41) cannot be used. In the current study, the l_B expression is fitted to the experimental results. The experimental data that are used for fitting the l_B expression and the procedure to obtain this expression are described in Appendix C.

In the current work, the following expressions are proposed for l_B by keeping the original shape of the expression l_B (Equation 2.41) and re-calibrating its coefficients with the experimental data for the triangular pattern (P)

$$l_B^P = \frac{0.3(a_P/St^2) + 1}{a_P/St^2 + 1} \quad ; \quad a_P = 23 \left(\frac{Re_q}{R} \right)^3. \quad (6.6)$$

Similarly, for the square and rectangular patterns (S and Sa)

$$l_B^{S,Sa} = \frac{0.3(a_S/St^2) + 1}{a_S/St^2 + 1} \quad ; \quad a_S = 2.4 \left(\frac{Re_q}{R} \right)^2. \quad (6.7)$$

In Equation 2.41, Bellucci considered a constant value of 6 instead of parameters a_P and a_S in Equations 6.6 and 6.7. Since the center-to-center orifice spacing affects the velocity profile in the vicinity of the orifices, the reduction of the end-correction due to bias flow (represented by the expression l_B) may be affected by the center-to-center orifice spacing, too. Thus, the effect of the center-to-center orifice spacing (or in general, hole-to-hole interaction) is included in the expression l_B by parameters a_P and a_S . Introducing the term $\left(\frac{Re_q}{R}\right)$, enables the expression proposed by Bellucci presented in Equation 2.41 to consider the effect of hole-to-hole interaction. These two expressions can be integrated into the end-correction expression presented in Equation 6.3.

For comparison, the impedance model proposed by Bellucci [8] is used, and the expressions l_B that are obtained from the regression analysis (presented in Equations 6.6 and 6.7) are integrated into the end-correction expression (Equation 6.3). Then, the acoustic reflection coefficient is compared with the experimental data and Bellucci's original model. In addition, the impedance model proposed by Jing et al. [16] (presented in Section 2.5) is used to predict the acoustic behavior of the perforated plates backed by a cavity. In the fol-

Following section, the end-correction model proposed by Wang et al. [51] is not considered for the comparison because their model does not account for bias flow.

Figures 6.9 and 6.10 present the comparison of the reflection coefficient curves for the S1 case at the bias flow velocities $U_B = 1.1 \text{ m/s}$ and $U_B = 4.5 \text{ m/s}$, respectively.

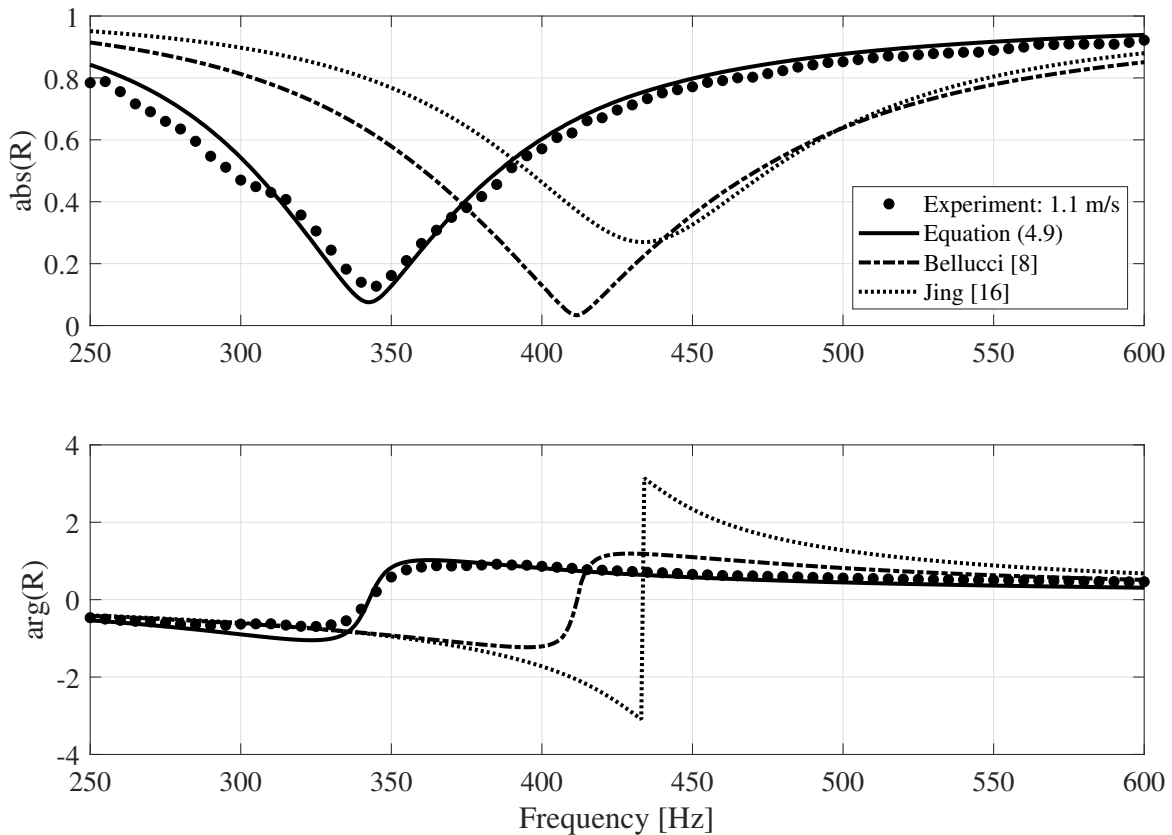


Figure 6.9: Comparison of the model predictions for the magnitude (top) and phase (bottom) of reflection coefficient for the S1 case with the cavity length of $L_c = 30 \text{ mm}$ at the bias flow velocity $U_B = 1.1 \text{ m/s}$.

In Figures 6.9 and 6.10, circles represent the experimental results, which are obtained from direct measurement of acoustic pressure in the impedance tube (presented in Chapter 5). Black dashed-lines represent the prediction of Bellucci's original model (presented in Section 2.6). Black dotted-lines represent the prediction of Jing model presented in Section 2.5. The solid black lines

represent the prediction of the modified Bellucci model, where the mathematical correlation for the normalized end-correction ($\delta_{s,sa}$) presented in Equation 4.9, is used for the calculation of the end-correction presented in Equation 6.3.

In terms of the location of the resonance frequency and the magnitude of damping, the general trend is accurately predicted by the modified Bellucci model, where the mathematical correlation for the normalized end-correction ($\delta_{s,sa}$) presented in Equation 4.9, is used for the calculation of the end-correction presented in Equation 6.3. Bellucci's original model predicts the damping level in good agreement with the experimental results. However, the resonance frequency is not accurate (with a deviation of approximately 70 Hz). The reason for the over-prediction of the resonance frequency by original Bellucci's model is that the end-correction model used in this model is not valid for multi-orifice perforated plates, and therefore, it lacks the hole-to-hole interaction effect. Including this effect by using the expression $l_B^{S,sa}$ presented in Equation 6.7 improves the model's prediction significantly. Similar to Bellucci's original model, Jing's model over-predicts the maximum absorption frequency. The reason is that, although Jing's model improved Howe's Rayleigh conductivity model by including the plate thickness, it does not consider any end effect. Additionally, Jing's model does not predict the magnitude of absorption accurately. This behavior can be explained by the resistance term of Jing's model, which considers the vortex shedding phenomenon only. In contrast, Bellucci's original model considers several resistance terms (Equation 2.32). The selection criteria of these resistance terms is based on the ratio of the mean bias flow velocity (U_B) and the acoustic velocity (u'), in the presence of a bias flow. Figure 6.10 shows the comparison of the impedance models at a bias flow velocity of $U_B = 4.5 \text{ m/s}$.

Similar to the lower bias flow velocity, the modified Bellucci model with the mathematical correlation presented in Equation 4.9 for the calculation of the end-correction, predicts the resonance frequency and the damping level accurately. In comparison, Bellucci's original model and Jing's model locate the maximum absorption at higher frequencies. Jing's model predicts the magnitude of the reflection coefficient in good agreement with the experiments

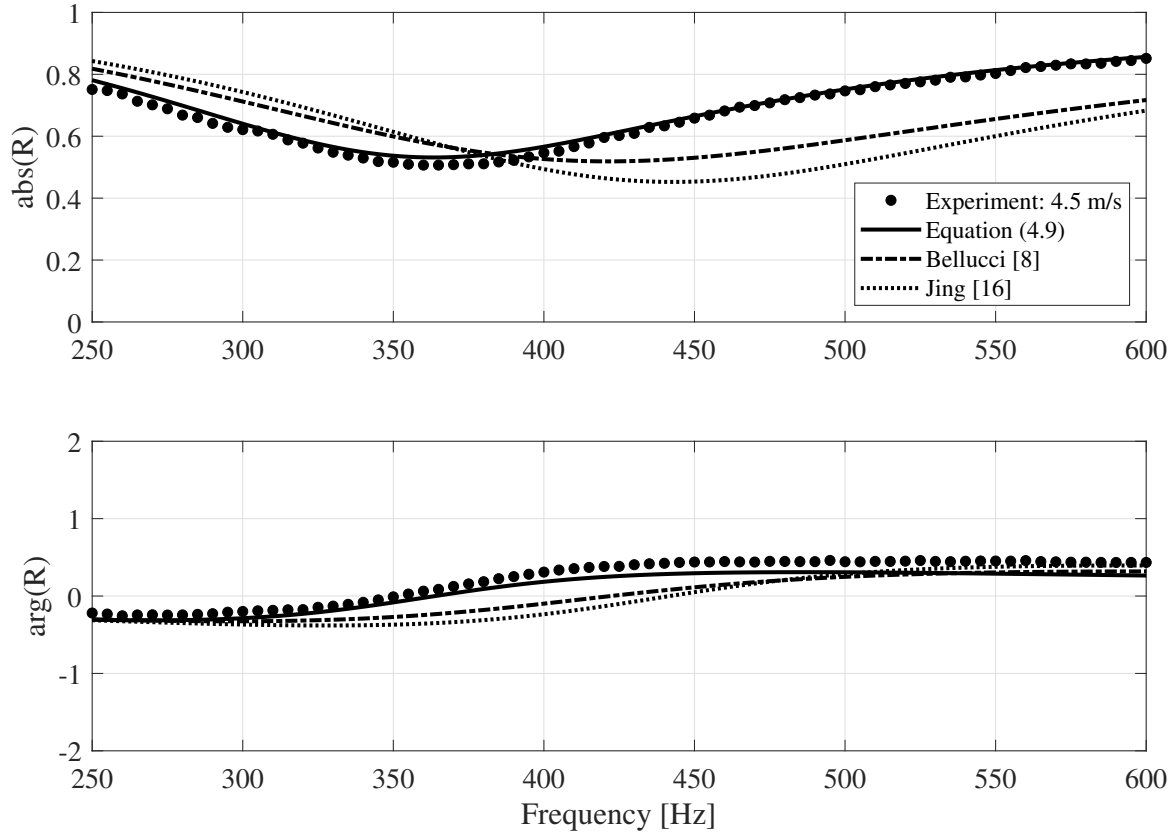


Figure 6.10: Comparison of the model predictions for the magnitude (top) and phase (bottom) of reflection coefficient for the S1 case with the cavity length of $L_c = 30 \text{ mm}$ at the bias flow velocity $U_B = 4.5 \text{ m/s}$.

at this bias flow velocity, similar to Bellucci's original model. It can be concluded that Jing's model can predict the absorption level accurately when the bias flow velocity is sufficiently high. In contrast, Bellucci's original model can be used for all levels of bias flow. At the bias flow velocity of $U_B = 4.5 \text{ m/s}$, it can be seen that both Bellucci's original model and Jing's model predict the same level of absorption because they employ the resistance term of Howe's Rayleigh conductivity model. The difference in the absorption level might be related to the reactance term of Bellucci's original model, where function Γ is a complex quantity and translates the effect of orifice length also into the resistance term. Therefore, the resulting resistance term of Bellucci's original model differs slightly from Jing's model.

Figure 6.11 presents the comparison of the impedance models for the P1 case at a bias flow velocity of $U_B = 4.5 \text{ m/s}$.

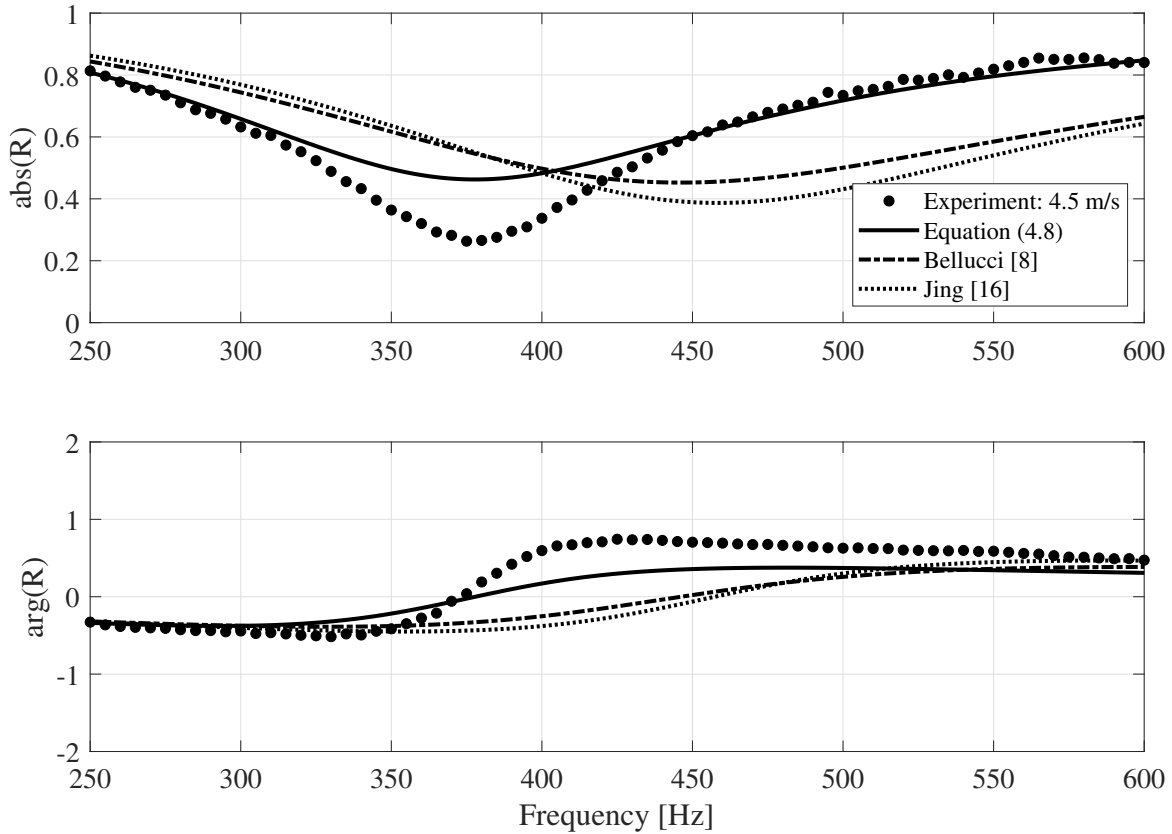


Figure 6.11: Comparison of the model predictions for the magnitude (top) and phase (bottom) of reflection coefficient for the P1 case with the cavity length of $L_c = 30 \text{ mm}$ at the bias flow velocity $U_B = 4.5 \text{ m/s}$.

In Figure 6.11, circles represent the experimental results, which are obtained from direct measurement of acoustic pressure in the impedance tube (presented in Chapter 5). Black dashed-line represents the prediction of the original Bellucci model (presented in Section 2.6). Black dotted-line represents the prediction of Jing model presented in Section 2.5. The solid black line represents the prediction of the modified Bellucci model, where the mathematical correlation for the normalized end-correction (δ_P) presented in Equation 4.8, is used for the calculation of the end-correction presented in Equation 6.3.

As the results show, the modified Bellucci model with the mathematical correlation presented in Equation 4.8 for the calculation of the end-correction can accurately predict the resonance frequency of the triangular pattern, similar to the square pattern (S1). Again, Bellucci's original model and Jing's model locate the maximum absorption with significant deviation from the experiments. In addition, a deviation between the absorption level of the experiments and all the models can be observed. Such deviation was not observed in the S1 case. Because of the hexagonal arrangement of the orifices in the P1 case, the orifices are more closely distributed than in the S1 case, resembling a larger orifice. Therefore, the resistance effect might be intensified in terms of vortex shedding and visco-thermal damping. In addition, the orifices in the P1 case are more tightly spaced compared to the S1 case.

7 Summary

The presented study has demonstrated the influence of the non-planar wave propagation and geometrical parameters such as orifice center-to-center distance on the resonance frequency of multi-orifice perforated plates backed by a cavity.

As a result of this work, a three-dimensional analytical method was developed to consider the non-planar wave propagation at the orifice-plate area discontinuity in multi-orifice perforated plates. The results showed that the calculated end-correction first increases with the number of considered higher-order modes and then converges quickly. One major shortcoming of this method is the excessive computational cost associated with the number of considered higher-order modes.

Furthermore, to investigate the propagation of the acoustic waves through small orifices, a three-dimensional, numerical method in frequency space for the computation of the wave propagation described by the Helmholtz equation using FEM was developed. Several perforated plates (triangular, square, and rectangular orifice patterns) backed by a cavity are studied, and the effect of hole-to-hole interaction is studied. For all investigated perforated plates similar behavior is observed, i.e., acoustic reactance curves shift to lower frequencies as the distance between orifices decreases. This decrease in resonance frequency implies that the end-correction increases by decreasing the orifice spacing. It is shown that the oscillating mass of each orifice is not significantly affected by the adjacent orifices, when the holes are distantly spaced, while, the acoustic radiation of orifices is significantly influenced by the neighboring holes when the orifices are closely distributed.

The knowledge of the correct end-correction is essential for the accurate prediction of the resonance frequency of the perforated plates backed by the cav-

ity. Thus, mathematical correlations for the normalized end-correction (δ_P and $\delta_{S,sa}$) are obtained using the FEM results.

Several perforated plate configurations (triangular, square, and rectangular orifice patterns) backed by a cavity were investigated experimentally. Experimental results showed that the resonance frequency location is sensitive to the hole-to-hole interaction effect. The resonance frequency shifts to the higher frequencies by increasing the orifice spacing for the perforated plates with the same orifice radius and pattern. The observations showed that this shift in the resonance frequency is associated with the variation in the end-correction value due to the hole-to-hole interaction effect, as all the geometrical and operating parameters are kept constant except the center-to-center orifice spacing. Similar to the experiments without a bias flow, the same behavior is observed in the experiments with the bias flow.

Moreover, the mathematical correlations for the normalized end-correction (δ_P and $\delta_{S,sa}$) obtained from FEM results were integrated into an impedance model. Similarly, the normalized end-correction obtained from the three-dimensional analytical method was integrated into the impedance model. The prediction of the impedance models with the mathematical correlations (δ_P and $\delta_{S,sa}$) and the normalized end-correction obtained from three-dimensional analytical method are compared with the experimental results. The comparisons demonstrated that neglecting the hole-to-hole interaction effect may result in an over-prediction of the resonance frequency. The impedance model with the mathematical correlations (δ_P and $\delta_{S,sa}$) can accurately predict the resonance frequency of the perforated plates backed by a cavity, and can be easily applied to different orifice patterns and orifice radii in a plate. Therefore, the impedance model with the mathematical correlations (δ_P and $\delta_{S,sa}$) is applicable in the design of multi-orifice perforated plates for acoustic attenuation in practical applications, such as perforated liners in gas turbines.

Appendices

A Modeling Details

As mentioned in page 40, in this section the development of the equations that describe the boundary conditions is presented.

For the pressure boundary condition, multiply both sides of Equation 3.45 with $J_t(b_{ts}r/r_0)\cos(t\theta)dA$ and integrate over A_h to get, for $t = 0$ and $s = 0$

$$\begin{aligned}
 (Ai_{00} + Bi_{00}) \frac{r_0}{2} = & \\
 C_{00} [1 + e^{-2ikL_c}] \frac{r_0}{2} + & \\
 \sum_{n=1}^{\infty} C_{0n} [1 + e^{2ik_{z,0n}^{II}L_c}] \frac{1}{k_{r,0n}^{II}} J_0(k_{r,0n}^{II}d_i) J_1(k_{r,0n}^{II}r_0) + & \quad (A.1) \\
 \sum_{m=1}^{\infty} \sum_{n=0}^{\infty} C_{mn} e^{-im\theta_i} [1 + e^{2ik_{z,mn}^{II}L_c}] \frac{1}{k_{r,mn}^{II}} J_m(k_{r,mn}^{II}d_i) J_1(k_{r,mn}^{II}r_0). &
 \end{aligned}$$

For $t = 0, s = 1, 2, 3, \dots, \infty$

$$\begin{aligned}
 (Ai_{0s} + Bi_{0s}) \frac{r_0}{2} J_0(k_{r,0s}^I r_0) = & \\
 \sum_{n=1}^{\infty} C_{0n} [1 + e^{2ik_{z,0n}^{II}L_c}] \frac{k_{r,0n}^{II}}{(k_{r,0s}^I)^2 - (k_{r,0n}^{II})^2} J_0(k_{r,0n}^{II}d_i) J_0'(k_{r,0n}^{II}r_0) + & \\
 \sum_{m=1}^{\infty} \sum_{n=0}^{\infty} (C_{mn} e^{-im\theta_i}) [1 + e^{2ik_{z,mn}^{II}L_c}] \frac{k_{r,mn}^{II}}{(k_{r,0s}^I)^2 - (k_{r,mn}^{II})^2} \times & \quad (A.2) \\
 J_m(k_{r,mn}^{II}d_i) J_0'(k_{r,mn}^{II}r_0). &
 \end{aligned}$$

For $t = 1, 2, 3, \dots, \infty$, $s = 0, 1, 2, \dots, \infty$

$$\begin{aligned}
 & (Ai_{ts} + Bi_{ts}) \frac{r_0}{2} \left(1 - \frac{t^2}{(k_{r,ts}^I r_0)^2} \right) J_t(k_{r,ts}^I r_0) = \\
 & \sum_{n=1}^{\infty} C_{0n} \left[1 + e^{2ik_{z,0n}^{II} L_c} \right] \frac{k_{r,0n}^{II}}{(k_{r,ts}^I)^2 - (k_{r,0n}^{II})^2} J_t(k_{r,0n}^{II} d_i) J'_t(k_{r,0n}^{II} r_0) + \\
 & \sum_{m=1}^{\infty} \sum_{n=0}^{\infty} \left[C_{mn} \left(1 + e^{2ik_{z,mn}^{II} L_c} \right) J_{m+t}(k_{r,mn}^{II} d_i) e^{-im\theta_i} (-1)^t \times \right. \\
 & \left. \frac{k_{r,mn}^{II}}{(k_{r,ts}^I)^2 - (k_{r,mn}^{II})^2} J'_t(k_{r,mn}^{II} r_0) \right].
 \end{aligned} \tag{A.3}$$

For velocity boundary condition for $t = 0$ and $s = 0$

$$\sum_{i=1}^M [Ai_{00} - Bi_{00}] r_0^2 = C_{00} [1 - e^{-2ikL_c}] R_c^2, \tag{A.4}$$

where M stands for the number of orifices.

For $t = 0$, $s = 1, 2, 3, \dots, \infty$

$$\begin{aligned}
 & \sum_{i=1}^M \left[(Ai_{00} - Bi_{00}) \frac{r_0}{k_{r,0s}^{II}} J_0(k_{r,0s}^{II} d_i) J_1(k_{r,0s}^{II} r_0) + \right. \\
 & \sum_{n=1}^{\infty} (Ai_{0n} - Bi_{0n}) \frac{k_{z,0n}^I}{k} \frac{r_0 k_{r,0s}^{II}}{(k_{r,0n}^I)^2 - (k_{r,0s}^{II})^2} J_0(k_{r,0s}^{II} d_i) J_0(k_{r,0n}^I r_0) J'_0(k_{r,0s}^{II} r_0) + \\
 & \left. \sum_{m=1}^{\infty} \sum_{n=0}^{\infty} (Ai_{mn} - Bi_{mn}) \times \frac{k_{z,mn}^I}{k} \frac{r_0 k_{r,0s}^{II}}{(k_{r,mn}^I)^2 - (k_{r,0s}^{II})^2} J_m(k_{r,0s}^{II} d_i) J_m(k_{r,mn}^I r_0) J'_m(k_{r,0s}^{II} r_0) \right] \\
 & = \frac{k_{z,0s}^{II}}{k} C_{0s} \left[1 - e^{-2ik_{z,0s}^{II} L_c} \right] \frac{R_c^2}{2} J_0^2(k_{r,0s}^{II} R_c).
 \end{aligned} \tag{A.5}$$

Similarly, for $t = 1, 2, 3, \dots, \infty$, $s = 0, 1, 2, \dots, \infty$,

$$\begin{aligned}
& \sum_{i=1}^M \left[(Ai_{00} - Bi_{00}) e^{-it\theta_i} \frac{r_0}{k_{r,ts}^{II}} \times J_t(k_{r,ts}^{II} d_i) J_1(k_{r,ts}^{II} r_0) + \right. \\
& \sum_{n=1}^{\infty} Ai_{0n} e^{-it\theta_i} \left[1 - e^{-2ik_{z,0n}^I L_p} \right] \frac{k_{z,0n}^I}{k} \frac{r_0 k_{r,ts}^{II}}{(k_{r,0n}^I)^2 - (k_{r,ts}^{II})^2} \times J_t(k_{r,ts}^{II} d_i) J_0(k_{r,0n}^I r_0) J_0'(k_{r,ts}^{II} r_0) + \\
& \sum_{m=1}^{\infty} \sum_{n=0}^{\infty} (Ai_{mn} - Bi_{mn}) e^{-it\theta_i} (-1)^m J_{t-m}(k_{r,ts}^{II} d_i) \frac{k_{z,mn}^I}{k} \frac{r_0 k_{r,ts}^{II}}{(k_{r,mn}^I)^2 - (k_{r,ts}^{II})^2} \\
& \left. J_m(k_{r,mn}^I r_0) J_m'(k_{r,ts}^{II} r_0) \right] = \frac{k_{z,ts}^{II}}{k} C_{ts} \left[1 - e^{-2ik_{z,ts}^{II} L_c} \right] \frac{R_c^2}{2} J_t^2(k_{r,ts}^{II} R_c) \left(1 - \frac{t^2}{k_{r,ts}^{II} R_c^2} \right). \tag{A.6}
\end{aligned}$$

By forming a matrix set of Equations 3.40, 3.41, and A.1 to A.6 containing the description of boundary conditions, the solution of the acoustic field inside the domain may be determined. The pressure amplitudes for waves Ai_{mn} , Bi_{mn} , and C_{mn} are unknowns. By solving this set of equations for a finite number of higher-order modes, the pressure amplitudes can be obtained.

As mentioned in Chapter 2, the multi-dimensional effects associated with the evanescent higher-order modes created at area discontinuities can be considered by introducing an acoustic length correction (l'). In the following, the procedure of obtaining Equation 3.48 is briefly described.

Considering the domain shown in Figure 3.1, at the area jump between the orifice and the cavity, the continuity of sound pressure requires [45]

$$\hat{p}_{00}^I + \hat{p}_h^I = \hat{p}_{00}^{II} + \hat{p}_h^{II} \quad \text{at } z = 0, \text{ on } A_h \tag{A.7}$$

where the subscripts 00 and h represent the fundamental mode (0,0) and the higher-order modes, respectively. Below the cut-on frequency of the first higher-order mode, only the fundamental mode (0,0) can propagate, and the

discontinuity can be equivalent to the equation [52]

$$\hat{p}_{00}^I - \hat{p}_{00}^{II} = z \hat{u}_{00}^I, \quad (\text{A.8})$$

where z is lumped specific impedance and \hat{u}_{00}^I the acoustic velocity of the fundamental mode at the orifice-cavity interface ($z = 0$). The lumped impedance can be written as [69]

$$z = i\omega\rho l' = \frac{\hat{p}_h^I - \hat{p}_h^{II}}{\hat{u}_{00}^I} = \frac{\hat{p}_{00}^I - \hat{p}_{00}^{II}}{\hat{u}_{00}^I}, \quad (\text{A.9})$$

where the l' is the acoustic length correction of the orifice, and can be calculated using the following formula [52, 71, 86]

$$l' = \frac{\hat{p}_{00}^I - \hat{p}_{00}^{II}}{i\omega\rho\hat{u}_{00}^I} = \frac{(Ai_{00} + Bi_{00}) - C_{00}(1 + e^{-2ikL_c})}{ik(Ai_{00} - Bi_{00})}. \quad (\text{A.10})$$

In the current study, the length correction of each orifice (l') is normalized by the square root of the orifice area $\sqrt{\pi r_0^2}$. The normalized end-correction for each orifice (δ_i) can be calculated using the following formula

$$\delta_i = \frac{\hat{p}_{00}^I - \hat{p}_{00}^{II}}{i\omega\rho\hat{u}_{00}^I (\pi \cdot r_0^2)^{1/2}} = \frac{(Ai_{00} + Bi_{00}) - C_{00}(1 + e^{-2ikL_c})}{ik(Ai_{00} - Bi_{00}) (\pi \cdot r_0^2)^{1/2}}. \quad (\text{A.11})$$

B Re-calibration of the Coefficients of the Expression l_{nl}

As mentioned in page 80, the coefficients of the expression l_{nl} are re-calibrated using the experimental data. This section presents the experimental results that are used for re-calibration of the coefficients of the expression l_{nl} , followed by describing the procedure to obtain the expression l_{nl} for the triangular, square, and rectangular patterns separately.

Figure B.1 presents the reflection coefficient curves of sixteen excitation amplitude levels for the S1 case, which are obtained from direct measurement of acoustic pressure in the impedance tube.

For the purpose of re-calibrating the coefficients of the expression l_{nl} , the data set is selected accurately so that the data set which is used for validation is excluded from the regression data set. Then, approximately 75% of the data set is used for the regression and the remaining data points are used to evaluate the accuracy of the fitted expression. This regression data set includes the lowest and highest excitation levels. The same procedure is applied to the P configuration. The experimental results, which are obtained from direct measurement of acoustic pressure in the impedance tube, are used for re-calibrating the coefficients of the expression l_{nl} for P configuration are presented in Figure B.2.

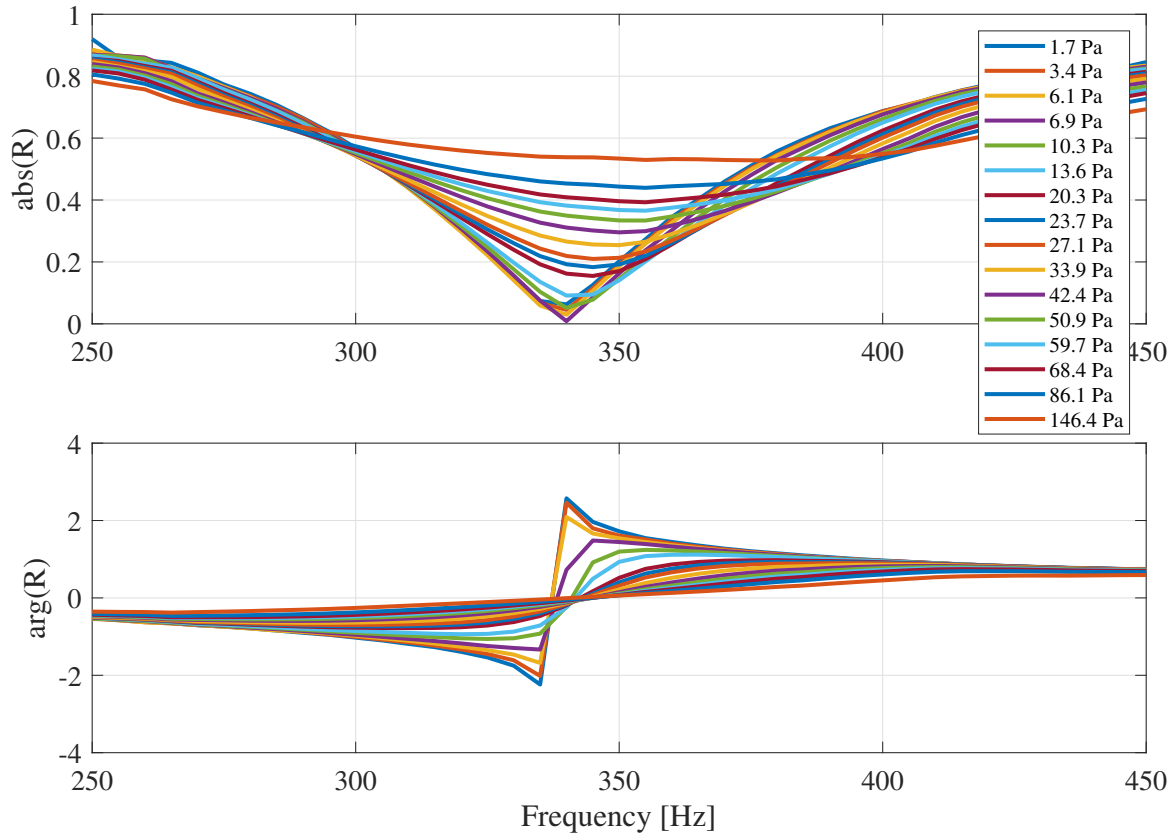


Figure B.1: Magnitude (top) and phase (bottom) of reflection coefficient for the S1 case with the cavity length of $L_c = 30 \text{ mm}$ and various excitation amplitudes obtained from direct measurement of acoustic pressure in the impedance tube.

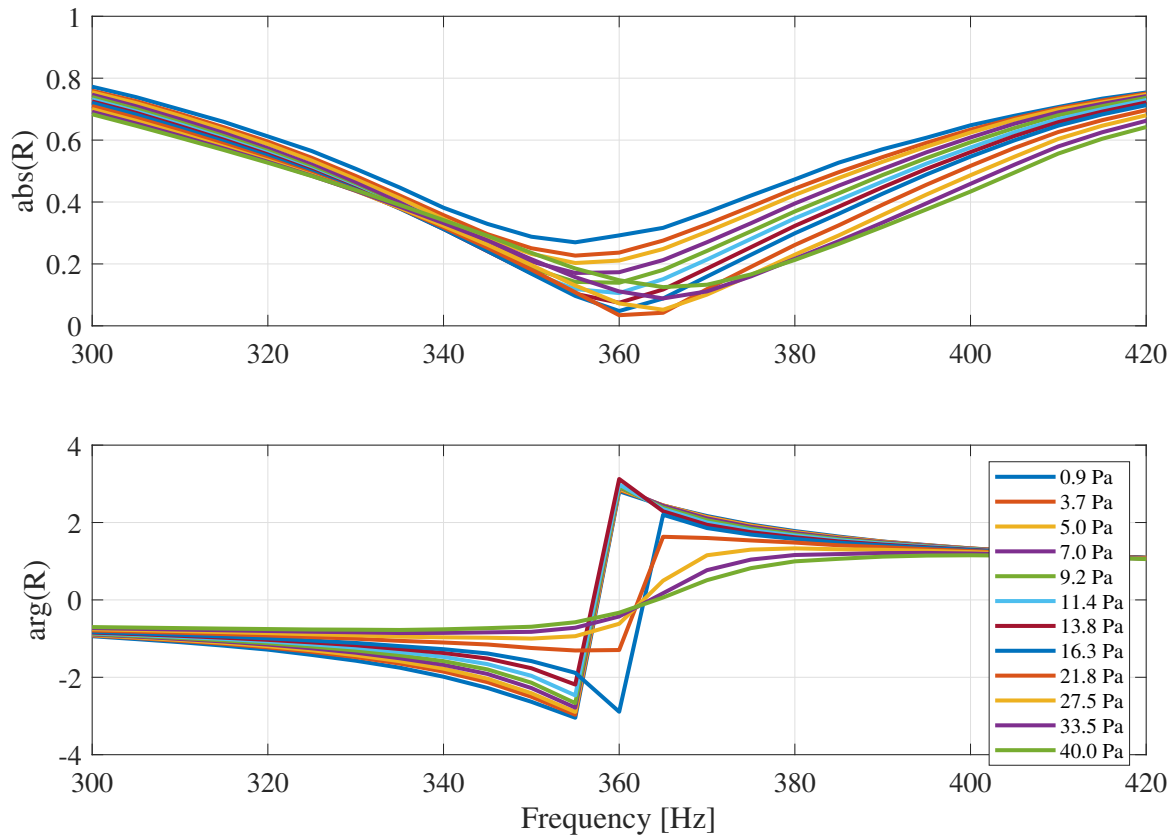


Figure B.2: Magnitude (top) and phase (bottom) of reflection coefficient for the P1 case with the cavity length of $L_c = 30 \text{ mm}$ and various excitation amplitudes obtained from direct measurement of acoustic pressure in the impedance tube.

C Re-calibration of the Coefficients of the Expression l_B

As mentioned in page 88, the coefficients of the expression l_B are re-calibrated using the experimental data. This section presents the experimental results that are used for re-calibration of the coefficients of the expression l_B , followed by describing the procedure to obtain the expression l_B for the triangular, square, and rectangular patterns separately.

Following data sets are the experimental results, which are obtained from direct measurement of acoustic pressure in the impedance tube, used for re-calibration of the coefficients of the expression l_B .

Similar to the procedure of re-calibrating of the coefficients of the expression l_{nl} , the data set used for regression is selected carefully so that the validation data set was excluded from the regression data set. These data sets are excluded to avoid validating the l_B expression with the underlying data set that the l_B is obtained from. Therefore, approximately 80% of the whole data set is used for regression and the remaining data points are used for validation.

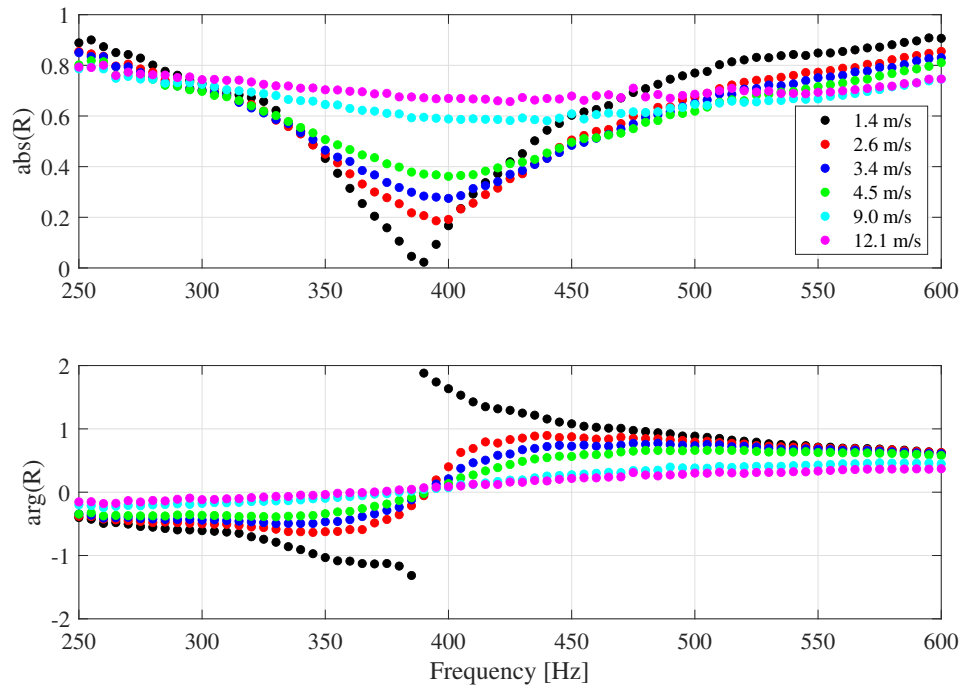


Figure C.1: Magnitude (top) and phase (bottom) of reflection coefficient for the P2 case with the cavity length of $L_c = 30 \text{ mm}$ obtained from direct measurement of acoustic pressure in the impedance tube.

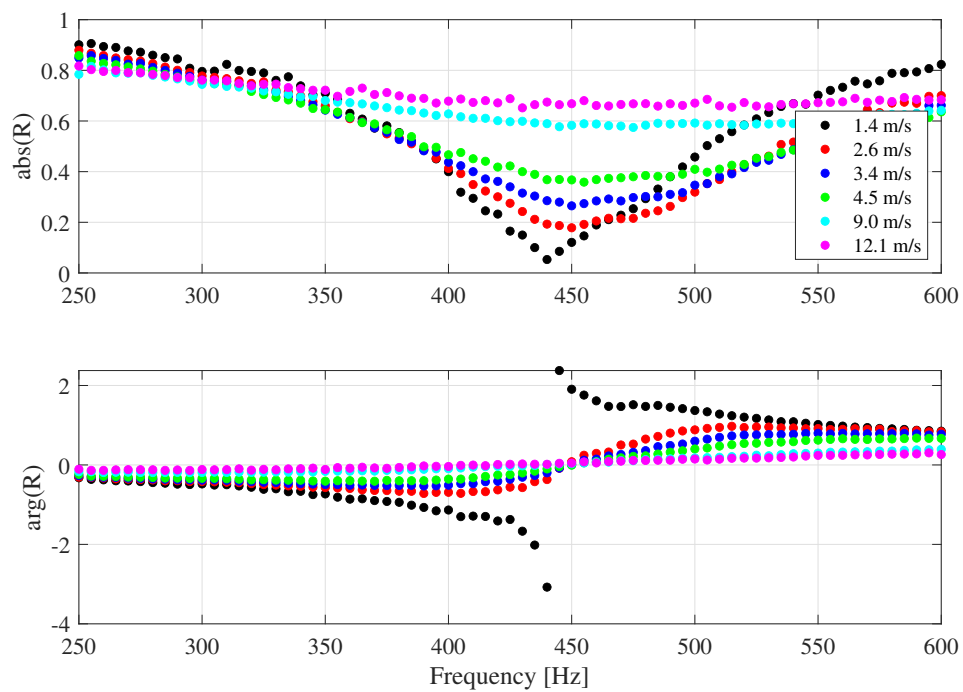


Figure C.2: Magnitude (top) and phase (bottom) of reflection coefficient for the P3 case with the cavity length of $L_c = 30 \text{ mm}$ obtained from direct measurement of acoustic pressure in the impedance tube.

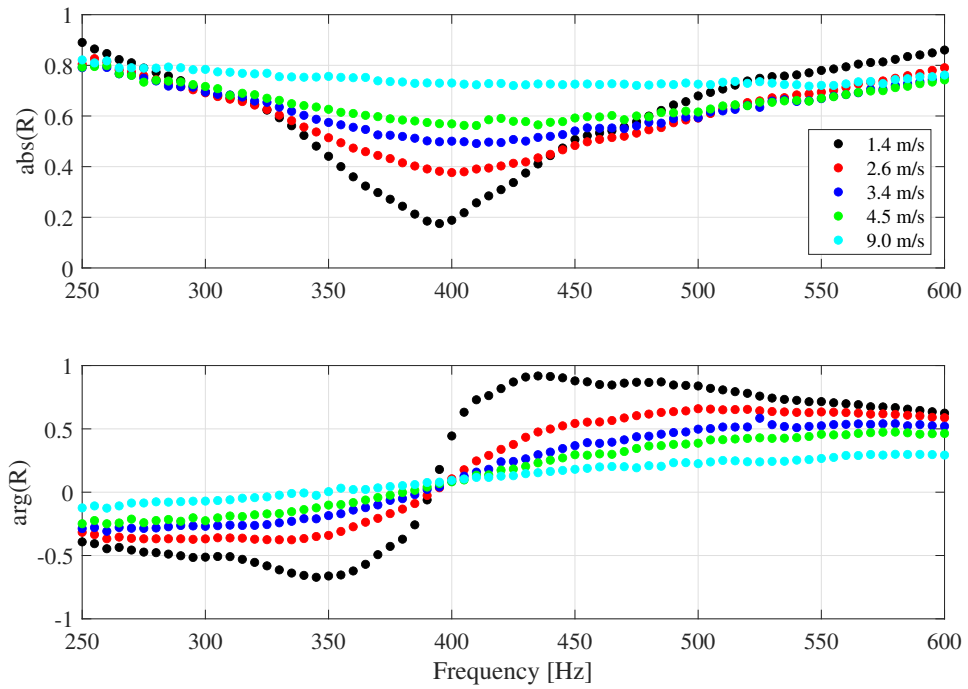


Figure C.3: Magnitude (top) and phase (bottom) of reflection coefficient for the S2 case with the cavity length of $L_c = 30 \text{ mm}$ obtained from direct measurement of acoustic pressure in the impedance tube.

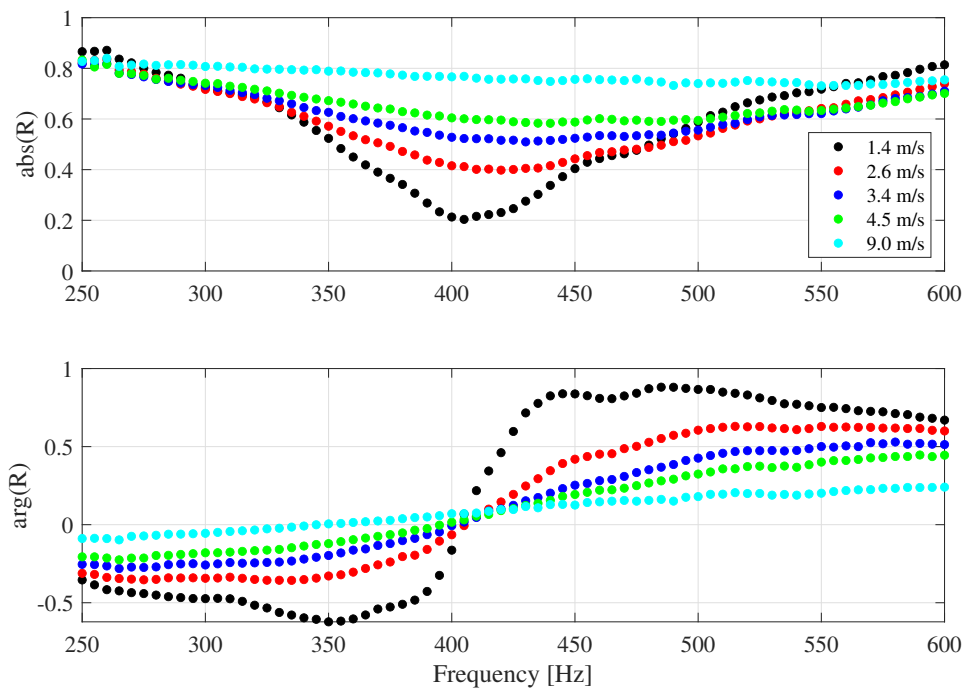


Figure C.4: Magnitude (top) and phase (bottom) of reflection coefficient for the S3 case with the cavity length of $L_c = 30 \text{ mm}$ obtained from direct measurement of acoustic pressure in the impedance tube.

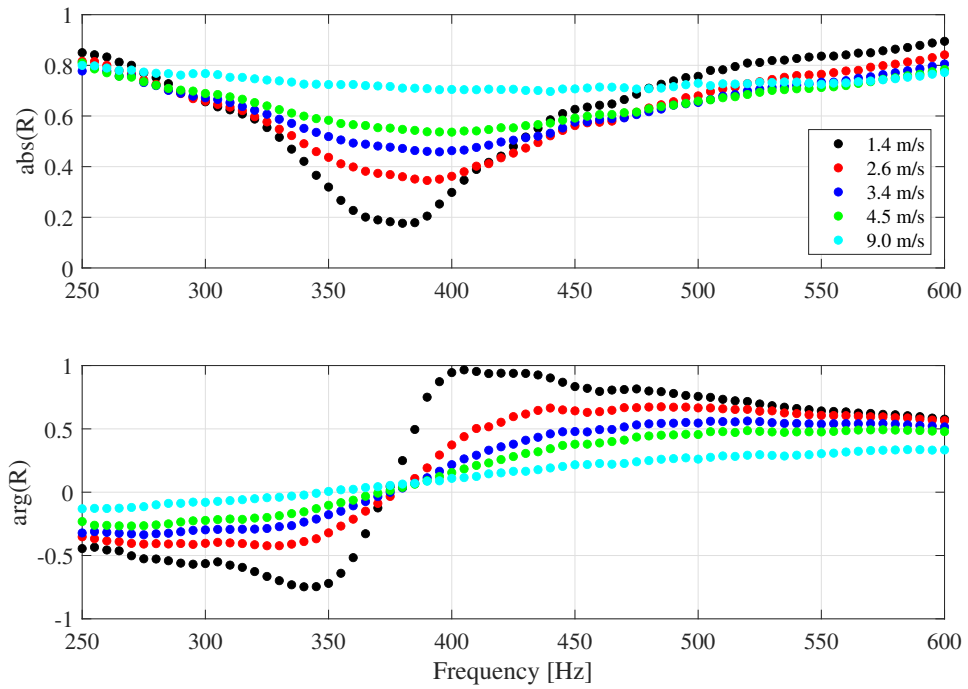


Figure C.5: Magnitude (top) and phase (bottom) of reflection coefficient for the S1a case with the cavity length of $L_c = 30 \text{ mm}$ obtained from direct measurement of acoustic pressure in the impedance tube.

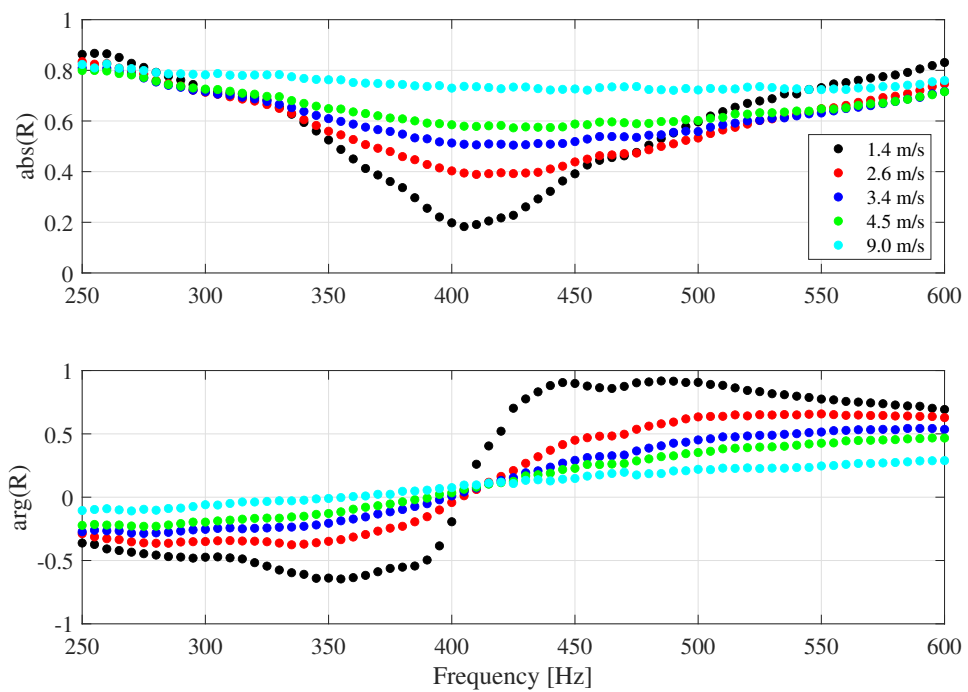


Figure C.6: Magnitude (top) and phase (bottom) of reflection coefficient for the S2a case with the cavity length of $L_c = 30\text{ mm}$ obtained from direct measurement of acoustic pressure in the impedance tube.

D Final Configuration of the Acoustic Impedance Model

As mentioned in page 79, in the current section, the final configuration of the modified Bellucci model, where the normalized end-correction is obtained from the mathematical correlations (δ_P and $\delta_{S,Sa}$), is presented. All equations presented in the current section are introduced throughout the current work. Thus, the equations in the current section are copied from the main text.

The modified Bellucci's model in the current study, is based on Bellucci's original model presented in Section 2.6. The resistance term of Bellucci et al. [8] yields

$$\theta_{Bellucci} = \frac{\varepsilon}{c\sigma} G\left(\frac{U_B}{|\hat{u}|}\right) |\hat{u}|, \quad (D.1)$$

where ε , which stands for pressure loss coefficient, is calculated as follows:

$$\varepsilon = \begin{cases} 1/C_d^2 & \text{if } U_B = 0, St_{ac} \leq (St_{ac})_{qs} \\ 0.6\left(\frac{3\pi}{4}\right)St_{ac}^{1/3} & \text{if } U_B = 0, St_{ac} > (St_{ac})_{qs} \\ \frac{\pi}{2} \frac{\delta St}{\gamma^2 + \delta^2} & \text{if } U_B \geq |\hat{u}| \\ \frac{\varepsilon_{nonlin}(1-G) + \varepsilon_{lin}(G - \frac{4}{3\pi})}{1 - \frac{4}{3\pi}} & \text{if } 0 < U_B < |\hat{u}| \end{cases}. \quad (D.2)$$

In Equation D.2, ε_{nonlin} in the forth expression corresponds to the first and second expressions in Equation D.2, depending on St_{ac} . In the forth expression of Equation D.2, ε_{lin} refers to the third expression with γ and δ , which are the real and imaginary parts of Howe's Rayleigh conductivity, respectively. The threshold of the quasi-steady assumption for the acoustic Strouhal number is defined by $(St_{ac})_{qs} = 0.61/C_d^6$.

In Equation D.1, $G(x)$ is proposed as:

$$G(x) = \begin{cases} \frac{2}{\pi} \left(x \cdot \arcsin(x) + \frac{\sqrt{1-x^2}}{3} (2+x^2) \right) & \text{if } |x| \leq 1 \\ |x| & \text{if } |x| > 1 \end{cases}. \quad (\text{D.3})$$

When $U_B > |\hat{u}|$, Equation D.1 reduces to the linear expression $\theta_{Bellucci} = \frac{\varepsilon}{c\sigma} U_B$. For large $|\hat{u}|$ and for $U_B < |\hat{u}|$, Equation D.1 predicts a nonlinear behavior of pressure losses [8, 17]. When bias flow is present, the resistance term in this model is based on Howe's Rayleigh conductivity model.

The impedance model of Bellucci et al. [8, 17] is based on Crandall's impedance model [22]. Additionally, different correction lengths are added to Crandall's impedance model, which yields

$$\chi_{modified\ Bellucci} = \frac{k}{\sigma} \left(l\Gamma + l_{eff} \right). \quad (\text{D.4})$$

In the current study, the original function Γ , introduced by Crandall [22] (presented in Equation 2.6), is used as

$$\Gamma(k_s r_0) = \left[1 - \frac{2J_1(k_s r_0)}{k_s r_0 J_0(k_s r_0)} \right]^{-1}. \quad (\text{D.5})$$

In Equation D.4, l_{eff} accounts for the end-correction length, including contributions from the radiation reactance and the hole-to-hole interaction effects (l_{h-h}), the bias flow (l_B), and nonlinear effects due to high amplitude excitation (l_{nl}). Considering the end-correction length for both sides of the orifice yields

$$l_{eff} = l_{h-h} \cdot l_{nl} \cdot l_B, \quad (\text{D.6})$$

where

$$l_{h-h} = 2 \cdot \frac{\delta (\pi \cdot r_0^2)^{1/2}}{\left[1 + \frac{(0.77kr_0)^2}{1+0.77kr_0}\right]}. \quad (D.7)$$

The normalized end-correction (δ) in Equation D.7 is obtained using the FEM results for triangular pattern (P) as

$$\delta_P = 0.48 \left(1 - 34 \frac{r_0}{R_c} + 26.56 \frac{r_0}{R_{eq}}\right), \quad (D.8)$$

and for square and rectangular patterns (S and Sa) as

$$\delta_{S,Sa} = 0.48 \left(1 - 50.41 \frac{r_0}{R_c} + 38.19 \frac{r_0}{R_{eq}}\right). \quad (D.9)$$

The expression l_{nl} for triangular pattern (P) is obtained as [2]

$$l_{nl}^P = 1 - \frac{0.15}{St_{ac}^{0.2}}, \quad (D.10)$$

and similarly, for the square and rectangular patterns (S and Sa) [2]

$$l_{nl}^{S,Sa} = 1 - \frac{0.09}{St_{ac}^{0.54}}. \quad (D.11)$$

The expression l_B for P pattern is obtained as

$$l_B^P = \frac{0.3(a_P/St^2) + 1}{a_P/St^2 + 1} \quad ; \quad a_P = 23 \left(\frac{R_{eq}}{R}\right)^3, \quad (D.12)$$

and for the square and rectangular patterns (S and Sa)

$$l_B^{S,Sa} = \frac{0.3(a_S/St^2) + 1}{a_S/St^2 + 1} \quad ; \quad a_S = 2.4 \left(\frac{R_{eq}}{R}\right)^2. \quad (D.13)$$

In the presence of a back cavity and considering the plane wave propagation into the back cavity, the final configuration of the modified Bellucci impedance model yields

$$\zeta_{modified\ Bellucci} = \frac{\varepsilon}{c\sigma} G\left(\frac{U_B}{|\hat{u}|}\right) |\hat{u}| + \frac{ik}{\sigma} (l\Gamma + l_{eff}) - i \cot(kL_c). \quad (\text{D.14})$$

Bibliography

- [1] Ingard, U., 1953. “On the Theory and Design of Acoustic Resonators”. *The Journal of the Acoustical Society of America*, **25**, p. 41.
- [2] Javareshkian, A., Dancelme, A., Chen, H., and Sattelmayer, T., 2021. “Influence of Hole-to-Hole Interaction on the Acoustic Behavior of Multi-Orifice Perforated Plates”. *Proceedings of ASME Turbo Expo 2021 - GT2021-58535*.
- [3] ACARE, 2011. Flightpath 2050 Europe’s Vision for Aviation. Tech. rep., Advisory Council for Aviation Research and Innovation in Europe.
- [4] Lefebvre, A. H. A. H., and Ballal, D. R., 2010. *Gas Turbine Combustion : Alternative Fuels and Emissions*. Taylor & Francis.
- [5] Rayleigh, J. W. S., 1878. “The Explanation of Certain Acoustical Phenomena”. *Nature*, **18**(455), pp. 319–321.
- [6] Rayleigh, J. W. S., 1945. *The Theory of Sound*, Vol. 2. Dover, New York.
- [7] Zhao, D., and Li, X., 2015. “A Review of Acoustic Dampers Applied to Combustion Chambers in Aerospace Industry”. *Progress in Aerospace Sciences*, **74**, pp. 114–130.
- [8] Bellucci, V., Flohr, P., and Paschereit, C. O., 2004. “Numerical and Experimental Study of Acoustic Damping Generated by Perforated Screens”. *AIAA Journal*, **42**(8), pp. 1543–1549.
- [9] Camporeale, S. M., Fortunato, B., and Mastrovito, M., 2008. “Prediction of Thermoacoustic Instability in Combustion Chamber Equipped With

- Passive Dampers”. *Proceedings of the ASME Turbo Expo 2008*, January, pp. 1087–1094.
- [10] Dupere, I. D. J., and Dowling, A. P., 2005. “The Use of Helmholtz Resonators in a Practical Combustor”. *Journal of Engineering for Gas Turbines and Power*, **127**(2), p. 268.
- [11] Gysling, D. L., Copeland, G. S., McCormick, D. C., and Proscia, W. M., 2000. “Combustion System Damping Augmentation With Helmholtz Resonators”. *Journal of Engineering for Gas Turbines and Power*, **122**(2), p. 269.
- [12] Richards, G. A., Straub, D. L., and Robey, E. H., 2003. “Passive Control of Combustion Dynamics in Stationary Gas Turbines”. *Journal of Propulsion and Power*, **19**(5), pp. 795–810.
- [13] Laudien, E., Pongratz, R., Pierro, R., and Preklik, D., 1995. “Fundamental Mechanisms of Combustion Instabilities: Experimental Procedures Aiding the Design of Acoustic Cavities”. In *Liquid Rocket Engine Combustion Instability*. American Institute of Aeronautics and Astronautics, Washington DC, January, ch. 14, pp. 377–399.
- [14] Dowling, A. P., and Stow, S. R., 2006. “Acoustic Analysis Of Gas-Turbine Combustors”. In *Combustion Instabilities In Gas Turbine Engines*. American Institute of Aeronautics and Astronautics (AIAA), Reston, VA, ch. 13, pp. 369–414.
- [15] Bechert, D. W., 1980. “Sound Absorption Caused by Vorticity Shedding, Demonstrated with a Jet Flow”. *Journal of Sound and Vibration*, **70**(3), June, pp. 389–405.
- [16] Jing, X., and Sun, X., 1999. “Experimental Investigations of Perforated Liners with Bias Flow”. *The Journal of the Acoustical Society of America*, **106**(5), October, p. 2436.
- [17] Bellucci, V., Paschereit, C. O., and Flohr, P., 2002. “Impedance of Perforated Screens with Bias Flow”. *8th AIAA/CEAS Aeroacoustics Conference, 17-19 June 2002, Breckenridge, Colorado*.

BIBLIOGRAPHY

- [18] Heaviside, O., 2012. “Electromagnetic Induction and its Propagation (Second half)”. In *Electrical Papers*. Cambridge University Press, March, pp. 39–155.
- [19] Webster, A. G., 1919. “Acoustical Impedance and the Theory of Horns and of the Phonograph”. *Proceedings of the National Academy of Sciences*, **5**(7), July, pp. 275–282.
- [20] Pierce, A. D., and Beyer, R. T., 1990. “Acoustics: An Introduction to its Physical Principles and Applications.”. *The Journal of the Acoustical Society of America*, **87**(4), April, pp. 1826–1827.
- [21] Morfey, C. L., 2001. *Dictionary of Acoustics*. Academic Press.
- [22] Crandall, I., 1926. *Theory of Vibrating Systems and Sound*. D. Van Nostrand Co., New York.
- [23] Melling, T. H., 1973. “The Acoustic Impedance of Perforates at Medium and High Sound Pressure Levels”. *Journal of Sound and Vibration*, **29**(1), pp. 1–65.
- [24] Rayleigh, J. W. S., 1871. “On the Theory of Resonance”. *Philosophical Transactions of the Royal Society of London*, **161**, January, pp. 77–118.
- [25] Lieuwen, T., 2012. *Unsteady Combustor Physics*. Cambridge University Press.
- [26] Helmholtz, H., 1860. “Theorie der Luftschwingungen in Röhren mit offenen Enden”. *Journal für die Reine und Angewandte Mathematik*, **1860**(57), January, pp. 1–72.
- [27] Norris, A. N., and Sheng, I. C., 1989. “Acoustic Radiation from a Circular Pipe with an Infinite Flange”. *Journal of Sound and Vibration*, **135**(1), November, pp. 85–93.
- [28] Levine, H., and Schwinger, J., 1948. “On the Radiation of Sound from an Unflanged Circular Pipe”. *Physical Review*, **73**(4), February, pp. 383–406.

- [29] Nomura, Y., Yamamura, I., and Inawashiro, S., 1960. “On the Acoustic Radiation from a Flanged Circular Pipe”. *Journal of the Physical Society of Japan*, **15**(3), December, pp. 510–517.
- [30] Causse, R., Kergomard, J., and Lurton, X., 1984. “Input Impedance of Brass Musical Instruments Comparison between Experiment and Numerical Models”. *Journal of the Acoustical Society of America*, **75**(1), January, pp. 241–254.
- [31] Dalmont, J. P., Nederveen, C. J., and Joly, N., 2001. “Radiation Impedance of Tubes with Different Flanges: Numerical and Experimental Investigations”. *Journal of Sound and Vibration*, **244**(3), July, pp. 505–534.
- [32] Allard, J. F., 1993. *Propagation of Sound in Porous Media*. Elsevier applied sciences.
- [33] Maa, D.-Y., and Liu, K., 2000. “Sound Absorption Characteristics of Microperforated Absorbers for Random Incidence”. *Chinese Journal of Acoustics*, **19**, pp. 289–298.
- [34] Liu, K., Nocke, C., and Maa, D.-Y., 2000. “Experimental Investigation on Sound Absorption Characteristics of Microperforated Panel in Diffuse Field”. *Acta Acustica (in Chinese)*, **25**, pp. 211–218.
- [35] Jaouen, L., and Chevillotte, F., 2018. “Length Correction of 2D Discontinuities or Perforations at Large Wavelengths and for Linear Acoustics”. *Acta Acustica united with Acustica*, **102**(2), April, pp. 243–250.
- [36] Wertheim, G., 1851. “Mémoire sur les vibrations sonores de l’air”. *Annales de Chimie et de Physique*, **31**, pp. 385–432.
- [37] Kergomard, J., Garcia, A., Tagui, G., and Dalmont, J. P., 1989. “Analysis of Higher Order Mode Effects in an Expansion Chamber Using Modal Theory and Equivalent Electrical Circuits”. *Journal of Sound and Vibration*, **129**(3), pp. 457–475.
- [38] Kinsler, L., Frey, A., Coppens, A., and Sanders, J., 2000. *Fundamentals of acoustics*, 4th ed. John Wiley and Sons, New York.

- [39] Bolt, R. H., Labate, S., and Ingard, U., 1949. “The Acoustic Reactance of Small Circular Orifices”. *Journal of the Acoustical Society of America*, **21**(2), pp. 94–97.
- [40] Morse, P., 1948. *Vibration and Sound*, 2nd ed. McGraw-Hill, New York.
- [41] Fok, V. A., 1941. “Theoretical Study of the Conductance of a Circular Hole, in a Partition Across a Tube”. *Proceedings of the USSR Academy of Sciences*, **31**, pp. 875–878.
- [42] Rschevkin, S. N., 1963. *A Course of Lectures on the Theory of Sound*. Macmillan & Co.Ltd. (New York), Pergamon Press (London).
- [43] Nesterov, V. S., 1941. “Experimental Study of the Conductance of a Circular Hole, in a Partition Across a Tube”. *Proceedings of the USSR Academy of Sciences*, **31**, pp. 879–882.
- [44] Ingard, U., 1948. “On the Radiation of Sound into a Circular Tube, with an Application to Resonators”. *Citation: The Journal of the Acoustical Society of America*, **20**, p. 2360.
- [45] Karal, F. C., 1953. “The Analogous Acoustical Impedance for Discontinuities and Constrictions of Circular Cross Section”. *The Journal of the Acoustical Society of America*, **25**, pp. 327–334.
- [46] Acoustical Porous Material Recipes: <https://apmr.matelys.com/BasicsAcoustics/LengthCorrections/>.
- [47] Jaouen, L., and Bécot, F.-X., 2011. “Acoustical Characterization of Perforated Facings Dynamic Tortuosity and Bulk Modulus in Air-saturated Porous Media”. *The Journal of the Acoustical Society of America*, **129**, p. 1975.
- [48] Ih, J.-G., 1993. “On the Inertial End Correction of Resonators”. *Acta Acustica united with Acustica*, **78**, pp. 1–15.
- [49] Tayong, R., 2013. “On the Holes Interaction and Heterogeneity Distribution Effects on the Acoustic Properties of Air-cavity Backed Perforated Plates”. *Applied Acoustics*, **74**(12), December, pp. 1492–1498.

- [50] Tayong, R., Dupont, T., and Leclaire, P., 2011. “Experimental Investigation of Holes Interaction Effect on the Sound Absorption Coefficient of Micro-perforated Panels under High and Medium Sound Levels”. *Applied Acoustics*, **72**(10), October, pp. 777–784.
- [51] Wang, J., Rubini, P., Qin, Q., and Houston, B., 2019. “A Model to Predict Acoustic Resonant Frequencies of Distributed Helmholtz Resonators on Gas Turbine Engines”. *Applied Sciences*, **9**(7), April, p. 1419.
- [52] Kergomard, J., and Garcia, A., 1987. “Simple Discontinuities in Acoustic Waveguides at Low Frequencies: critical analysis and formulae”. *Journal of Sound and Vibration*, **114**(3), pp. 465–479.
- [53] Howe, M. S., 1979. “On the Theory of Unsteady High Reynolds Number Flow Through a Circular Aperture”. *Proceedings of the Royal Society of London.*, **366**, pp. 205–223.
- [54] Howe, M. S., 1998. *Acoustics of Fluid Structure Interactions*. Cambridge University Press, Cambridge.
- [55] Ahuja, K. K., and Gaeta, R. J., 2000. Active Control of Liner Impedance by Varying Perforate Orifice Geometry. Tech. rep., Contractor Report NASA-CR-2000-210633, NASA.
- [56] Atalla, N., and Sgard, F., 2007. “Modeling of Perforated Plates and Screens Using Rigid Frame Porous Models”. *Journal of Sound and Vibration*, **303**(1-2), June, pp. 195–208.
- [57] Euler, L., 1757. “General Principles of the Motion of Fluids”. *Mémoires de l’académie des sciences de Berlin*, **11**, pp. 274–315.
- [58] Batchelor, G., 2000. *An Introduction to Fluid Dynamics*. Cambridge University Press, Cambridge, UK.
- [59] Stokes, G., 1845. “On the Theories of the Internal Friction of Fluids in Motion, and of the Equilibrium and Motion of Elastic Solids”. *Transactions of the Cambridge Philosophical Society*, **8**, pp. 287–319.
- [60] Bird, R., Stewart, W., and Lightfoot, E., 2002. *Transport Phenomena*, 2nd ed. John Wiley and Sons, New York.

BIBLIOGRAPHY

- [61] Clapeyron, B., 1837. “Memoir on the Motive Power of Heat”. *Scientific Memoirs, Selected From the Transactions of Foreign Academies of Science and Learned Societies and From Foreign Journals*, **1**, pp. 347–376.
- [62] Goldstein, M., 1976. *Aeroacoustics*. McGraw-Hill, New York.
- [63] D’Alembert, 1747. “Investigation of the Curve Formed by a Vibrating String”. *Histoire de l’Académie des sciences et belles-lettres*, **3**, pp. 214–219.
- [64] Euler, L., 1766. “On the Propagation of Sound”. *Mémoires de l’académie des sciences de Berlin*, **15**, pp. 185–209.
- [65] Campos, L., 2007. “On 36 Forms of the Acoustic Wave Equation in Potential Flows and Inhomogeneous Media”. *Applied Mechanics Review*, **60**, pp. 149–171.
- [66] Mason, V., 1969. “Some Experiments on the Propagation of Sound along a Cylindrical Duct Containing Flowing Air”. *Journal of Sound and Vibration*, **10**(2), pp. 208–226.
- [67] Michalke, A., 1989. “On the Propagation of Sound Generated in a Pipe of Circular Cross-section with Uniform Mean Flow”. *Journal of Sound and Vibration*, **134**(2), pp. 203–234.
- [68] Morfey, C., 1971. “Sound Transmission and Generation in Ducts with Flow”. *Journal of Sound and Vibration*, **14**(1), pp. 37–55.
- [69] Munjal, M., 1987. *Acoustics of Ducts and Mufflers*. John Wiley and Sons, New York.
- [70] Morse, P., and Ingard, K., 1968. *Theoretical Acoustics*. McGraw-Hill, New York.
- [71] Selamet, A., and Ji, Z. L., 2000. “Circular Asymmetric Helmholtz Resonators”. *The Journal of the Acoustical Society of America*, **107**, pp. 2360–2369.
- [72] Horner, J., and Hu, Y., 2013. “Investigation into Higher-order Mode Propagation Through Orifice Plates in Circular Ducts”. *Applied Acoustics*, **74**(5), May, pp. 728–739.

- [73] Abom, M., 1992. “A Note on the Experimental Determination of Acoustical Two-port Matrices”. *Journal of Sound and Vibration*, **155**(1), pp. 185–188.
- [74] Kuttruff, H., 2006. *Acoustics: An Introduction*. Taylor & Francis Group, London and New York.
- [75] Rasmussen, C. E., Williams, C. K. I., and Bach, F., 2006. *Gaussian Processes for Machine Learning*. The MIT Press, Cambridge, Massachusetts.
- [76] Vapnik, V. N., 1995. *The Nature of Statistical Learning Theory*. Springer Verlag, New York.
- [77] McCartney, M., Haeringer, M., and Polifke, W., 2020. “Comparison of Machine Learning Algorithms in the Interpolation and Extrapolation of Flame Describing Functions”. *Journal of Engineering for Gas Turbines and Power*, **142**(6).
- [78] Salomon, D., 2006. *Spline Interpolation*. Springer New York, New York, NY, pp. 141–173.
- [79] Hall, C. A., and Meyer, W., 1976. “Optimal Error Bounds for Cubic Spline Interpolation”. *Journal of Approximation Theory*, **16**(2), pp. 105–122.
- [80] Dahlquist, G., and Bjorck, A., 2003. *Numerical Methods*. Dover, New York.
- [81] Lahiri, C., 2014. “Acoustic Performance of Bias Flow Liners in Gas Turbine Combustors”. Doctoral thesis, Technical University Berlin.
- [82] Eldredge, J. D., and Dowling, A. P., 2003. “The Absorption of Axial Acoustic Waves by a Perforated Liner with Bias Flow”. *Journal of Fluid Mechanics*, **485**, May, pp. 307–335.
- [83] Follet, J., Betts, J., and Kelly, J., 2001. “Improvements to Acoustic Liner Broadband Absorption Using Bias Flow”. In 39th Aerospace Sciences Meeting and Exhibit, American Institute of Aeronautics and Astronautics.
- [84] Heuwinkel, C., Enghardt, L., and Rohle, I., 2007. “Experimental Investigation of the Acoustic Damping of Perforated Liners with Bias Flow”. In 13th

BIBLIOGRAPHY

AIAA/CEAS Aeroacoustics Conference (28th AIAA Aeroacoustics Conference), American Institute of Aeronautics and Astronautics.

- [85] Hughes, I. J., and Dowling, A. P., 1990. “The Absorption of Sound by Perforated Linings”. *Journal of Fluid Mechanics*, **218**, September, pp. 299–335.
- [86] Kang, Z., and Ji, Z., 2008. “Acoustic Length Correction of Duct Extension into a Cylindrical Chamber”. *Journal of Sound and Vibration*, **310**(4-5), March, pp. 782–791.